UNITED NATIONS
UNIVERSITY

UNU-GTP
Geothermal Training Programme

ORKUSTOFNUN

Blési hot spring at Geysir geothermal field

Vincent Kipkirui Koech

NUMERICAL GEOTHERMAL RESERVOIR MODELLING AND INFIELD REINJECTION DESIGN, CONSTRAINED BY TRACER TEST DATA: CASE STUDY FOR THE OLKARIA GEOTHERMAL FIELD IN KENYA

Report 5
December 2014

NUMERICAL GEOTHERMAL RESERVOIR MODELLING AND INFIELD REINJECTION DESIGN, CONSTRAINED BY TRACER TEST DATA: CASE STUDY FOR THE OLKARIA GEOTHERMAL FIELD IN KENYA

MSc thesis
School of Engineering and Natural Sciences
Faculty of Industrial Engineering, Mechanical Engineering and Computer Science
University of Iceland

by

Vincent Kipkirui Koech
Kenya Electricity Generating Company Ltd. - KenGen
P.O. Box 785, Naivasha
KENYA
vkoech@kengen.co.ke

INTRODUCTION

The Geothermal Training Programme of the United Nations University (UNU) has operated in Iceland since 1979 with six month annual courses for professionals from developing countries. The aim is to assist developing countries with significant geothermal potential to build up groups of specialists that cover most aspects of geothermal exploration and development. During 1979-2014, 583 scientists and engineers from 58 developing countries have completed the six month courses, or similar. They have come from Asia (37%), Africa (36%), Central America (15%), Europe (11%), and Oceania (1%) There is a steady flow of requests from all over the world for the six-month training and we can only meet a portion of the requests. Most of the trainees are awarded UNU Fellowships financed by the Government of Iceland.

Candidates for the six-month specialized training must have at least a BSc degree and a minimum of one year practical experience in geothermal work in their home countries prior to the training. Many of our trainees have already completed their MSc or PhD degrees when they come to Iceland, but several excellent students who have only BSc degrees have made requests to come again to Iceland for a higher academic degree. From 1999 UNU Fellows have also been given the chance to continue their studies and study for MSc degrees in geothermal science or engineering in co-operation with the University of Iceland. An agreement to this effect was signed with the University of Iceland. The six-month studies at the UNU Geothermal Training Programme form a part of the graduate programme.

It is a pleasure to introduce the 39th UNU Fellow to complete the MSc studies at the University of Iceland under the co-operation agreement. Vincent Kipkirui Koech, BSc in Mechanical Engineering, from Kenya Electricity Generating Company Ltd., - KenGen, completed the six-month specialized training in Reservoir Engineering at the UNU Geothermal Training Programme in October 2011. His research report was entitled: *Initial conditions of wells OW 905A, OW 907A, OW 913A and OW 916A, and a simple natural state model of Olkaria Domes geothermal field, Kenya.* After two years of geothermal research work in Kenya, he came back to Iceland for MSc studies at Faculty of Industrial Engineering, Mechanical Engineering and Computer Science in February 2013. In September 2014, he defended his MSc thesis presented here, entitled *Numerical geothermal reservoir modelling and infield reinjection design, constrained by tracer test data: Case study for the Olkaria power plant.* His studies in Iceland were financed by the Government of Iceland through a UNU-GTP Fellowship from the UNU Geothermal Training Programme. We congratulate him on his achievements and wish him all the best for the future. We thank the Faculty of Industrial Engineering, Mechanical Engineering and Computer Science at the School of Engineering and Natural Sciences of the University of Iceland for the co-operation, and his supervisors for the dedication.

Finally, I would like to mention that Vincent´s MSc thesis with the figures in colour is available for downloading on our website *www.unugtp.is*, under publications.

<div style="margin-left:4em;">

With warmest greetings from Iceland,

Ludvik S. Georgsson, director
United Nations University
Geothermal Training Programme

</div>

ACKNOWLEDGEMENTS

DEDICATION

To my beloved wife, Lynnet, for her remarkable patience and unwavering love and support over the course of the study, and my sweet daughter Skylar

ABSTRACT

Numerical simulation of geothermal reservoirs is a very useful instrument for developing strategies of field exploitation, production well location and reinjection scheme design. Reinjection of spent geothermal fluids serves to maintain reservoir pressure and enhance energy extraction efficiency over the life of the resource. Tracer testing is used as tool for tracing flow within a geothermal system for the purpose of characterizing the system and to gain good understanding on inherent heterogeneity. Tracer transport is orders of magnitude faster than cold-front advancement around reinjection boreholes and can be used as a cooling prediction tool.

This study involved interpretation of tracer test data collected during cold injection into well OW-12 in the Olkaria geothermal field in Kenya. A single fracture model showed well OW-15 to be the most affected by the cold reinjection and OW-19 to be the least affected. A pessimistic version of the model predicts well OW-15 to cool by more than 20°C and wells OW-18 and OW-19 to cool by about 6°C for a forecast period of 15 years. An optimistic model version predicts well OW-15 to cool by 16°C, OW-18 to cool by 2°C and OW-19 to cool by 4°C for the same period. A numerical reservoir model was developed for the Olkaria East and Southeast fields, covering an area of 27 km2. The natural state model matched well available temperature and pressure data as well as being validated by production history data. Thermal front advance compares well for both models, it takes about a year to be felt in production well. Onset of cooling is immediate for single fracture model but in numerical model there is temperature rise followed by decline. This temperature increase before decline in the complex model is attributed to steam cap collapse.

Well OW-12 in Olkaria can be used as a cold reinjection well, but it has to be used intermittently according to the results of the study, injection for one year followed by a period of recovery. The current injection depth in well OW-12 is shallow, but model calculations show that if reinjection depth is considerably greater (-2600 m a.s.l.), longer injection periods are possible without collapse of the steam cap involved.

TABLE OF CONTENTS

LIST OF FIGURES

LIST OF TABLES

EXPLANATION OF SYMBOLS

A Area [m^2]
D Distance [m]
D_{ij} Dispersion tensor [m^2/s]
D_m Molecular diffusion [m^2/s]
C   Tracer concentration [kg/m^3]
c Heat capacity [J/kg]
E Thermal energy [J]
Ea Energy of activation (J/mol);
F Mass or heat flux [kg/s.m^2] or [J/m^2 s]
f Fickian diffusive mass flux [kg/s.m^2]
g Acceleration due to gravity [m/s^2]
h Reservoir thickness [m] or enthalpy [J/kg]
k Absolute permeability [m^2] or decay parameter [s^{-1}].
$k_{r\beta}$ Relative permeability [-]
M Mass per volume [kg/m^3]
M_R Ratio of tracer recovered
n Normal vector
P Pressure [Pa]
Q,q Mass flow rate [kg/s]
R Residual or universal gas constant [J/mol K]
R_g Recovery factor
S Saturation [m^3/m^3]
T Temperature [°C] or absolute temperature [K]
t Time [s]
$\bar{t}$ Mean transit time [s]
u Specific internal energy [J/kg]
U Darcy velocity [m/s]
v velocity [m/s]
V Volume [m^3]
X Mass fraction

Greek letters

$\alpha_{L,T}$ Dispersivity [m]
η Conversion efficiency
ρ Density [kg/m^3]
μ Dynamic viscosity [kg/m s]
ϕ Rock porosity
β Specific heat capacity [kJ/kgK]
Γ Surface area [m^2]
τ Turtuosity
λ Thermal conductivity [W/m°C]

x

1. INTRODUCTION

The Greater Olkaria geothermal field is in the southern part of the Kenyan rift. It is located south of Lake Naivasha, approximately 120 km northwest of Nairobi city. Exploration for geothermal resources in Kenya started in 1950's with mainly geological investigations in the region between Olkaria and Lake Bogoria in the north rift. In 1970s exploration was carried out in Olkaria and by 1976, six deep wells had been drilled. After evaluation of these initial wells, development was found to be feasible. By 1981 the first 15 MWe generating unit located in Olkaria East was commissioned. More wells were drilled and connected to the steam gathering system. Unit 2 and Unit 3, each 15 MWe, were commissioned in 1982 and 1985, respectively. Olkaria II located in Olkaria Northeast, was commissioned in 2003. The plant has been producing 70 MWe since and an additional 35 MWe turbine was later commissioned in May 2010, increasing the generation capacity to 105 MWe. Olkaria West hosts Olkaria III Independent Power Producer (IPP) power plant generating 48 MWe; the first 12 MWe unit was commissioned in 2000 and the second 36 MWe was commissioned in 2009. Olkaria III currently generates 102 MWe and is owned and operated by an Independent Power Producer, OrPower4 Inc. After latest commissioning the total power generated by KenGen in this geothermal field is over 500 MWe. In addition, several wellhead power plants are being put up to allow early generation as the company sources for more funds to construct a big power plant.

The principal methods and main steps of geothermal resource assessment can be classified depending on the phase of resource development. During exploration and the initial stages of exploitation the main focus is on geological studies, geophysical exploration, geochemical studies and reservoir engineering well studies once some wells have been drilled. The main quantitative resource assessment method used during the early exploration stages is the volumetric assessment method, the method involves estimating the energy content within the system volume and how much of that can be extracted within a given time-period and ultimately used to generate electricity. Once exploitation from a geothermal resource starts the emphasis shifts to resource assessment by *dynamic modelling*, i.e. modelling aimed at stimulating physical conditions in a geothermal system and its response to utilization (e.g. pressure decline, enthalpy changes), which chiefly controls the production capacity of a given resource. This is done through a variety of modelling methods and by utilizing assorted software packages. The most commonly used methods are (i) lumped parameter modelling of the mass-balance and pressure-response in geothermal systems and (ii) detailed numerical reservoir modelling (Axelsson, 2008a). Numerical modelling is the main assessment method applied in this study.

Numerical simulation of geothermal reservoirs is a very useful instrument for making decisions about the strategies of field exploitation, production well location and design, and reinjection schemes. Numerical model construction must be supported by a detailed knowledge of the spatial distribution of the properties of the reservoir in the form of a conceptual model. The accuracy in the collection of the data is fundamental for the construction of an efficient conceptual and numerical model.

Reinjection of spent geothermal fluids has become a major reservoir management strategy. It not only serves to maintain reservoir pressure, but also to increases energy extraction efficiency over the life of the resource. Tracer testing is used as tool for tracing flow within a geothermal reservoir for the purpose of characterizing the geothermal system and to gain good understanding on the heterogeneity of a geothermal system. This is done to determine well connectivity and mitigate against thermal break through during reinjection.

Numerical modelling has been applied in Olkaria geothermal resource development. The latest revision of the conceptual and numerical models was performed in 2012 when Mannvit/ISOR/Vatnaskil/Verkis consortium (Axelsson et al., 2013a and 2013b) undertook a comprehensive study of the field. In this study a smaller model covering Olkaria East and Southeast is developed. The model is mainly used in for a tracer and infield reinjection study.

The study involved interpretation of data from a tracer test done from July 1996 to September 1997, during cold injection in OW-12. In the first case a single fracture model is used to estimate parameters for flow channels connecting wells OW-15, OW-18 and OW-19 to the injection well OW-12. Parameters

from the single fracture model are used to predict cooling for two scenarios. In the second case an attempt is made to calibrate the numerical model developed in the study with the tracer test data. The current conceptual reservoir model, which has been developed over the last three decades, provides the basis for development of the numerical model. The model is then calibrated on well test temperature logs. The results of this are represented in the form of natural state model of the pre-exploitation state (1981). A production model is then validated on basis of thermodynamic properties of the discharged fluids. An attempt is then made to further calibrate it on chemical tracer test data.

The objectives of the study are the following:

- To interpret the tracer test data and apply it to predict cooling using single fracture one-dimensional model and a complex three-dimensional numerical reservoir model, covering Olkaria East and Southeast

- Develop and calibrate a natural state model of Olkaria East and Southeast parts of the field from the current conceptual model and thermophysical properties of the reservoir measured in the natural state.

- Validate the numerical reservoir model with production history matching. Production well mass flows and enthalpies, reinjection well mass injected and enthalpy, and the monitoring well pressure time series are used to calibrate the model.

- Use the numerical model to forecast field response to long term reinjection. Different mass flows, fluid temperature and injection depths scenarios are tested.

- Comparison of the prediction performed with the single fracture model and complex three-dimensional numerical reservoir model.

2. OLKARIA GEOTHERMAL FIELD

The Greater Olkaria geothermal field is in the southern part of the Kenyan rift. It is located south of Lake Naivasha, approximately 120 km northwest of Nairobi city. Olkaria geothermal area has been divided into seven development sectors. These are Olkaria East, Olkaria Northeast, Olkaria South West, Olkaria Central, Olkaria North West, Olkaria South East, and Olkaria Domes. These fields are named with respect to Olkaria Hill (Figure 1).
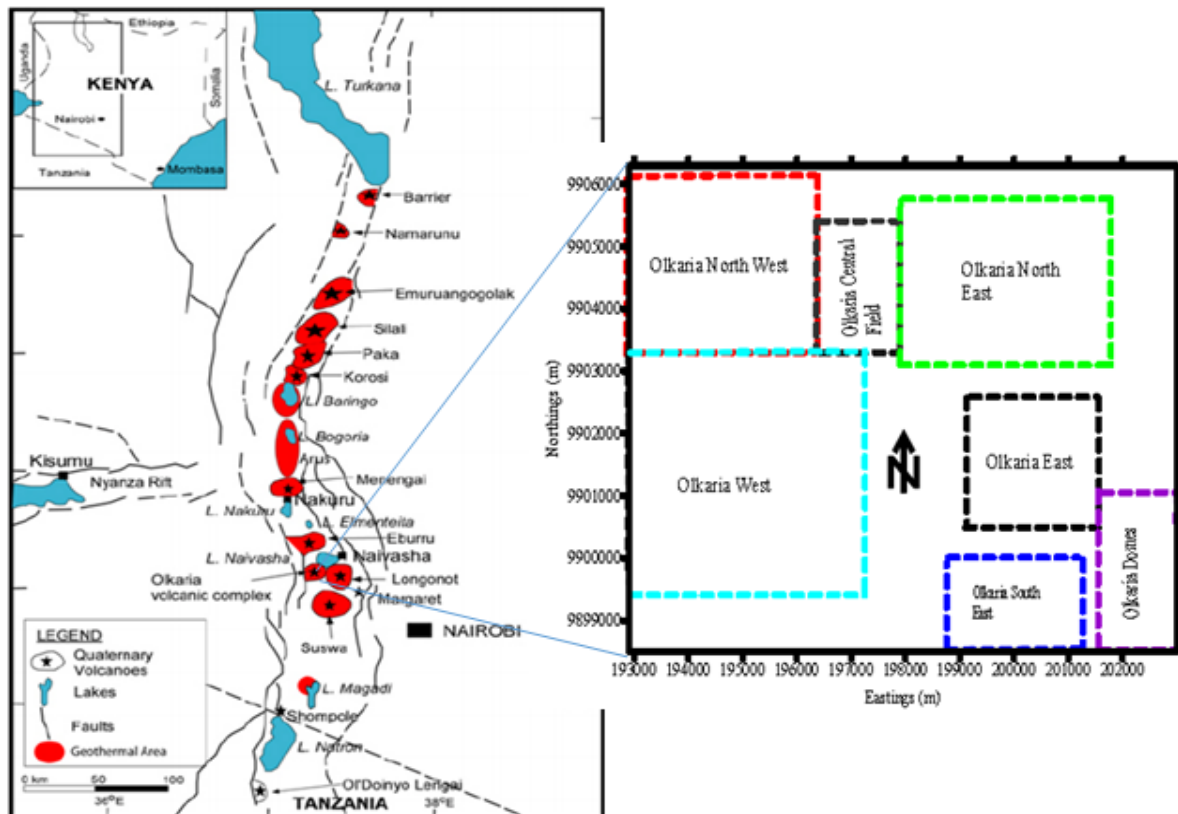
FIGURE 1: Location map of geothermal prospects in the Kenyan Rift valley and geothermal fields in the Greater Olkaria geothermal area

Exploration for geothermal resources in Kenya started in 1950's with mainly geological investigations in the region between Olkaria and Lake Bogoria in the north rift. The exploration resulted in the drilling of two wells X-1 and X-2 in Olkaria which encountered high temperatures at depth but failed to produce steam. In 1970s exploration was carried out with the support of the United Nations Development Program (UNDP) and by 1976, six deep wells had been drilled. After evaluation of these initial wells, development was found to be feasible. By 1981 the first 15 MWe generating unit was commissioned. The first power plant that was commissioned is located in Olkaria East. More wells were drilled and connected to the steam gathering system. Unit 2 and Unit 3, each 15 MWe, were commissioned in 1982 and 1985, respectively. Olkaria II located in Olkaria Northeast, was commissioned in 2003. The plant has been producing 70 MWe since and an additional 35 MWe turbine was later commissioned in May 2010, increasing the generation capacity to 105 MWe. Olkaria West hosts Olkaria III Independent Power Producer (IPP) power plant generating 48 MWe; the first 12 MWe unit was commissioned in 2000 and the second 36 MWe was commissioned in 2009.

The Greater Olkaria geothermal field currently hosts four power plants and five wellhead units. Olkaria I, II, III and IV located in East, North East, West and Domes Respectively (Figure 1). After latest commissioning of 140 MWe in Olkaria Domes and 140 MWe expansion in Olkaria I, the total power generation capacity of KenGen in this geothermal field is over 500 MWe. In addition, several wellhead power plants are being put up to allow early generation.

TABLE 1: Greater Olkaria geothermal field development over the years

Year	Activity
1950s	Scientific investigations in Olkaria, Eburru and Lake Bogoria all within Great Rift Valley (Noble and Ojiambo, 1975)
1958	Two exploration wells X-1 and X-2 drilled in Olkaria. Encountered high temperature but unproductive (Noble and Ojiambo, 1975)
1970s	Extensive exploration project carried out with financial support of UNDP (Noble and Ojiambo, 1975)
1976	6 additional wells drilled and feasibility of field development confirmed
1981, 1982 and 1985	1st, 2nd and 3rd 15 MWe generating units commissioned in Olkaria East (Olkaria I). A plant with total 45 MWe capacity operated by KenGen (Bodvarsson et al., 1987)
1990s	Detailed Exploration and Later drilling of 3 exploration wells in Olkaria Domes (located in the southeast part of the Olkaria field)
2000	12 MWe unit commissioned in Olkaria west part of the field (Olkaria III) operated by Independent Power Producer (IPP) OrPower4 Inc.
2003, 2010	Olkaria II plant, located in Olkaria Northeast field, was commissioned with 2 units each 35 MWe, and later 3rd unit with 35 MWe, making a total of 105 MWe operated by KenGen
2009, 2011	Olkaria III production was increased first by 36 MWe and later by 62 MWe making the current total by OrPower4 Inc. to be about 110 MWe
2011-2014	- Well heads units introduced; 3 units with a combined capacity of more than 40 MWe (operated by KenGen) - Beginning of production in Olkaria Domes (units I and II) with combined capacity 140 MWe being commissioned (operated by KenGen) - Production in Olkaria East expanded with Olkaria I units IV and V, combined capacity 140 MWe, in commissioning stages (operated by KenGen)

3. REINJECTION, REINJECTION CASES AND TRACER APPLICATION IN GEOTHERMAL SYSTEMS

Reinjection of spent geothermal fluids has become a major reservoir management Tool. It not only serves to maintain reservoir pressure, but also to increases energy extraction efficiency over the life of the resource. In most cases the spent geothermal fluid is much cooler than the geothermal fluid in the reservoir, these benefits depend strongly on locating injection in such a fashion that the thermal breakthrough within the reservoir does not occur in unanticipated manner. Procedure to optimizing an injection strategy to avoid premature thermal breakthrough can be iterative, a properly designed tracer test can be used to trace flow paths within the reservoir, and to predict the timing of thermal breakthrough. The onset of thermal breakthrough leads to operational problems, which may include plant output running below design capacity, an added cost of makeup wells, and/or modifications to field operations (Shook 1999)

Propagation of thermal front as examined by various researchers (e.g., Bodvarsson, 1972; Woods and Fitzgerald, 1993) for single-phase, porous medium, they showed that, due to the thermal inertia of the rock matrix, thermal front is proposed to lag behind the fluid front by a factor related to the volumetric heat capacity. In homogeneous media, one would expect a sharp transition from far-field temperature to injection temperature behind the injection front. In heterogeneous media, however, mixing of the injected fluids with in situ fluid results in both an earlier and more gradual decrease in production temperature. Such premature thermal breakthrough have been observed in various geothermal reservoirs, including Beowawe (e.g., Benoit and Stark, 1993) and The Geysers (e.g., Beall et al., 1994).

Tracer testing is used as tool for tracing flow within a geothermal reservoir (e.g., Beall et al., 1994; Kocabas et al., 1996; Rose et al., 1997) for the purpose of characterizing the geothermal system. By injecting a finite slug of tracer with injectate, fluid flow paths and mean residence times of injectate can be estimated. Knowledge of the flow field provides a means of identifying problems with, and optimizing injection. Through numerical simulation, one may further predict the onset of cooling in produced fluids.

Ghergut et al. (2010) discuss typical tracer test results obtained, by assuming a case of geothermal well doublet (injection-production) where the wells are intersecting one or more of parallel permeable features (fissure/fault zones) that constitute the flow channels of the reservoir. Assuming a steady dipole flow field when some solute tracer is introduced in the injection well, tracer breakthrough can be measured in the producing well and is often presented as breakthrough curves (BTC). The thermal breakthrough are more often too fast. They also point out that the heat transport predictions based on tracer-based estimated transport parameters can be inconclusive. In that the fracture densities derived from single or inter-well tracer tests may not be present on the reservoir scale. This can lead to an underestimation of reservoir lifetime, as the fluid residence times derived from inter-well tracer tests can led to uncertain estimation of thermal breakthrough time. They further second Kocabas and Horne (1987, 1990) in recommending the use of solute tracers only for determining inter-well residence times, and use of heat as a tracer for determining heat exchange area.

3.1 Reinjection experience in geothermal fields

Zarouk and O'Sullivan (2006) reviewed the world wide experience of reinjection in geothermal systems which considered a total of 92 electric power producing geothermal fields. Effect of reinjection on production is known to be dependent on the structure and geology, and the thermodynamic state of geothermal system. Geothermal systems can be generally classified into five categories as: Hot water, two-phase low-enthalpy, two-phase medium-enthalpy, two-phase high-enthalpy and two-phase vapour dominated systems. Table 2 below shows the classification based on reservoir temperatures and enthalpy of produced fluids.

TABLE 2: Classification of geothermal systems (Zarouk and O'Sullivan, 2006)

Geothermal system category	Temperature T (ºC)	Production enthalpy h (kJ/kg)
Hot water	T < 200	h < 943
Two-phase, low-enthalpy	220 < T < 250	943 < h < 1100
Two-phase, medium-enthalpy	250 < T < 300	1100 < h < 1500
Two-phase, high-enthalpy	250 < T < 330	1500 < h < 2600
Two-phase, vapour dominated	250 < T < 330	2600 < h < 2800

In the design of reinjection system, among other factors the most important factor is the location of injection well relative to production well for the particular injectate. Reinjected fluid can be relatively cold spent fluid or hot separated brine. Infield reinjection refers to locating reinjection wells close to the production wells within the hot part of the system. Whereas the outfield reinjection refers locating of reinjection wells further away from production wells and outside the hot part of the reservoir.

Two phase low enthalpy systems are more permeable when compared to the other systems. When production begins there is less pressure drop and less boiling occurs. Due to its nature, cold recharge from reservoir boundaries can easily flow into the reservoir. With its high vertical permeability cold recharge may flow down from above or extra hot recharge may flow into the reservoir from below with the balance between the two varying for different reservoirs. Examples illustrating the undesired effects of degradation of geothermal resource by thermal breakthrough caused by infield reinjection are Miravalles field (Gonzales-Vargas et al., 2005) and Ahuachapán geothermal field (Steingrimsson et al., 1991). The degradation effects are mitigated by moving the reinjection outfield.

Two-phase, medium-enthalpy systems contains hot water with limited boiling zones if any in its pre exploitation natural state condition. With less large fractures within less permeable rock matrix, boiling occurs at the feed zones in the wells as a result of large pressure drops associated with low reservoir permeability. Wells are expected to discharge medium enthalpy fluids. The boiling zones that develop as a result of production are typically localized and have high steam fraction which may increase with production. Localize vapour-dominated zone may develop.

Pressure drop in the reservoir induces boiling which leads to production of medium enthalpy mixture of water and steam. Conversion of thermal energy to electricity is more efficient for medium enthalpy fluid and there is less separated fluid to dispose. Pressure drop in the reservoir near production wells is normally buffered by boiling process. With utilization field the pressure declines rapidly until boiling occurs, then the pressure declines slowly. This pressure decline with boiling is associated with temperature decline resulting from heat extraction from rock matrix by water turning into steam (and extracting latent heat of vaporization in the process), decline is also attributed to cool recharge attracted to low pressure zone both from the sides and top of the reservoir (Grant and Bixley, 2011)

For two-phase medium enthalpy system infield reinjection of cold water will cause faster cooling of production wells and may suppress boiling and cause production enthalpy to drop to that of hot water. A system of this category does not run out of water like in the case of vapour dominated system and does not suffer from excessive pressure decline and may not require pressure maintenance as can be the case for hot water systems. Once the system has established equilibrium between production and natural discharge supplemented by boiling, infield reinjection may not be recommended. Adverse thermal breakthroughs are reported in two-phase medium enthalpy geothermal fields; e.g. in Cerro Prieto (Lippmann et al., 2004) and Tiwi (Sugiaman et al., 2004) reinjection was moved outfield.

Two phase high enthalpy systems consist of few major fractures (flow channels) in a low permeability matrix. In high enthalpy system volume and permeability of fractures are smaller than in medium enthalpy system and the boiling zones surrounding the production wells are drier and production enthalpies are higher. Natural recharge is limited by low permeability, for this case infield reinjection may be beneficial.

In two phase vapour dominated system the dominant mobile phase is steam. With continued production, the pressure decline leads to increased boiling of immobile water phase into steam which flows into the production wells. Vapour dominated two phase systems are known to have low permeability within the reservoir and in its surroundings. This ensures that there is no natural recharge of cold water flowing into the low pressure vapour dominated reservoir. After some years of production, parts of the reservoir may run out of the immobile water phase and becomes superheated. Infield reinjection of condensate or cold water injection directly above the depleted reservoir close to the production wells may be recommended. Cappetti and Cappattelli (2005) and Goyal (1999) report on successful implementation of the strategy in Larderello in Italy and Geysers in California, respectively, respectively.

3.2 Tracers in hydrothermal systems

Divine and McDonnell (2005) defines applied tracers as non-natural constituents that are intentionally introduced into a ground water system for the purpose of investigating subsurface flows. Tracers permit quantification of transport parameters and measurements of subsurface properties. Tracer tests directly measure the properties in-situ and can be used to investigate specific processes by selecting tracers with appropriate physiochemical properties. Tracer tests has been adopted in hydrogeology almost as a standard tool for aquifer characterization. By quantitative determination of rock and/or flow properties which among others are; ground water velocity, and hydraulic conductivity, dispersivities, porosities, transit time, volume of water and flow rates. These are the main inputs in the development of conceptual models. This information can be used for calibration or validation of numerical flow and transport deterministic models (Leibundgutet et al., 2009).

Axelsson et al (2005) discusses in detail the application of tracer tests and the qualitative interpretation of tracer test data. The prerequisites for a tracer tests are that: A tracer chosen should not be present in the reservoir or at a constant concentration much lower than the expected tracer concentration, should not react or absorb to the reservoir rocks and it should be easy- fast and inexpensive to analyse. The required amount of tracer to inject should be determined prior to the test. This depends on many factors; the chosen tracer detection limit, tracer background if it is present, injection rate, production rate and production wells involved, distances between the wells and the anticipated return rate can be slow or fast depending on the reservoir. Coarse estimates can be obtained by mass balance calculations considering the injection and production rates as well as recovery time span determined mainly by the distances and hydraulic connectivity of the wells involved which may not be known beforehand.

Tracers most commonly used in geothermal applications are in three categories; liquid-phase, steam-phase and two-phase tracers. Examples of liquid phase tracers are halides such as iodine or bromide, radioactive tracers such as iodide-125, iodide-131, fluorescent dyes like fluorescein and rhodamine, aromatic acids such as benzoic acid, and naphthalene sulfonates. Examples of steam-phase tracers are fluorinated hydrocarbons such as R-134a and R-23, and sulphur hexafluoride (SF_6). Examples of two-phase tracers for geothermal applications are tritiated water (HTO) and alcohols such as methanol, ethanol and n-propanol (Axelsson, 2013a). Fluorescein dyes has been successfully applied in low and high temperature geothermal systems (e.g. Axelsson et al., 1995; Rose et al., 1997 and 1999). It has the advantages of being absent in natural hydrological systems and very low levels of concentration detection. Adams and Davis (1991) in their study, showed that thermal decay for fluorescein is significant at temperatures above 200ºC and above 250ºC fluorescein decays too rapidly. And that the decay may be presented in a manner similar to that of radioactive isotopes (through the use of half-life). This principle may be applied to correct for the tracer decay in the interpretation of tracer tests in high temperature geothermal application.

In summary, a tracer test experiment involves; Carrying out a tracer background benchmarking in the area of interest, a fixed mass of tracer is injected in as short time as possible into injection wells. The geothermal reservoir should be preferably in a quasi-steady pressure state prior to the test so as to prevent major transients flow pattern (over pressure in the injection wells) of the reservoir different with the natural flow that otherwise would be prevailing. Sampling frequency is high in the beginning but reduces as test progresses. As illustrated in Figure 2 high sampling frequency is required to capture sharp tracer

return. But as time progresses depending on the reservoir, intermediate and slow tracer returns would be expected due to dispersion effects in the flow channels. Observations made on the tracer break through curves, such as in Figure 1, are; Tracer break through time which depends on maximum fluid velocity, time for concentration maximum, which reflects the average fluid velocity, the width of the tracer pulse, which reflects the flow path dispersion and the tracer recovery as a function of time.

3.3 Transport processes in hydrological systems/porous media

FIGURE 2: Figure showing typical fast, intermediate and slow tracer return profiles (Axelsson et al., 2005)

The transport processes in ground water systems are advection, dispersion and diffusion. In advection, the mean fluid velocity is the governing force moving the mass along the flow path and mass spreading in the steady state systems defined by the path lines for most systems.

The release of transported component (plume) will not spread at a constant rate because there are different paths around grains that flow could take. In practice there is usually a non-uniform velocity field as illustrated in Figure 3 below. This transport mechanism is referred to as dispersion. The transported component is spread to a larger area by the combined effects of diffusion and variable advection. Figure 3-d shows a longer torturous path L_e travelled by fluid in a porous media of length L.

FIGURE 3: Dispersion in ground water due to non-uniform velocity distribution and different flow paths (a, b), molecular diffusion (c) and Tortuosity due to longer flow paths in porous medium (d)

As illustrated in Figure 4, the velocity components in the flow field which in most cases is turbulent in nature gives rise to longitudinal and transverse dispersion

Transport modelling and discussion of the transport equations described in this chapter is based mostly on the work of Leibundgutet et al., (2009). By considering an aquifer containing only mobile water, transport of nonreactive non decaying solutes in ground water is described by three dimension dispersion equation in which dispersion is a tensor form and water velocity flow a vector form. The general three dimension transport equation for an ideal tracer is:
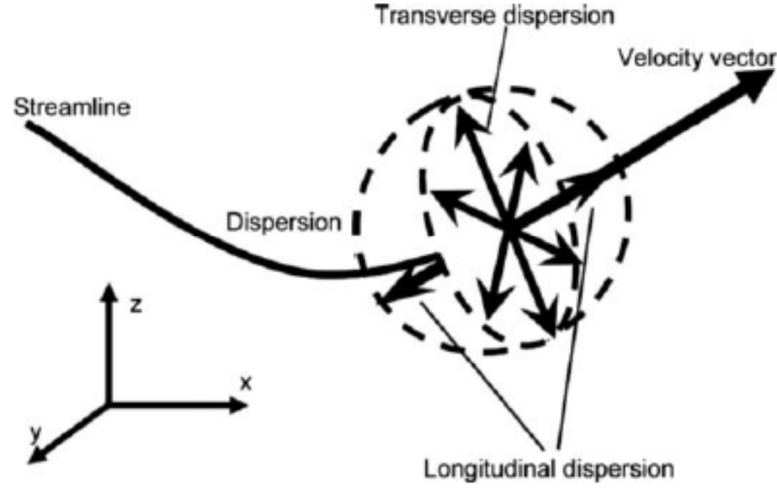
FIGURE 4: Schematic presentation of two transport processes – convection and dispersion – in the 3D case. The dashed line shows the concentration distribution of an ideal tracer injected instantaneously into the groundwater at beginning of the stream line.
From Leibundgutet et al., (2009)

$$\frac{\partial}{\partial x}\left(D_{xx}\frac{\partial C}{\partial x} + D_{xy}\frac{\partial C}{\partial y} + D_{xz}\frac{\partial C}{\partial z} - v_x C\right)$$
$$+ \frac{\partial}{\partial y}\left(D_{yx}\frac{\partial C}{\partial y} + D_{yy}\frac{\partial C}{\partial y} + D_{yz}\frac{\partial C}{\partial z} - v_y C\right) \tag{3.1}$$
$$+ \frac{\partial}{\partial z}\left(D_{zx}\frac{\partial C}{\partial x} + D_{zy}\frac{\partial C}{\partial y} + D_{zz}\frac{\partial C}{\partial z} - v_z C\right) = \frac{\partial C}{\partial t}$$

where *x, y, z* is the chosen co-ordinate system; C is the concentration of the solute in water; t is time; v_x, v_y, v_z are the x-,y-,z-components of velocity vector V and D_{ij} $with$ $(i, j = x, y, z)$ being the components of the dispersion tensor **D.**

Dispersion tensor:

$$D_{xx} = D_L\left(\frac{v_x^2}{v^2}\right) + D_T\left(\frac{v_y^2}{v^2}\right) + D_T\left(\frac{v_z^2}{v^2}\right) + \frac{D_m}{\tau}$$
$$D_{yy} = D_T\left(\frac{v_x^2}{v^2}\right) + D_L\left(\frac{v_y^2}{v^2}\right) + D_T\left(\frac{v_z^2}{v^2}\right) + \frac{D_m}{\tau} \tag{3.2}$$
$$D_{zz} = D_T\left(\frac{v_x^2}{v^2}\right) + D_T\left(\frac{v_y^2}{v^2}\right) + D_L\left(\frac{v_z^2}{v^2}\right) + \frac{D_m}{\tau}$$

$$D_{xy} = D_{yx} = (D_L - D_T)\left(\frac{v_x v_y}{v^2}\right)$$
$$D_{xz} = D_{zx} = (D_L - D_T)\left(\frac{v_x v_z}{v^2}\right) \tag{3.3}$$
$$D_{zy} = D_{yz} = (D_L - D_T)\left(\frac{v_z v_y}{v^2}\right)$$

where D_m is molecular diffusion coefficient of tracer in free water; τ is tortuosity factor of the porosity matrix; and D_L and D_T are longitudinal and transverse dispersion coefficients and are represented as:

$$D_L = \alpha_L v \quad D_T = \alpha_T v$$

Here α_L and α_T are longitudinal and trasverse dispersivities of the hydrodynamic dispersion respectively. They characterize the heterogeneity of the porous medium.

The mean water velocity v and tortuosity τ are:

$$v = \sqrt{v_x^2 + v_y^2 + v_z^2}$$

$$\tau = \frac{L_e}{L}$$

(3.4)

Solution to the general transport equation can be found by applying numerical techniques. Finite difference methods and finite element methods can be used as have been applied in numerical ground water modelling codes.

In granular porous medium assumed to be homogeneous, flow streamlines are parallel. When x axis is taken in the direction parallel to the flow lines, the velocity components v_y and v_z reduces to zero and the velocity vector is then $v = v_x$. The dispersion tensor $\boldsymbol{D}$ reduces to:

$$D_{xx} = D_L + \frac{D_m}{\tau}$$

$$D_{yy} = D_T + \frac{D_m}{\tau}$$

$$D_{zz} = D_T + \frac{D_m}{\tau}$$

(3.5)

The three dimension transport equation for steady state flow reduces to:

$$D_{xx} \frac{\partial^2 C}{\partial x^2} + D_{yy} \frac{\partial^2 C}{\partial y^2} + D_{zz} \frac{\partial^2 C}{\partial z^2} - v \frac{\partial C}{\partial x} = 0$$

(3.6)

Molecular diffusion is much lower in comparison to hydrodynamic dispersion for cases where the flow velocity is greater than 0.1 m in a day Leibundgutet al., (2009). This condition is expected to be met in flows along fractures in geothermal systems. Diffusion can play an important role in solute migration into stagnant fluid and fracture-matrix interaction (e.g.; Maloszewski et al., 1999, Pruess et al., 2000). The dispersion tensor $\boldsymbol{D}$ is then further reduced to $D_{xx} = D_L$ and $D_{yy} = D_{zz} = D_T$

3.3.1 One- and two-dimensional cases

For a tracer injected through the whole thickness of homogeneous aquifer like a fully penetrating well, the tracer is assumed to be vertically well mixed in the injection well. Injection well located at the origin x = 0 and y = 0, with the vertical concentration gradient:

$$\frac{\partial C}{\partial z} = 0$$

Taking x parallel to the flow direction and neglecting molecular diffusion, the transport equation becomes:

$$D_L \frac{\partial^2 C}{\partial x^2} + D_T \frac{\partial^2 C}{\partial y^2} - v \frac{\partial C}{\partial x} = \frac{\partial C}{\partial t}$$

(3.7)

This is the 2D transport equation for the case where transport is in the horizontal plane along the flow direction i.e. x-axis.

When the tracer is injected into water flowing into a column covering the whole cross section of the column perpendicular to the flow direction, a one-dimensional case arises. An example is injection into a well with thickness close to the width of the fracture. Taking x-axis along the flow direction the concentration gradients in y and z direction are both equal to zero:

$$\frac{\partial C}{\partial y} = \frac{\partial C}{\partial z} = 0$$

(3.8)

Equation 3.7 above reduces to the 1D transport equation:

$$D_L \frac{\partial^2 C}{\partial x^2} - v \frac{\partial C}{\partial x} = \frac{\partial C}{\partial t}$$

(3.9)

3.3.2 One-dimensional solution

Solution for the 1D transport Equation 3.10 is also known as the advection-dispersion equation for instantaneous tracer injection and is based on the following boundary conditions:

$$C(x = 0, t) = \frac{M}{Q}\delta(t)$$
$$C(x, t = 0) = 0$$
$$\lim_{x \to \pm\infty} C(x, t) = 0$$
(3.10)

Where M is the mass of tracer injected and Q is the volumetric flow rate through the column (injection rate). The solution for these initial conditions is as shown below (e.g.; Lenda and Zuber, 1970, Kreft and Zuber, 1978):

$$C(x, t) = \frac{M}{Q} \frac{x}{\sqrt{4\pi D_L t^3}} \exp\left\{ -\frac{(x - vt)^2}{4D_L t} \right\}$$
(3.11)

This is one of the solutions to transport equation that has been applied to match tracer return profiles (Axelsson et al., 1993, 1995, 2001) in a method known as de-convolution or inverse modelling. It can be applied to multiple flow channels like in layered porous medium.

The parameters v, D_L in Equation 3.11 can be determined from experimental data obtained by fitting the equation to the data. Maloszewski and Zuber (1990) showed that in closed systems for 1D case the relative mass recovery can be calculated as a function of time t. This is the ratio of tracer recovered M_R to the mass injected M:

$$RR(t) = M_R/M = Q \int_0^t C(t)dt \, /M$$
(3.12)

The method of moments (e.g.,Kreft and Zuber, 1978, Malosweski and Zuber,1985,1992b, Maloszewski, 1994) is often used to analyse tracer test data. The 1st momment M_1 of the tracer curve C(t) is:

$$M_1 = \int_0^\infty t^1 C(t)dt$$
(3.13)

After obtaining the tracer concentration curve for sufficiently long period possibly the concentration has peaked and tailed off to the background concentration of water. Two key mathematical descriptors, centre of gravity $\bar{t}$ which is the mean transit time t_t and the variance of the tracer concentration curve δ_t^2 are then calculated:

$$\bar{t} = t_t = \frac{\int_0^\infty tC(t)dt}{\int_0^\infty C(t)dt} = \frac{M_1}{M_0}$$
(3.14)

$$\delta_t^2 = \frac{\int_0^\infty (t - \bar{t})^2 C(t)dt}{\int_0^\infty C(t)dt} = \frac{M_2 M_0 - M_2}{M_0^2}$$
(3.15)

These two descriptors can be used to estimate the transport parameters in the 1D case where the relationships below are then used

Mean transit time $\bar{t} = x/v$
Dispersion parameter:

$$\alpha_L = \frac{x}{2}\left(\frac{\delta_t}{\bar{t}}\right)^2 \quad or \quad P_D = \frac{\alpha_L}{x} = \frac{1}{2}\left(\frac{\delta_t}{\bar{t}}\right)^2$$
(3.16)

3.3.3 Double porosity medium

Flow in fractures in a fissured system with low permeability matrix, tracer transport can be modelled with double porosity model. Figure 5 below shows a conceptualized model for such a system. A system of parallel identical fractures equally distributed in a matrix are assumed to represent the fractured aquifer (Sudicky and Frind, 1982). The fractures have aperture 2b filled with mobile water. Matrix has porosity ϕ_m and in it there is only immobile water. The ratio of fracture aperture to fracture spacing L is defined as effective fracture mobile porosity ϕ_f (2b/L).
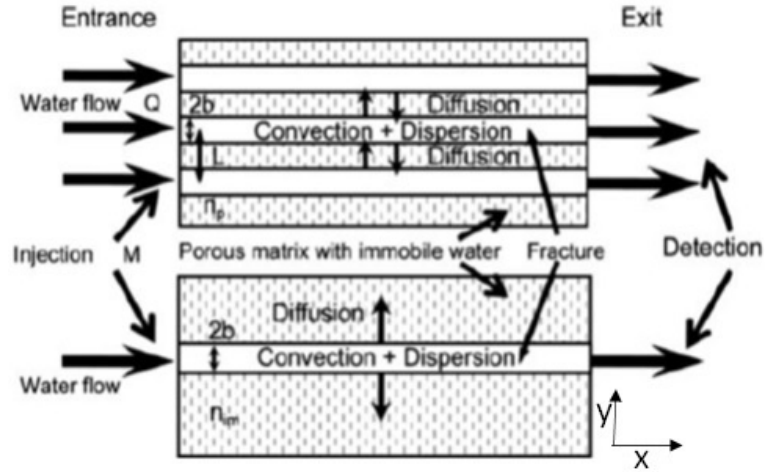
FIGURE 5: Idealized model of tracer transport in a fractured aquifer consisting of parallel fractures (top), or a single fracture (bottom), with in each case a porous matrix with immobile water. Transport of an ideal tracer (non-sorbing or non-decaying) in this model can be described by the equation below (Maloszewski and Zuber, 1985, 1990)

The tracer is transported in the fracture by convection v and dispersion D and there is, at the same time, a loss (sink term) due to diffusion through the fracture walls into the immobile water in the matrix. In Figure 5 an aquifer consisting of a single fracture situated in an infinitely large matrix is shown.

Within the fracture:

$$\frac{\partial C}{\partial t} + v\,\frac{\partial C}{\partial x} - D\,\frac{\partial^2 C}{\partial x^2} - \frac{\phi_m D_P}{2b}\frac{\partial C_m}{\partial y}\bigg|_{y=b} = 0 \ \ for\ 0 \leq y < b \tag{3.17}$$

And within the matrix (diffusion):

$$\frac{\partial C_m}{\partial t} - D_P\,\frac{\partial^2 C_m}{\partial y^2} = 0 \ \ for\ b \leq y < \infty \tag{3.18}$$

Where $C(t)\ and\ C_m(t)$ are the tracer concentrations in fracture (mobile) and in matrix (immobile) water, respectively, D_P is the effective diffusion coefficient in immobile water in porous matrix while v is the mean water velocity in the fracture.

The equation above has the following solution, as solved by Maloszewski and Zuber (1985, 1990), for instantaneous tracer injection:

$$C(t) = \frac{aM\sqrt{t_0}}{2\pi Q\sqrt{P_D}}\int_0^t exp\left[-\frac{(t_0 - \xi)^2}{4\xi t_0 P_D} - \frac{a^2\xi^2}{t - \xi}\right] \tag{3.19}$$

where ξ is an integration variable and a is the diffusion parameter equalling:

$$a = \frac{\phi_m\sqrt{D}_P}{2b}, \quad P_D = \frac{\alpha_L}{x} = \frac{D_L}{vx}, \quad t_0 = \frac{x}{v} \tag{3.20}$$

4. BACKGROUND OF NUMERICAL MODELLING WITH TOUGH2

Geothermal Reservoir numerical simulation tool, iTOUGH2 (Transport of Unsaturated Groundwater and Heat, it is a multi-phase, multi-component codes developed at the Lawrence National Berkeley Laboratories in California (Pruess et al., 1999).) is used. The code solves the heat (energy) transfer equation and mass conservation equations for every element (Grid) for the gridded domain (Reservoir).

4.1 Forward model

TOUGH2 is a general purpose numerical simulator for non-isothermal flow of multi-component, multi-phase fluids in one, two or three dimensional porous and fractured media (Pruess et al., 1999). The basic mass conservation equations governing this kind of flow can be written in the form:

$$\frac{d}{dt}\int_{V_n} M^k dV_n = \int_{\Gamma_n} F^k . n d\Gamma_n + \int_{V_n} q^k dV_n \tag{4.1}$$

Integration is over an arbitrary subdomain V_n of the flow system under study, which is bounded by closed surface Γ_n. Quantity M appearing in the accumulation term represents mass or energy per volume, with $k = 1, \dots, NK$ for mass components (like water, air or solutes-tracer) present in the flow system being modelled and $k = NK + 1$ for heat component being transported. F denotes the mass or heat flux, q denotes sinks and sources while n is a normal vector on the surface element $d\Gamma_n$, pointing inwards into V_n. Equation 4.1 expresses the fact that the rate of change of fluid mass in V_n is equal to the net inflow across the surface of V_n plus net gain from the fluid sources.

The general form of the mass accumulation term for multi-phase, multi-component with non-sorbing components system is:

$$M^k = \emptyset \sum_{\beta} S_\beta \rho_\beta X_\beta^k \tag{4.2}$$

In the equation above, the total mass of the component k is obtained by summing over the fluid phases β (that is liquid, gases). $\emptyset$ is the porosity, S_β is the saturation of the phase β (the fraction of pore volume occupied by that phase), ρ_β is the density of phase β and X_β^k is the mass fraction of component k present in phase β.

Similarly the heat accumulation in the multiphase multicomponent system is:

$$M^{Nk+1} = (1 - \emptyset)\rho_R C_R T + \emptyset \sum_{\beta} S_\beta \rho_\beta u_\beta \tag{4.3}$$

where ρ_R and C_R are grain density and specific heat of the rock respectively, T is temperature and u_β is specific internal energy in phase β.

Advective mass flux is the sum over phases:

$$F_{adv}^k = \sum_{\beta} X_\beta^k F_\beta \tag{4.4}$$

And individual phase flux is given by a multiple version of the Darcy's law:

$$F_\beta = \rho_\beta u_\beta = -k \frac{k_{r\beta}\rho_\beta}{\mu_\beta}\left(\nabla P_\beta - \rho_\beta g\right) \tag{4.5}$$

u_β is the Darcy velocity (volume flux) in phase β, k is absolute permeability, $k_{r\beta}$ is the relative permeability to phase β, μ_β is the viscosity while P_β is the fluid pressure in phase β normally obtained by summing the pressure of a reference gas phase and the capillary pressure of that phase. g is a vector of gravitational acceleration.

Heat flux includes conductive and convective components:

$$F^{Nk+1} = -\lambda \nabla T + \sum_\beta h_\beta F_\beta$$

(4.6)

where λ is thermal conductivity and h_β is the specific enthalpy in phase β.

4.1.1 Diffusion

In addition to advection Darcy flow presented by Equation 4.4, mass transport can occur by diffusion and hydrodynamic dispersion as follows:

$$F_{dis}^k = -\sum_\beta \rho_\beta \overline{D}_\beta^k \nabla X_\beta^k$$

(4.7)

Hydrodynamic dispersion tensor is given by:

$$\overline{D}_\beta^k = \overline{D}_{\beta,T}^k I + \frac{\left(D_{\beta,L}^k - D_{\beta,T}^k\right)}{u_\beta{}^2} u_\beta u_\beta$$

(4.8)

where longitudinal and traverse dispersion coefficients respectively are:

$$D_{\beta,L}^k = \phi\, \tau_0 \tau_\beta d_\beta^k + \alpha_{\beta,L} u_\beta$$
$$D_{\beta,T}^k = \phi\, \tau_0 \tau_\beta d_\beta^k + \alpha_{\beta,T} u_\beta$$

(4.9)

d_β^k is the molecular diffusion coefficient "diffusivity" for component k in phase β. $\tau_0 \tau_\beta$ is the turtuosity which includes a porous medim dependent factor τ_0 and a coefficient τ_β which is dependent on phase saturation S_β. α_L and α_T are longitudinal and trasveres dispersivities.

Molecular diffusion in all phases is part of standard TOUGH2 code. Mass flux from molecular diffusion alone is obtained by setting $\alpha_L = \alpha_T = 0$ in the hyrodynamic dispersion tensor. Fickian diffusive mass flux is given by:

$$f_\beta^k = -\phi\, \tau_0 \tau_\beta \rho_\beta d_\beta^k \nabla X_\beta^k$$

(4.10)

∇X_β^k is the mass fraction gradient the driving force for diffusion.

4.1.2 Space and time discretization

For numerical simulations, the continuous space and time must be discretized. The mass and energy balance Equation 4.1 is discretized in space by introducing volume and area averages. The mass and heat accumulation term becomes:

$$\int_{V_n} M dV = V_n M_n$$

(4.11)

while the source and sink term becomes:

$$\int_{V_n} q^k dV_n = q_n V_n$$

(4.12)

where M_n and q_n are the average value of the two mass and energy balance terms over V_n.

The total flux crossing the interfaces can be approximated by discrete summation as:

$$\int_{\Gamma_n} F^k . n d\Gamma = \sum_m \int_{A_{nm}} F^k . n d\Gamma = \sum_m A_{nm} F_{nm}$$

(4.13)

F_{nm} is the average over surface segment A_{nm} between the volume element V_n and V_m. The discretized flux corresponding to the basic Darcy flux term Equation 4.5 is expressed in terms of averages over parameters for volume elements V_n and V_m as follows:

$$F_{\beta,nm} = -K_{nm} \left[\frac{K_{r\beta}\rho_\beta}{\mu_\beta} \right]_{nm} \left[\frac{P_{\beta,n} - P_{\beta,m}}{D_{nm}} - \rho_{\beta,nm} g_{nm} \right]$$ (4.14)

nm denotes a suitable averaging at the interface between the grid blocks n and m. $D_{nm} = D_m + D_n$ which is the distance between the nodal points in n and m while g_{nm} is the component of gravitational acceleration of gravity in the direction of m to n.

The basic geometric parameters used in space discretization are illustrated in Figure 6.
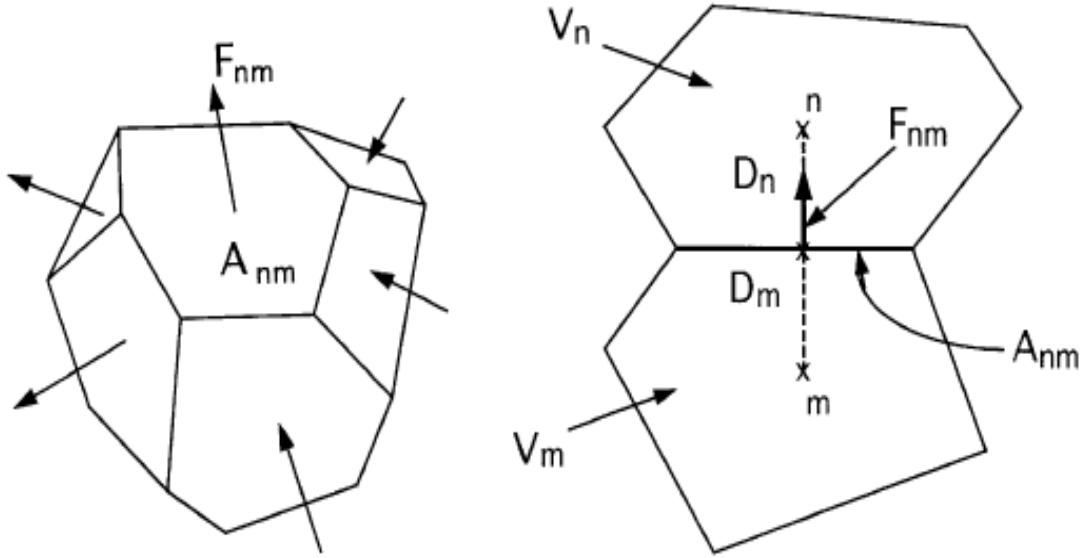
FIGURE 6: Space discretization and the geometry data (Pruess, 1999)

Substituting Equations 4.11, 4.12 and 4.13 into Equation 4.1 results to a set of first-order ordinary differential equations in time:

$$\frac{dM_n^k}{dt} = \frac{1}{V_n} \sum_m A_{nm} F_{nm}^k + q_n^k$$ (4.15)

Time is discretized as a first order finite difference. The flux, sink and source terms on the right hand side of the Equation 4.15 are evaluated at the new level $t^{k+1} = t^k + \Delta t$, to obtain the numerical stability needed for efficient calculation of multiphase flow. The time discretization results to Equation 4.16 below with $R_n^{k,k+1}$ introduced as residuals:

$$R_n^{k,k+1} = M_n^{k,k+1} - M_n^{k,k} - \frac{\Delta t}{V_n} \left\{ \sum_m A_{nm} F_{nm}^{k,k+1} + V_n q_n^{k,k+1} \right\} \cong 0$$ (4.16)

Equation 4.16 is solved by Newton-Raphson iteration by introducing an iteration index p and expand the residual at iteration step $p + 1$ in a Taylor series in terms of those at index p:

$$R_n^{k,k+1}(x_{i,p+1}) = R_n^{k,k+1}(x_{i,p}) + \sum_i \frac{\partial R_n^{k,k+1}}{\partial x_i}\bigg|_p (x_{i,p+1} - x_{i,p}) = 0$$ (4.17)

Retaining only terms up to first order results to:

$$-\sum_i = \left. \frac{\partial R_n^{k,k+1}}{\partial x_i} \right|_p (x_{i,p+1} - x_{i,p}) = R_n^{k,k+1}(x_{i,p}) \tag{4.18}$$

All terms $\partial R_n/\partial x_i$ in the Jacobian matrix are evaluated by numerical differentiation to achieve maximum flexibility in the manner in which various terms in the governing equations may depend on the primary thermodynamic variable. Iterations are done until all the residuals are reduced below a present convergence tolerance typically chosen as $\varepsilon = 10^{-5}$:

$$\left| \frac{R_n^{k,k+1}}{M_n^{k,k+1}} \right| \leq \varepsilon \tag{4.19}$$

5. THE OLKARIA EAST AND SOUTHEAST CASE STUDY

Here the case study of the East and Southeast parts of the Greater Olkaria geothermal field are discussed.

5.1 Physical characteristics

5.1.1 Regional geology

The Olkaria volcanic system is located south of Lake Naivasha on the southern segment of the Kenyan rift. The Kenyan rift is part of the series which runs several thousands of kilometres long and up to 40-60 km wide, and in aligned successions of adjacent individual tectonic basins (rift valleys). The Kenyan rift is an active continental rift zone with divergent plate boundary, where the Somali and the Nubian plates are drifting apart at an average rate of about 2 cm per year, thus creating a thinner crust (KenGen, 1980).

Omenda (2002) classifies the subsurface geology of the Olkaria geothermal field into six broad lithostratigraphic groups based on age, tectono-stratigraphy, and lithology as deduced from data from the numerous deep wells drilled in the area. The formation categories are Protezoic "basement", Mau tuffs, plateau trachytes, Olkaria basalts, and upper Olkaria volcanics (Figure 7).
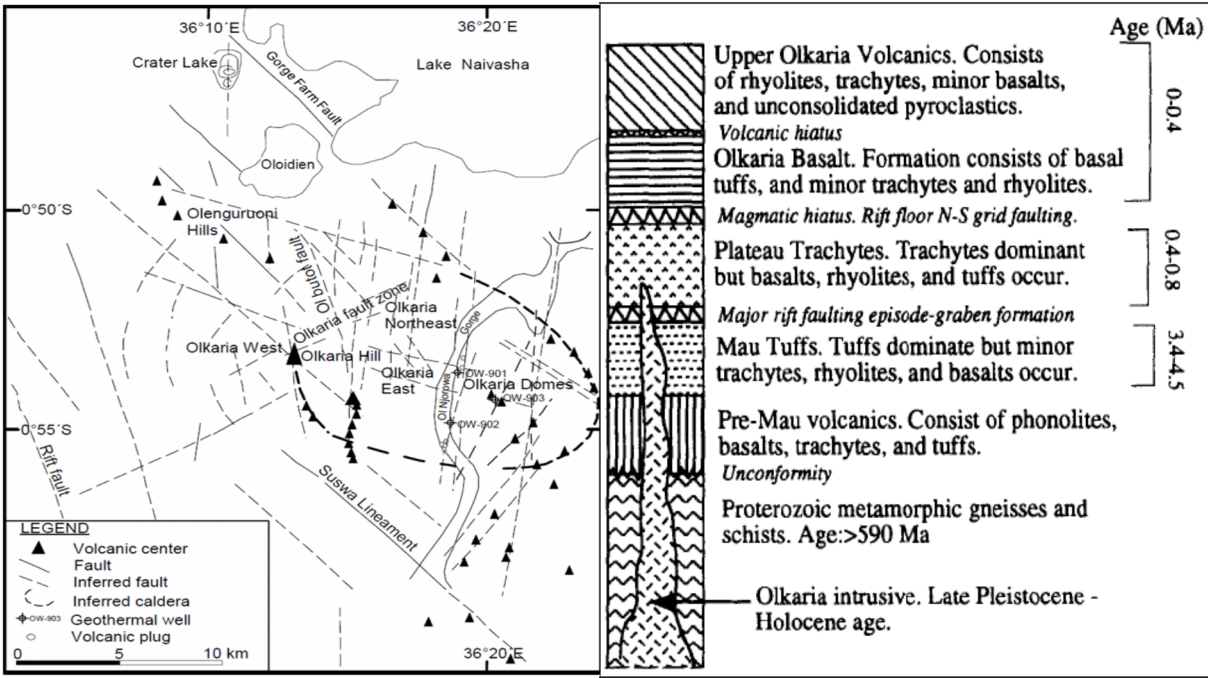
FIGURE 7: Geological structures and stratigraphic column of the Olkaria volcanic complex
(Omenda, 1998)

The Mau tuffs are considered to be the oldest rocks and are commonly encountered in the area west of Olkaria Hill (Figure 7). The rocks vary in texture from consolidated to ignimbrites, and are the main geothermal reservoir rocks on Olkaria West field as seen in the drill cuttings from boreholes in the area. Plateau trachytes are of Pleistocene age and are composed of mainly trachytic lavas with minor basalts, tuffs and rhyolites. This formation is known to host the geothermal reservoirs for the Olkaria East and Northeast fields. The thickness of the formation is estimated to be more than 1.5 km as observed in the boreholes drilled in the East field (Odongo, 1986 and Omenda, 1994). Olkaria basalt consists of basaltic flows, minor pyroclastic deposits and trachytes. This formation is believed to form the cap rock for the Olkaria geothermal system (Haukwa, 1984; Ambusso and Ouma, 1991). Its thickness varies from 100m to 500m. Underlying the upper volcanics, the formation is composed of numerous thin basaltic flows separated by thin layers of tuffs, minor trachytes and occasional rhyolites. It has been penetrated by almost all wells in the east and north east fields at nearly constant elevation. The sharp temperature

increase occurring below the formation, attributed to combined heat convection and conduction in the formation underlying it, further confirms that the Olkaria basalt is the cap rock for the geothermal system.

The upper Olkaria formation consists of comendite lavas and their pyroclastics equivalents, ashes from Suswa and Longonot volcanoes and minor trachytes and basalts, with comendite being the dominant rock (Thompson and Dodson. 1963; Clarke et al., 1990). These rocks form the formation from surface down to a depth of about 500 m.

5.1.2 The main faults/tectonic setting of the Olkaria volcanic complex

The ENE-WSW Olkaria Fault is one of the major faults running through the Olkaria geothermal area. The fault manifests itself on the surface as a linear zone of intense geothermal manifestation and highly altered grounds about 50-100 m wide (Omenda 1998)

The George Farm Fault runs NW-SE from Lake Naivasha and extends to Olkaria Domes area (Langat, 2004). This fault is considered to be a major recharge zone for the Greater Olkaria Geothermal System.

An E-W system of fissures and faults is believed to control the bulk of fluid movement and permeability properties of the reservoir rocks in the Olkaria west and domes areas (Odongo, 1993) this is noted in Figure 7, a major fault runs from Olkaria hill eastwards ending up below the younger lava to the east of Ol Njorowa gorge

The most recent structures in the Olkaria volcanic complex are N-S and NNE-SSW faults which are associated with the latest tectonic activities (Omenda, 1998). Example of these faults are the Olkaria fracture and Olobutot fault zones. The dyke swarms that have been exposed in the Ol Njorowa Gorge trend in north-north-easterly direction, further attesting to the recent activation of faults with that trend.

5.1.3 Geophysical studies

Several geophysical studies have been conducted in Olkaria. The purpose of which has been to identify, delineate and characterize the resource. Geophysical methods include resistivity surveys such as Schlumberger soundings, head-on profiling, TEM and MT as well as magnetic surveying, seismology and finally gravity surveying. The findings have been discussed in the detailed studies that have been conducted during the course of resource exploration and development. Combined interpretation of the results from these methods are presented in the form of a conceptual model discussed in Section 5.5.1. Figure 15 in that section shows a resistivity map at 1000 m a.s.l. of the greater Olkaria field based on 1D inversion of TEM-resistivity soundings. This map, shows a main NW-SE trending low resistivity anomaly and subsurface resistivity anomalies associated with the Olkaria East, Northeast and West sections, in the same map also shown is the micro earthquake epicentres associated with the heat sources. Figure 16 shows the contour map of the attenuating bodies beneath Olkaria field superimposed with the temperature contours to highlight the heat sources and the flow system.

5.1.4 Hydrogeology

Ground water occurrence in Olkaria is controlled by complex tectonics and geological formations. Faults are considered to have two effects on fluid flow; they may facilitate and (or) enhance flow by providing channels of high permeability or they may provide barriers to flow by offsetting zones of relatively high permeability (Chorowicz, 2005).

Within the rift valley, the main direction of faulting is along the axis of the rift, this has a significant effect on the flow across the rift. There is a high hydraulic gradient developed across the rift escarpments that can be attributed to the faults acting as zones of low permeability.

Most of litho-stratigraphic contacts and fissure zones covering the rift floor constitute the highly permeable aquifers. In the recent optimization study carried out in Olkaria (Axelsson et al., 2013a and

2013b) geothermal system has two recharge sources. There are deeper aquifers, indicated by isotope data studies, showing recharge to be from northern parts of the Great rift system, while shallow aquifers are mainly recharged by fissure systems, i.e. the Ololbutot fracture zone and Gorge Farm fault. The fault systems conduct the recharge water from western Rift escarpment.

The relative location/elevation of Lake Naivasha in relation to other areas within the rift floor, the high gradients drive the lake's outflow to the south and marginal outflow to the north. Structural features such as faults often optimize storage, transmissivity, and recharge, with most significant of these occurring in places that are adjacent to or within a surface drainage system (Driscoll, 1986).

5.1.5 Well data

Vast amount of data has been collected over the production history of the field (Appendix A). The borehole temperatures and pressure have been obtained with Kuster mechanical tools. Production well mass flows rates and enthalpy are obtained during well discharge and production well monitoring. Data used in the study are adopted from the 2011/2012 optimization study of the geothermal field by the Mannvit/ISOR/Vatnaskil/Verkis consortium (Axelsson et al., 2013a and 2013b)

5.2 Field development

Production in Olkaria geothermal field has been gradual. As discussed in Chapter 2 major increment in production is ongoing and the ability of the reservoir to sustain the expansion is critical. Numerical modelling has been embraced as a guiding tool in the geothermal field management from the beginning to date. Discussed in this chapter are the observations that have been made over the production period the field has been in operation. These observations have been incorporated into evolution of conceptual and numerical models.

The understanding of the reservoir in 1976 by Sweco and Virkir, the consultants at that time, Olkaria East reservoir is a free convecting hot water reservoir. Beneath the reservoir cap rock is a thin steam cap (50-100m) thought to be generated due to the lateral flow caused by the observed north south pressure gradient of 11 bars/km. Underlying the steam cap is a liquid dominated reservoir following a boiling with depth relationship (Bodvarsson et al., 1987). The production wells were then designed to tap and extract steam and water from the steam zone and the uppermost part of the water reservoir. With time, these shallow producing wells upset the stationary natural conditions with pressure declining. The drawdown of pressure lead to extensive boiling in their vicinity resulting in increase in enthalpy and dryness fraction.

5.3 Production history of Olkaria East field

The reservoir response to increased production with time is discussed in the following sub-sections.

5.3.1 Production and pressure response

Bi-annual output monitoring is done in Olkaria wells that are delivering steam to the power plants. This is done to observe important changes taking place in the reservoir. These include changes in reservoir temperature and pressure, enthalpy and mass output changes as well as cyclic behaviour of wells. Careful monitoring techniques help to map out thermodynamic and chemical changes before they cause adverse effects in the reservoir. Initially, 23 wells supplied steam for the first three units but as time progressed, some wells declined in output and had to be retired As seen in Figure 8 below, in 1994, power generation had declined by 35% due to steam output decline from most of the producing wells (Kamau and Odeny, 1997) To restore to original capacity of the plant, make up wells were required. Because of the high cost of drilling and connection of makeup wells, series of injection experiments were also undertaken to evaluate the feasibility of reinjection.

Figure 8 shows the field production history, the values of mass rates are bi-annual averages. Well OW-05 was deepened in 1998 from 900 m to 2200m, with good results (selected well's production histories in the Appendix F). The output from field increased after connection of make-up wells and deepening of OW-05. The increase in mass output is attributed to drilling of deeper wells that tapped deep permeable production zones which produced high mass flows and were more liquid dominated than the shallow steam dominated zones tapped by the older shallow wells. The pressure decline in the Olkaria East field has been moderate. Drawdown data come from 5 wells, two of those, wells OW-8 and OW-21, have the longest data series and are used as the main observation wells. Observed drawdown is 15 bars (Figure 8). It is less than the earlier thought 25 bars (Ofwona 2002), which was based on a single well, OW 08 that had previously been in production. The 10 – 15 bars decline is representative of the field when more wells are considered.
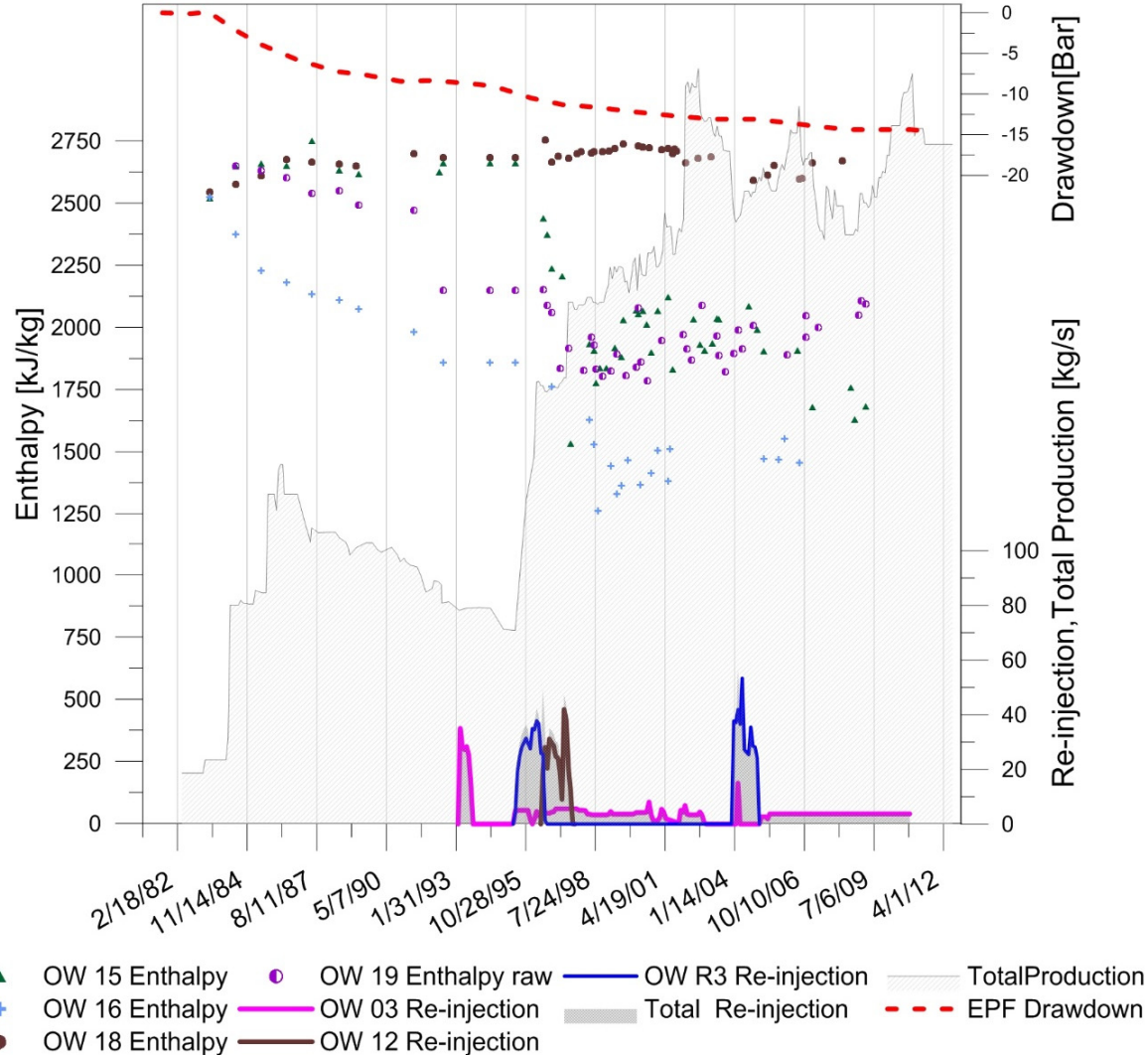
FIGURE 8: Olkaria East field: Total production flow, reinjection flows, pressure draw down at 640 m a.s.l. and injection effects on selected producing wells' enthalpy

5.3.2 Injection history and enthalpy changes

Both cold and hot re-injection has been applied on a small scale in Olkaria and to a larger extent had positive effects. Wells in the vicinity of reinjection in the Olkaria East field have responded with increased or stabilized outputs (more well production history figures in (Appendices F and G). Cold injection has been done intermittently due to breakthroughs leading to drop in enthalpies but after few months of stoppage, the wells recover and increase their outputs. Figure 8 shows the reinjection done in Olkaria East field with effects on selected producing wells' enthalpy and steam fraction. Hot and cold injection has been applied in well OW-03, while OW-06 is a cold reinjection well, utilizing the cooling

towers blow-down from the Olkaria I power plant. About 100 tons/hr (27.8 kg/s) of cold water (20°C) from L. Naivasha was injected into the reservoir with tracer in well OW-12 from July 1996 to August 1997. The figure also shows the decline in enthalpies in wells OW-15, 16, and 19 in 1997 due to cold injection in well OW-12.

5.3.3 Enthalpy changes

The enthalpy contour plots in Figure 9, shows enthalpy from 1985 to 2012. From Figure 9 a, in 1985 the centre of the field around wells OW-05, OW-10, OW-15, OW-18, OW-19 and OW-20 had the highest enthalpy as these are the wells that are tapping the steam cap. In FIGURE 9 b, contour plots for year 2001 after connection of makeup wells to steam gathering system. There has been increase in the enthalpy around the centre of the field, which extends towards the northern and western part of the field. The enthalpy contour plots shows that the centre of the field around wells OW-10, OW-18, OW-20 and OW-24 &28, 31 and 33 has the highest enthalpy. This shows that most part of the field has experienced pressure drawdown resulting in boiling. Little enthalpy change is observed in the southern part of the field, this could be as a result of recharge of cooler fluids. Enthalpy contour plots for the year 2012 (Figure 9, c) is similar to the year 2001 contour plot but the enthalpy values are higher. There is increase in the area with the high enthalpy which shows that most part of the field has experienced pressure drawdown resulting in still increased boiling.
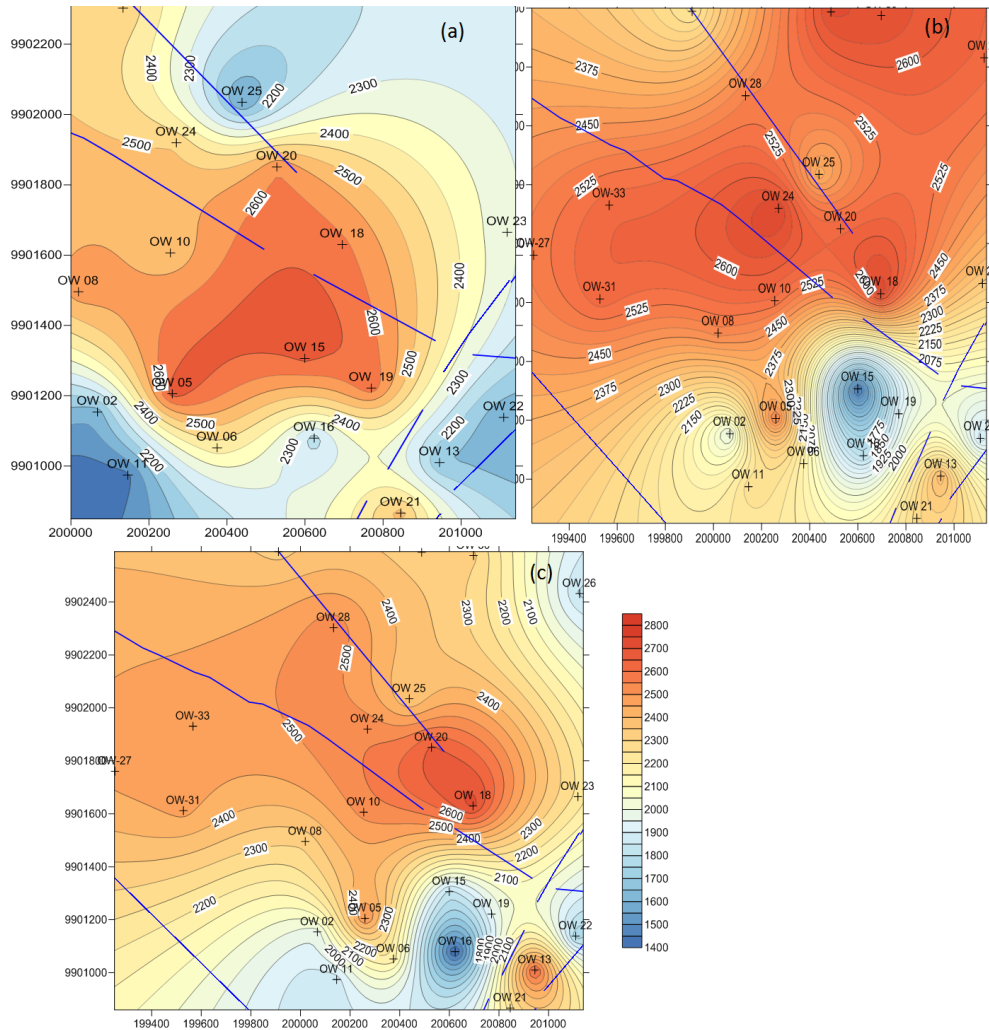

FIGURE 9: Contour maps showing enthalpy evolution with time for the Olkaria East field; enthalpy for 1985 - a, 2001 - b and 2012 - c

5.3.4 p-h diagram for the field production history

The field production history and the systems response are plotted in the pressure – enthalpy (p-h) diagram in Figure 10. The figure shows the total enthalpy at the well head for selected wells at four time-points over the production history. The total enthalpy of the flowing wells at the well head pressure are plotted for from the beginning of production in 1983, 1985, and 2002 and in 2006. The wells have been operated at well head pressure of 5-7 bars and the steam fraction of 40-95% at the well head for the discharging wells
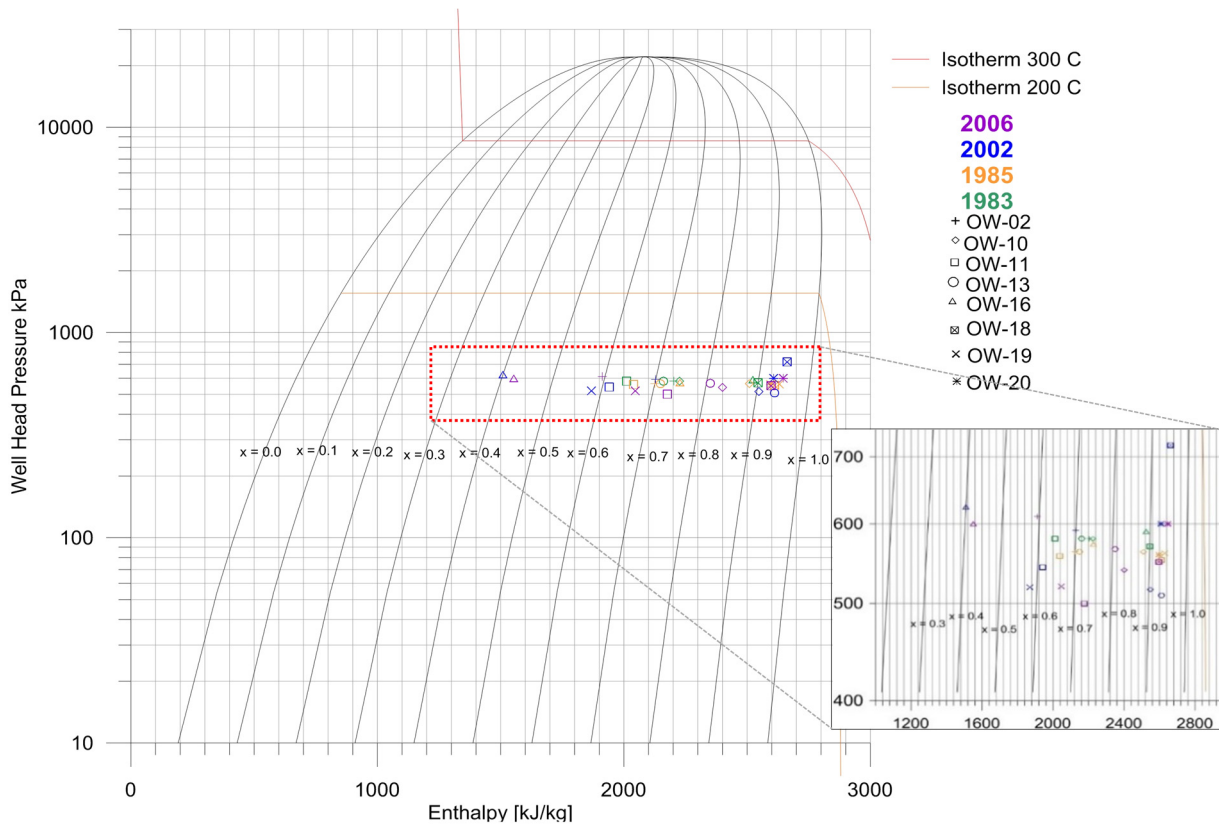

FIGURE 10: Plot of pressure vs. enthalpy (p-h) diagram at the well head for selected East field wells for years 1983, 1985, 2002 and 2006

5.4 Tracer tests

The tracer test considered in this study is the tracer injection test done in 1996 to 1997. Cold water was injected into well OW 12 from June 1996 to September 1997 at an average rate of 100 tons/hr (27.8 Kg/s) for a duration of 416 days. 500 kg of fluorescein dissolved in 20,000 litres were injected in August 1996 after two months of injection. Wells surrounding injection well OW-12 were monitored for tracer returns and changes in discharge characteristics. Appreciable tracer returns were noted in wells OW-15, 18 and 19 (Table 3). The recovery break through curves are as plotted in the Figure 11. The enthalpy drop noted in wells OW-18 and OW-15 indicates the presence of a direct reservoir connection. The results of the test were published in a report by Mawongo (2004) where single fracture model was considered and the dipole of OW-12 and OW-19 modelled.

5.4.1 Tracer returns and post processing of fluorescein concentrations

Fluorescein is an organic dye used to trace flow paths of injected fluids through geothermal reservoirs. Its advantages are low detection levels, ease of analysis and absence in natural hydrological systems (Axelsson, 2013a and 2013b). Thermal degradation of fluorescein, the main disadvantage associated with its use, has been studied up to 300°C in hydrothermal autoclaves at various fluid compositions, pH

and oxygen concentrations. At temperatures below 210°C, fluorescein is a suitable tracer for use in geothermal reservoirs (Adams and Davis, 1991). Its ability to decay at elevated temperatures is also advantageous in that it can be repeatedly used as an inexpensive and easy to analyse tracer in the same field for tests lasting a few months.

TABLE 3: Well feed zones, lengths of flow paths from injection depth in OW-12 and the injection rate for OW 12 and production rates for flowing wells during tracer test period

Well no.	Feed zones (m)	Feed zone depth	Flow channel	Production/ injection [kg/s]
	L : Liquid dominated S: Steam dominated		x Distance from OW12	
OW-12	575 (S), 750 (S); 850-900 (L)	800		27.78
OW-15	700-800 (S)	800	217.8	6.50
OW-18	540-600 (S)	600	281.5	7.00
OW-19	1000-1050 (L)	1050	451.1	6.00

Figure 11 presents tracer recovery curves in the East production field. Tracer breakthrough time ranged from 3 days in well OW-15, 20 days in well OW-18, to 14 days in well OW-19. Well OW-15 recorded the highest tracer concentrations at an early time. Tracer concentrations observed in wells OW-18 and OW-19 were comparable.
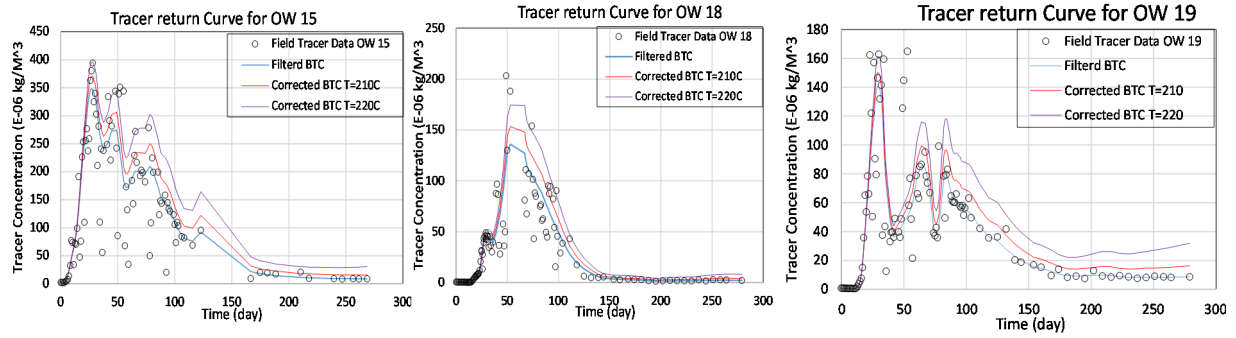

FIGURE 11: Measured, smoothed and thermal decay corrected tracer recovery curves (break through curves) for wells OW-15, OW-18 and OW-19

The breakthrough curves were smoothed using Matlab filter "rloess" (locally weighted scatter plot smooth) which uses locally weighted linear regression to smooth data. Each smoothed value is determined by neighbouring data points defined within the span. The process is weighted because a regression weight function is defined for the data points contained within the span. The span was specified to be 10% of the data points in the data set Mathworks. (2011)

5.4.2 Thermal degradation and decay correction

Study on the kinetics of fluorescein decay and their application on geothermal systems as a tracer by Adam and Davis (1991) showed that fluorescein decays by less than 10% in one month at temperatures below 210°C. Fluorescein at constant pH decays according to a first order rate law given by:

$$C_t = C_0 . e^{kt} \tag{5.1}$$

Where C_t = Concentration of fluorescein after heating (mg/l);
          Co = Initial concentration (mg/l);
          t = Time (s); and
          k = First order rate constant (decay parameter) (s^{-1}).

The temperature dependent decay parameter k can be described by an Arrhenius relationship as in the equation below (Rose et al., 2000; Adams and Davis, 1991):

$$k = A \exp\left\{\frac{-E_a}{RT}\right\} \tag{5.2}$$

where 　　 *Ea* 　 = Energy of activation (J/mol);
　　　　　 A 　 = Pre-exponential constant (s^{-1});
　　　　　 T 　 = Sample absolute temperature (K); and
　　　　　 R 　 = Universal gas constant = 8.31 J/mol K

In their experiment fluorescein was subjected to temperatures up to 300°C. And the activation energy *Ea* and the natural logarithm (ln) of the pre-exponential constant *A* were estimated as 143,300 (±6,620) J/mol and 18.25 (±1.44) s^{-1}, respectively.

In the Olkaria East production field, static downhole temperatures encountered in the reservoir are in the range of (220 – 300) °C and the flowing temperatures vary from 180°C to 250°C. Reservoir temperature is higher than 210°C at which the decay of fluorescein is significant. Values of activation energy (*Ea*) and the pre-exponential constant *A* were adopted from the experimental data by Adams and Davis discussed above and used to correct the field data for thermal decay.

Figure 11 shows the tracer return curves for field data together with the smoothed data and data corrected for thermal decay at 210°C and 220°C. The first order rate constant decay parameter used for correcting the field data, *k*, is 2.63328E-08 s^{-1} at 210°C and 5.43E-08 s^{-1} at 220°C.

5.4.3 Single fracture model tracer inverse modelling with TRINV

Single fracture model representing a 1-D flow channel whose governing equation was discussed in chapter 3.32 was applied to estimate the flow channel parameters. Inverse modelling program TRINV was used (Arason and Bjornsson, 1994). The program simulates the data through inversion. Input to the program are comprised of the estimated length of a flow channel between injection and production wells. A group of initial model parameters to be inverted for are selected and an initial guess is provided for the parameters. The program uses non-linear least squares fitting to simulate the data and obtain the model properties, i.e. the flow channel volume *(Axφ)*, the longitudinal dispersivity *(αL)* among other parameters (Axelsson at al., 2005).

Some of the assumptions made in the analysis are that; the flow channel connecting the injector and producer well is of a constant cross-section area, flow is one-dimensional, production and injection rates are constant, molecular diffusion is neglected, no phase changes take place in the flow channel, mass of the tracer is conserved hence thermal degradation and chemical reaction with the reservoir fluids and rocks have to be corrected for before modelling, fluid density inside the flow channel is constant.

The estimated parameters of the interconnecting flow channels and the tracer mass recovered as simulated with TRINV program are summarized in Table 4. The results of tracer inversion plots are shown in Figure 12. Only one flow channel was used for simulation of each well pair. Not all tracer injected can be recovered since as had been discussed some of the tracer is adsorbed in the reservoir rock matrix, others travels and diffuses through other parts of the reservoir outside the main flow-paths and some of the tracer undergoes thermal degradation. In the analysis of the tracer recovery curves described before, matrix permeability as well as high tracer dispersion is indicated by wide tracer pulses while fracture permeability is related to sharp and narrow pulses.

Table 4 below shows the single fracture model parameters used in the inversion of fluorescein break through curves. Product *Aφ* is the flow channel effective cross-section area, *αL* is longitudinal dispersion, *u* is the mean fluid velocity and *Mr* is the mass ratio of mass recovered to the injected mass of tracer.

TABLE 4: Model parameters used to simulate Fluorescein for the production wells
OW 15, 18 and 19 and injection well OW-12 (injection rate 27.8 kg/s)

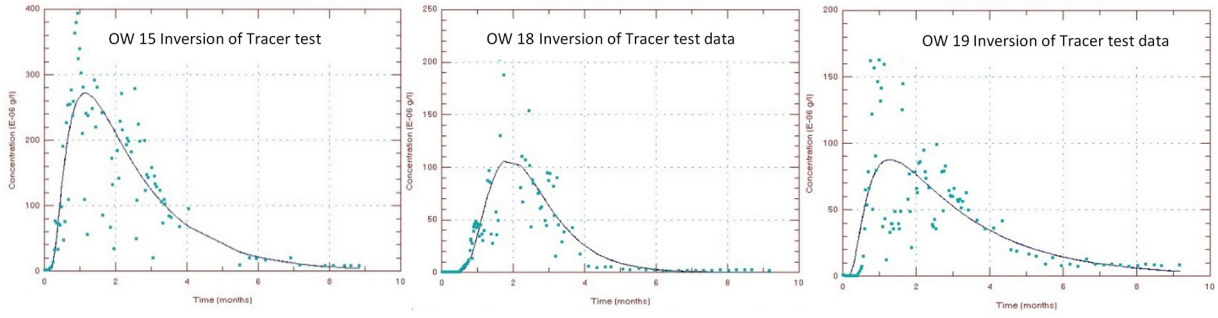| Well	% Coeff	*Aφ* (m$^{2)}$)	*αL* (m)	*u* (m/s)	*Mr* %	*Cmax* (kg/m^3)	Pulse width
OW 15	67.0	14.10	65.74	5.354E-05	2.60	2.718E-04	34 days
OW 18	72.2	5.14	28.12	5.112E-05	0.98	1.077E-04	57 days
OW 19	50.6	3.05	161.72	9.370E-05	0.98	8.770E-05	40 days

FIGURE 12: Observed (boxes) and simulated (line) tracer recovery in wells OW 15 (left),
OW 18 (centre) and OW 19 (right)

5.4.4 Cooling predictions for single fracture model

The results of single fracture model inversion, volume and mass ratio are used with additional information on the flow path geometry and rock properties are used to predict cooling in the flow channel connecting the wells. The objective is to predict thermal breakthrough and temperature decline during the long-term injection. The tracer recovered in the three well throughout the monitoring period is ~5%. A small fraction of the injected water is recovered through each of the three wells and thus the predicted temperature declines are not very great.

An example of analytical solution for temperature changes in a flow channel along a fracture or horizontal interbed which considers coupling between heat advected along the flow channel and heat conducted from reservoir rock to the fluid in the channel is presented in Equation 5.3 (Axelsson et al., 2005).

$$T(t) = T_0 - \frac{q}{Q}(T_0 - T_i)\left\{1 - erf\left\{\frac{kxh}{c_w q\sqrt{\kappa(t - x/\beta)}}\right\}\right\}$$

$$\beta = \frac{qc_w}{\langle \rho c\rangle_f hb}$$

$$\langle \rho c\rangle_f = \rho_w c_w \varphi + \rho_r c_r (1 - \varphi)$$

(5.3)

Here $T(t)$ is the production fluid temperature, T_0 undisturbed reservoir temperature, T_i injection temperature, Q rate of fluid production, q fluid injection rate, *erf* error function, k thermal conductivity of the reservoir rock , κ rock thermal diffusivity, x the distance between injection and production wells, $\langle \rho c\rangle_f$ is the volumetric heat capacity of the flow channel, ρ density, c heat capacity with subscripts w and r standing for water and rock respectively.

To address the uncertainty in cooling predictions based on tracer test data alone, the predictions are calculated for two different assumptions on flow channel dimensions and properties. A high porosity small surface area pipe-like flow channels considered as a pessimistic case resulting in rapid cooling prediction as seen in Figure 13 (left) and a second case where low porosity and large surface area, i.e. great height to width aspect ratio, was considered as the most optimistic case resulting in slow cooling prediction.

The results of cooling prediction are presented in Figure 13. The software TRCOOL (part of ICEBOX program package), which solves for temperature in Equation 5-3, was used to predict cooling during long term injection. The pessimistic model predicts well OW-15 to cool by more than 20°C and wells OW-18 and O-W19 to cool by about 6°C for a forecast period of 15 years (Figure 13 left). Optimistic model predicts OW-15 to cool by 16°C, OW-18 to cool by 2°C and OW-19 to cool by 4°C for the same period (Figure 13 right).
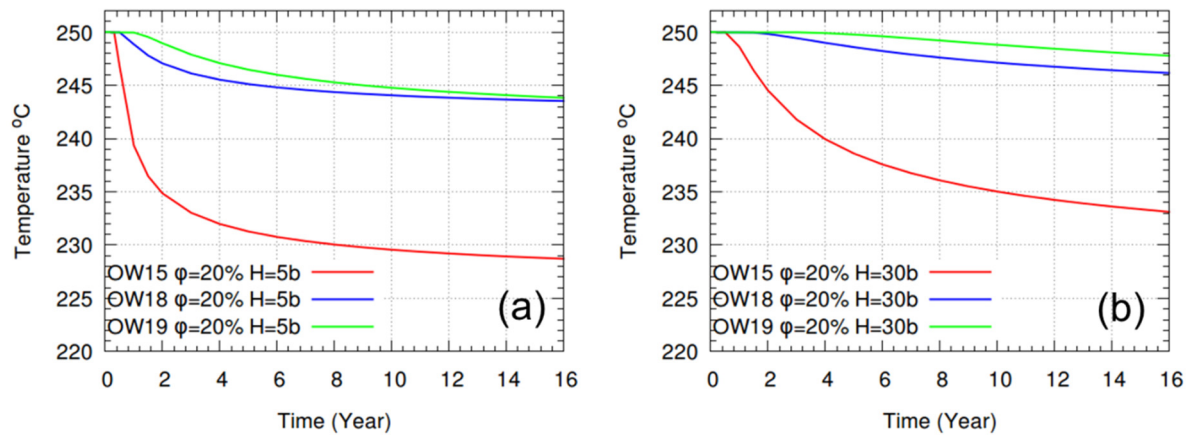
FIGURE 13: Cooling predictions calculated for wells OW-15, OW-18 and OW-19 during reinjection
into well OW-12 for small surface area high porosity flow channel (a)
and large surface area low porosity flow channel (b)

5.5 Numerical reservoir model

Numerical reservoir model is developed for the area covering the Eastern and South east part of the field. It will be used to test the effects of long term reinjection for different mass and temperature scenarios. These will be compared to the prediction earlier performed with the single fracture model. The TOUGH2/iTOUGH2 code is used to model the geothermal reservoir. Model development is split into four stages:

1. First stage involves development of natural state model of the field prior to exploitation, corresponding to the year 1981.
2. Second stage involves production history matching, where the production well mass flows and enthalpies, reinjection well mass injected and enthalpy, and the monitoring well pressure time series are simulated.
3. In the third stage the reservoir model is further calibrated on the tracer data to characterize better the fractures
4. The last stage involves forecasting the field response to long term reinjection. Different mass flows and temperature scenarios are tested.

To simulate tracer transport TOUGH2 code provides two waters option while using equation of state 1 (EOS1) where geothermal fluid is assumed to be pure water. All water properties were obtained from equation-of-state module EOS1 which contains steam table equations as given by the International Formulation Committee (1967). By default water 1 is COMPONENT 1, and the tracer contaminated water is defined as water 2, i.e. COMPONENT 2. The TOUGH2 code preserves mass of waters 1 and 2, and computes these two mass fractions for each model element at all times.

The model extent in respect to the Greater Olkaria Geothermal Field is as highlighted in Figure 14. The model covers Olkaria East field where usable tracer injection tests are available and extends to the southeast field.

5.5.1 Conceptual model

Conceptual models are primarily based on geological and geophysical information, temperature and pressure data as well as information on the chemical content of reservoir fluids. Conceptual models should explain the heat source for the reservoir in question and the location of recharge zones, as well as describe the location of main flow channels and the general flow pattern within the system, in addition to reflecting the size of the reservoir involved. Conceptual models are ultimately the foundation for all geothermal resource assessments, particularly geothermal reservoir modelling. In addition conceptual models are an important basis of field development plans, i.e. selecting locations and targets of wells to be drilled and field appraisal.
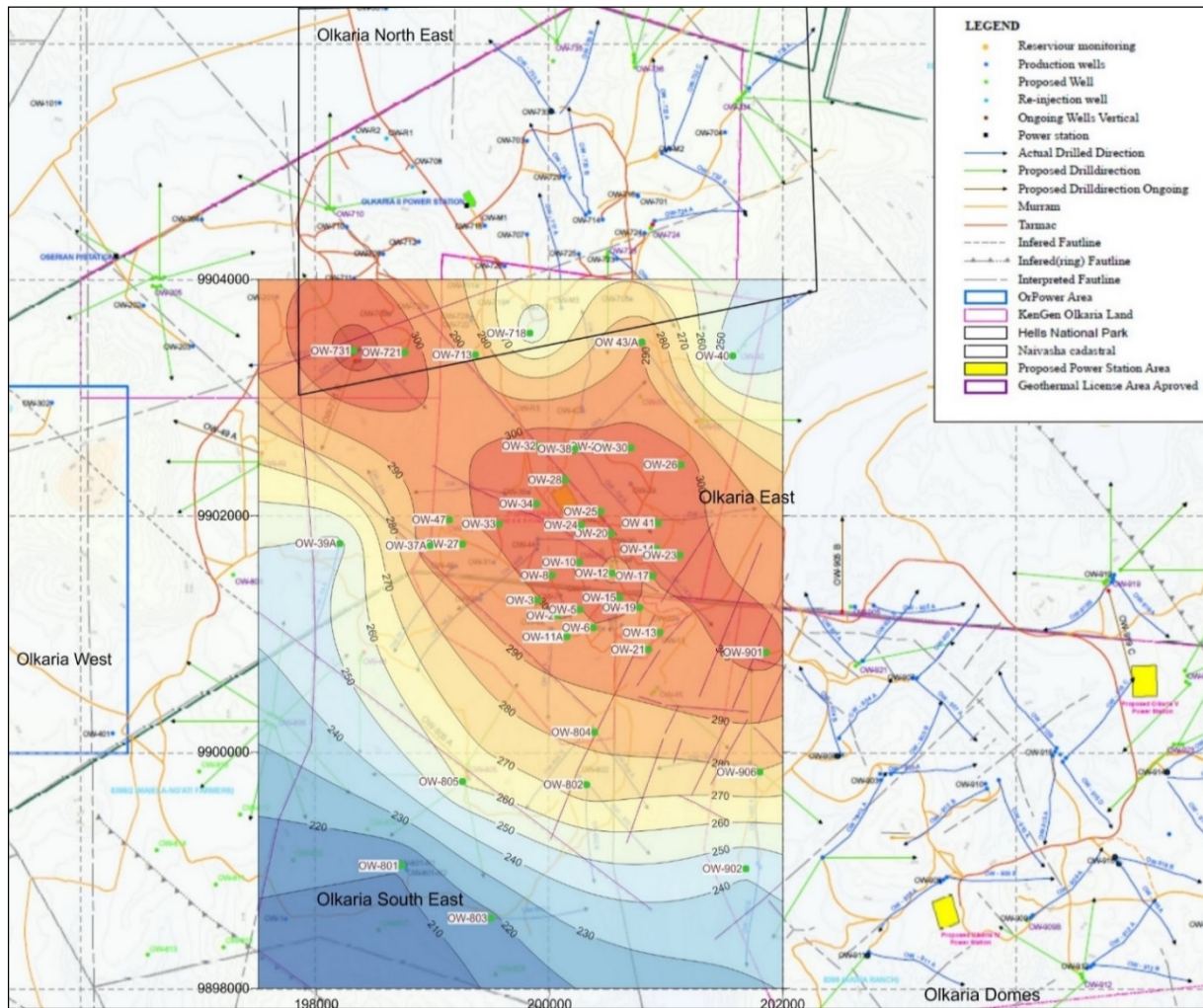
FIGURE 14. Model extent as highlighted with temperature contours at
500 m a.s.l. in the Greater Olkaria Geothermal Field

The conceptual model of the Olkaria geothermal resources has been constantly developing since 1976 when the first conceptual model was developed (Sweco and Virkir, 1976). The latest version of the conceptual and numerical reservoir models were developed by Mannvit/ISOR/Vatnaskil/Verkis consortium (Axelsson et al., 2013a and 2013b) It involved extensive review of previous models and incorporates the most recent data. The main elements of the conceptual model are discussed next.

The heat source of the Greater Olkaria Geothermal System is assumed to be a deep-lying magma chamber. The available seismic data, shown in Figure 16, indicates that three main intrusions shoot up from the magma chamber to shallower depths of 6 – 8 km. The figure indicates that the main heat source bodies (possibly partially molten) lie beneath the Olkaria Hill (supplying the West field), in the northeast beneath the Gorge farm volcanic centre (supplying the Northeast field), and in the Domes area.

The major geothermal up-flow zones are identified from the temperature model shown in Figure 16 showing the assumed heat source bodies superimposed with temperature contours. An up-flow zone feeding the West field seems to be associated with the heat source body beneath Olkaria Hill. Two up-flow zones, one feeding the Northeast production field and another feeding the East production field and the northwest corner of the Domes are probably both associated with the magmatic body beneath the Gorge Farm volcanic centre. The up-flow zone beneath the Eastern field is supported by the clear high-temperature anomaly in the area as well as by the chemical characteristics of the fluids discharged by wells, which are distinct from those of the Northeast and Domes fields. Finally, one up-flow zone appears to exist beneath the ring structure in the southeast corner of the Domes field, related to the magmatic body evident beneath the Domes area

The highest Cl concentration and Na/K temperatures are found in the discharge of wells in the centre of the Northeast and East production fields and in the southeast part of the Domes. This signifies an up-flow of deep, hot and Cl rich water, supporting the location of up-flows in these areas.

Permeability in the system is fracture-dominated, which is evident from the high well-to-well variability in the depth to high-temperature alteration. Flow paths are controlled by predominantly N-S, NW-SE and NE-SW trending faults, as shown in Figure 15 and Figure 16 displaying the main structural characteristics of the model along with the conceptualized recharge paths and upflow areas. Both figures show the main faults in the system along with the ring structures encircling the Domes field, representing a possible inner and outer rim of the proposed Olkaria caldera. Both the inner and the outer ring structures connect to the Gorge Farm fault, located north and east of the main production area. Figure 17 shows the geological structure of the field with the postulated heat sources.
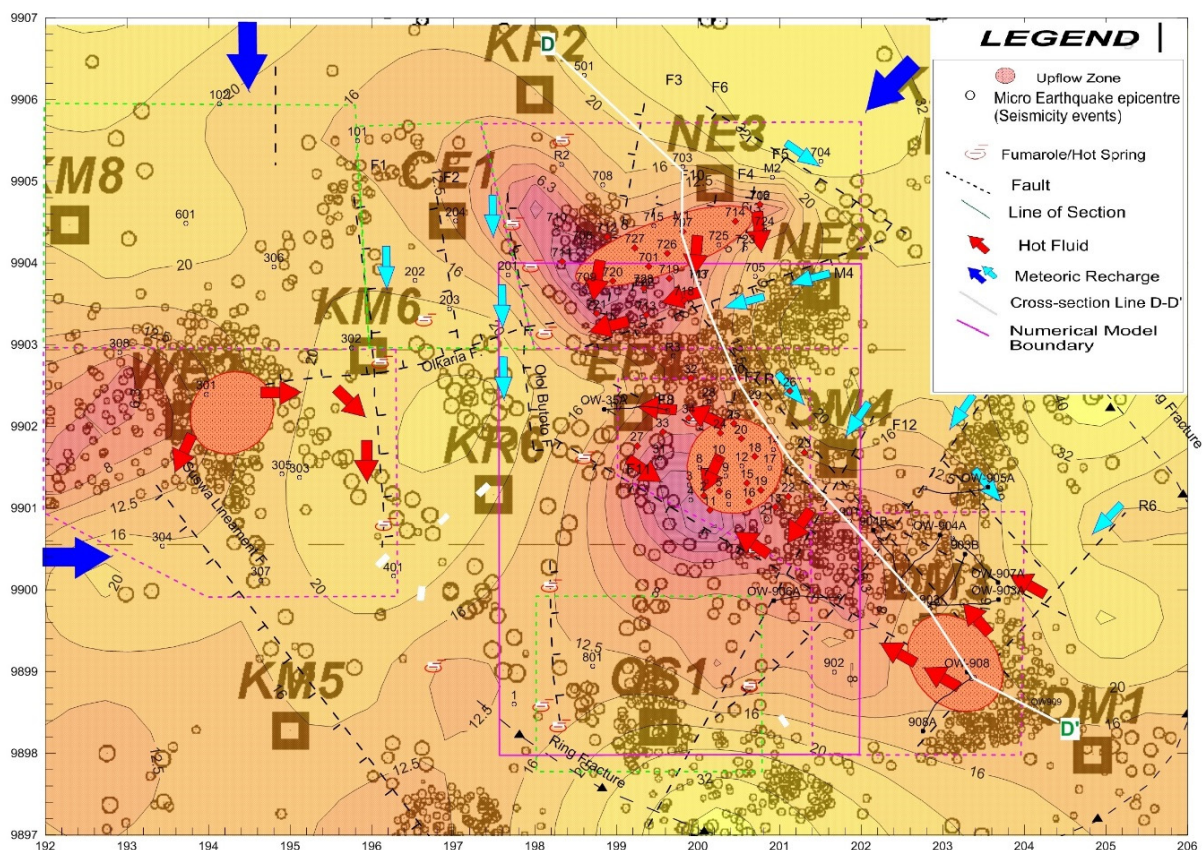

FIGURE 15: Geophysical TEM-data contours at 400 m a.s.l. and micro earthquake epicentres along with the conceptualized recharge paths and upflow areas Modified from Mannvit/ISOR/Vatnaskil/Verkis (Axelsson et al., 2013a, and b)

Cold water is assumed to flow into the system through the N-S fault system along the Ololbutot fault, shown in Figure 15, and possibly into the Domes area from the northeast. This can be deduced from the low enthalpy areas between the Western field and the Eastern production field and between the Eastern field and the Domes field. The Ololbutot fault zone is also believed to present a hydrological barrier in the system that separates the eastern and the western parts of the geothermal system.

Recharge to the system appears to be of two types. Deep recharge from surrounding areas and shallower cold recharge through fault systems, most notably the Ololbutot fracture zone and the Gorge Farm fault. Generally, the origin of Olkaria fluids appears to be 50% or more as deep Rift Valley water, with some variability between sectors.
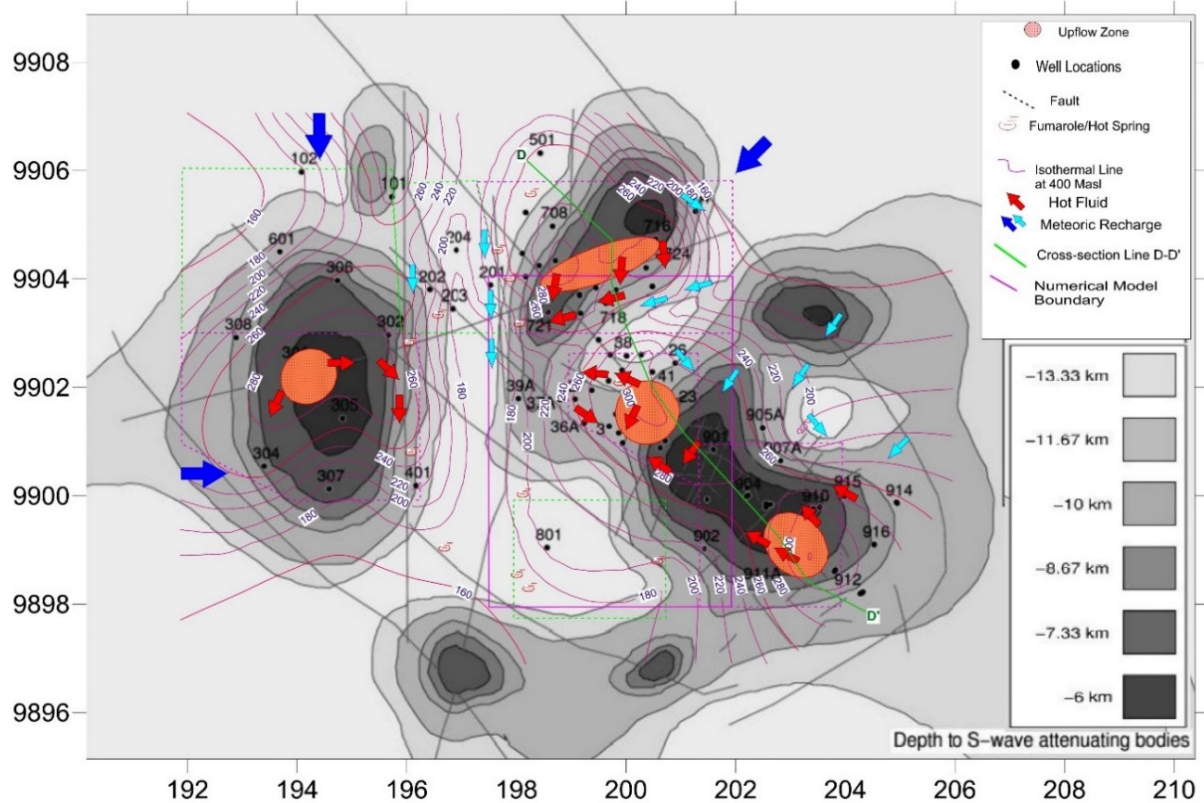
FIGURE 16: Depth to the heat source bodies with temperature contours along with the conceptualized recharge paths and upflow areas - modified from Mannvit/ISOR/ Vatnaskil/Verkis (Axelsson et al., 2013a and 2013b)
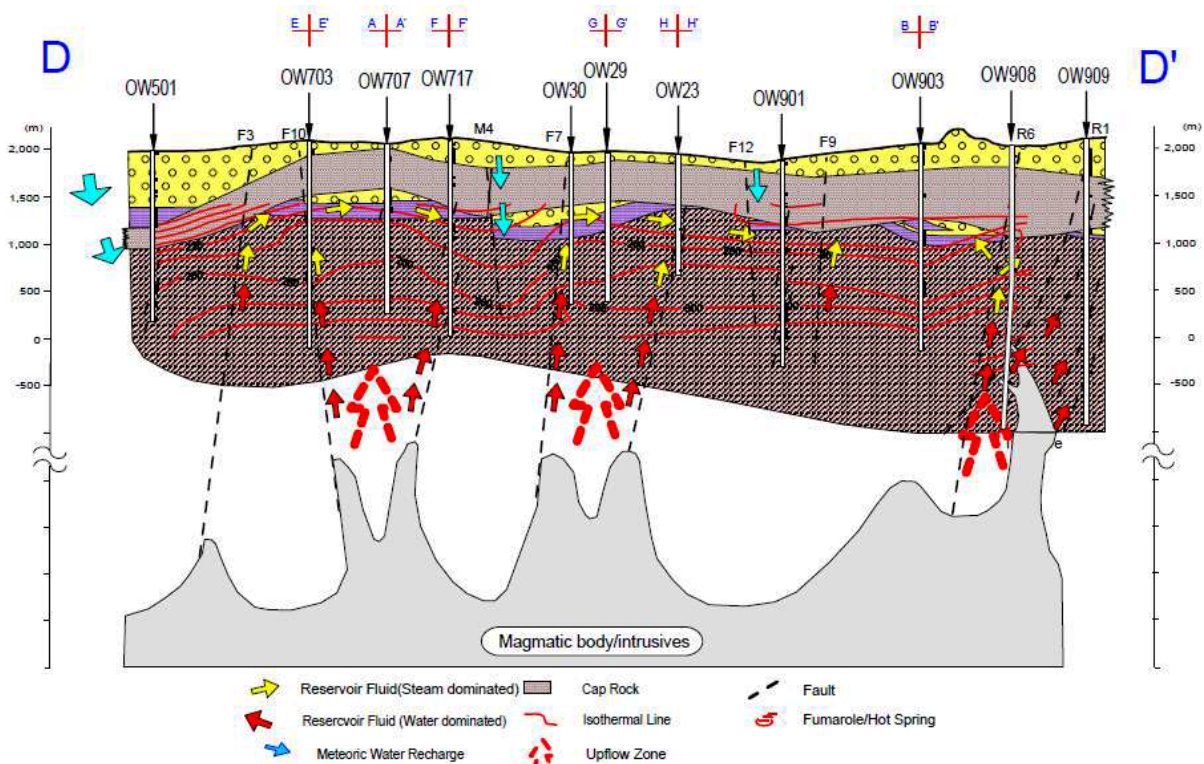

FIGURE 17: The three main intrusions and geological structural characteristic of the field - modified from Mannvit/ISOR/ Vatnaskil/ Verkis (Axelsson et al., 2013a and 2013b)

29

5.5.2 Numerical model

Numerical simulation of geothermal reservoirs is a very useful instrument for making decisions about the strategies of field exploitation and to analyse the behaviour of the whole rock-fluid-power plant system. Numerical model construction must be supported by a detailed knowledge of the spatial distribution of the properties of the reservoir in the form of conceptual model. The accuracy in the collection of the data is fundamental for the construction of an efficient conceptual and numerical model.

The approach taken is as outlined by Pruess (2002a and b), where continuous space and time variables are discretized. The volume of the reservoir system referred to as space is partitioned into sub volume grid elements. Hydrological and thermal properties are then assigned to the elements or a group of elements as guided by the conceptual model. Boundary conditions are chosen appropriately and sinks and sources are assigned to some selected elements to simulate wells and inflows respectively. Simulations for natural inflow and outflow as well as production wells and reinjection wells are finally done with finite element methods to solve relevant equations for conservation and flow of heat and mass.

5.5.3 General mesh features

The mesh is set up using RockEditor (developed by Vatnaskil) software package whose code is based on the Amesh code. The code generates discrete grids compatible with the TOUGH2 code which solves numerical modelling of flow and transport problems formulated on integral finite difference method (Haukwa, 1998).

The model mesh covers 27 km^2 and a thickness of about 3200 m, ranging between 1850 m a.s.l. to -1400 m b.s.l. The mesh consists of 9016 elements, where 1288 elements are inactive, and 34580 connections. The mesh grid boundary conditions are set as guided by the temperature and pressure observed in the wells at/close to the model boundary. As this model does not span the entire field there is bound to be expected influence from the edges of the model. From the conceptual model the main recharge to the system is from the northern boundary (Figure 18). The outermost elements of the grid are slightly larger and have the same rock type with very low permeability to keep stable temperature and pressure at the boundary. The top and bottom layers are also set inactive and relatively impermeable. These boundary conditions constrain the model thus maintaining a constant temperature and pressure in the top and bottom layers while limiting fluid flow into or from adjacent layers (Figure 18). The model consists of 14 layers of various thicknesses but the horizontal mesh remains the same for each layer. Figure 19 shows the vertical view of the mesh with the layers named in alphabetical order. Layer A represents the top and layer N represents the bedrock the two layers are set inactive. Layers B and C represent the caprock as is exhibited by the conductive temperature gradient in the measured data plots. Layers D to M constitute the high temperature reservoir. The wells have varied depths and feed points as listed in Appendix C, which were used to set the model layers.

5.5.4 Rock properties

Different rock types have been assigned to different regions in the model. An assumption is made that all the elements have the same physical properties such as density, porosity, thermal conductivity and specific heat capacity but with different permeability. The assumed physical properties of the rocks in the Olkaria Field are; density 2650 kg/m^3, porosity10%, specific heat capacity 850 kJ/(kg.K) and thermal conductivity 2.1 W/(m°C).

Figure 18 shows the rock type assignment for the reservoir zone layers D to L. Appendix J shows permeabilities assigned to the rocks.
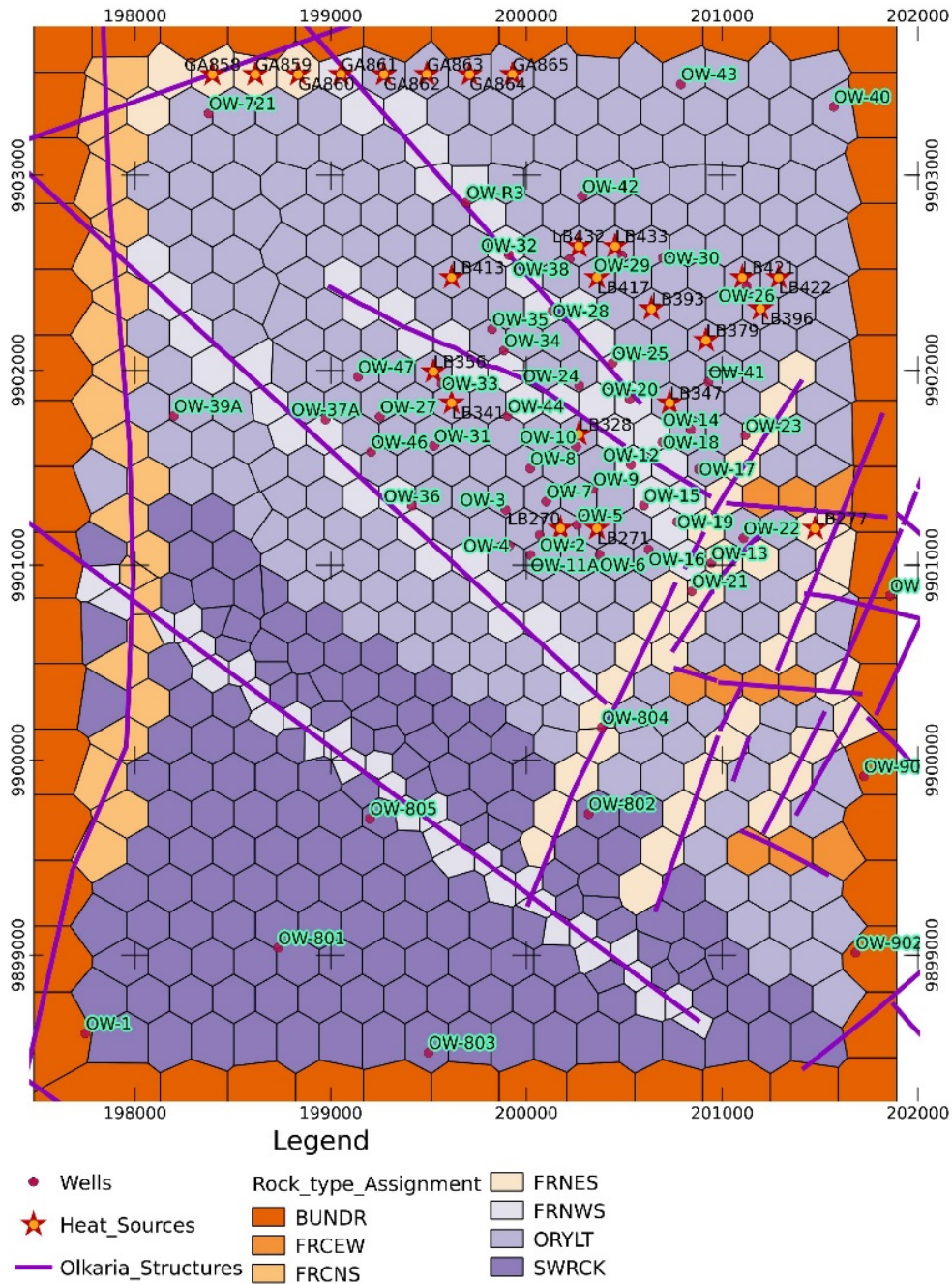
FIGURE 18: The numerical model grid layout and model rock type assignment, locations of wells and heat of sources in layer M are shown as yellow and red stars. Main fractures/structures also indicated

5.5.5 Initial conditions

The fluid in the numerical model is assumed to be pure water. All water properties into the model simulations are thus obtained from equation-of-state module EOS1 in TOUGH2. The flow systems in the model are initialised by assigning a complete set of primary thermodynamic variables to all grid blocks into which the flow domain is discretized (Pruess et al., 1999).

A temperature gradient of 85 °C/km and initial pressure of 2 bars at 1850 m a.s.l., i.e. the topmost layer A, are used as inputs to the RockEditor, which computes the temperature for all elements. The temperature and pressure for layers at the bottom varies in a wide range; they were manually changed for the inactive layers as guided by the conceptual model. Elements in areas corresponding to the upflow are expected to have higher temperature.
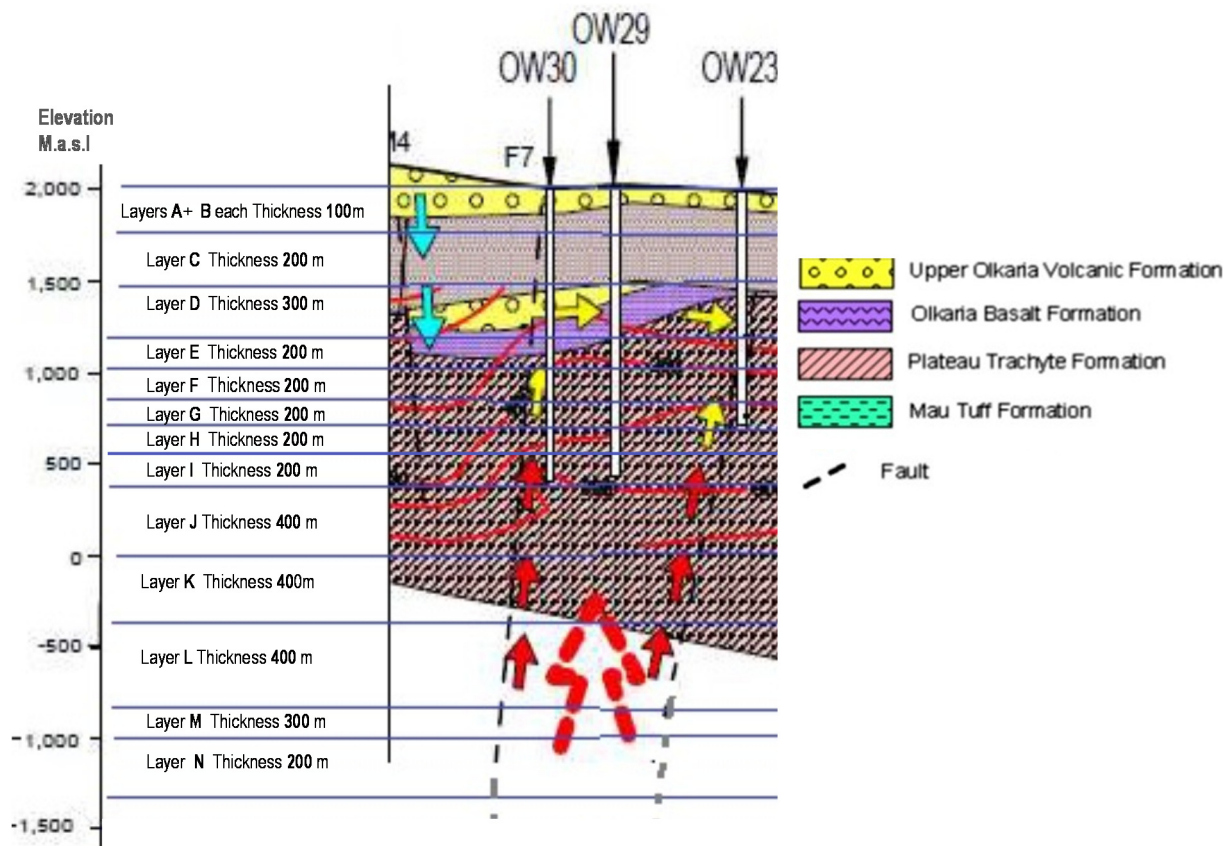
FIGURE 19: The numerical model grid vertical view, layer thickness and reservoir stratigraphy

Pruess (2002a and b) states that it is important to specify the model domain large enough so that the simulated behaviour is not unduly influenced by artificial boundary conditions close to the well field. It is for this reason that the model boundary in the east extends up to the edge of the Domes sector with the boundary conditions set based on wells OW-901, 902, and 906. The Olkaria fracture and wells OW-713, 718, 721, 731 and 43 are used to specify the initial conditions in the north. The Ololbutot fault is used as the boundary to the west.

Bodvarsson and Pruess (1987) in their Olkaria model-study used an observed north-south pressure gradient of 11 bars/km for the Olkaria east field that had been drilled then. The geothermal field was conceptualized to be having a steam zone with a temp of about 240°C encountered at 600-800m, the average vertical temperature gradient above the reservoir is approx. 400°C/Km. Average transmissivity of the liquid dominated reservoir is set at $3 \times 10^{-12} \, m^2 s^{-1}$. Rate of natural liquid flow through the reservoir is estimated as 50 kg/s (180 t/hr). The field extent considered was 2 km width from east to west. The Mannvit/ISOR/ Vatnaskil/Verkis consortium (Axelsson et al., 2013a and 2013b) used a north-south pressure gradient of about 30 bars for the entire field.

The correct temperature and pressure values for the active elements are generated during simulation process by adjusting the permeability and strength of heat sources while checking for the match between the measured and calculated data. The process is described in the next chapter.

6. RESULTS

6.1 Natural state model

A natural state model is a rendition of the physical state of a geothermal field in its pre-exploitation state. Primary purpose of a numerical natural state model is to verify the validity of conceptual models and to quantify the natural flow within the system (Bodvarsson et al., 1989). It consists running a model for a long time in a simulation of the development of the geothermal field over a geological time until steady state has been reached (O'Sullivan et al., 2001). At steady state, the heat and mass entering into the model are equal to heat and mass released through the boundaries and thus no change is observed in thermodynamic variables.

The model is constructed with an input of mass and heat at the bottom. Guided by the conceptual model, mass sources are set in in layer M, the bottom most active layer where the upflow is assumed to be located in the reservoir. The mass sources supply fluid of constant enthalpy with constant mass flow rate. Permeability distribution, the rate of mass and heat upflow into the system are adjusted automatically by iTOUGH2 until the residual difference between calculated and observed pressure and temperature is minimized. To achieve the best match a total of 55 kg/s of fluid with an enthalpy of around 1600 kJ/kg is injected into the model, giving a thermal input of about 88 MWt. Figure 18 shows the model heat sources with the assigned elements.

The results of the natural state simulation shows that the model simulates formation pressure and temperature quite well. Figure 20 shows the down hole pressure and temperature as calculated by the model plotted as a function of the measured/estimated formation pressure and temperature. For a perfect fit all the point should line up along the straight line. There is systematic misfit in the cap rock and slightly in the steam cap. Well by well plots are presented in the Appendix C.
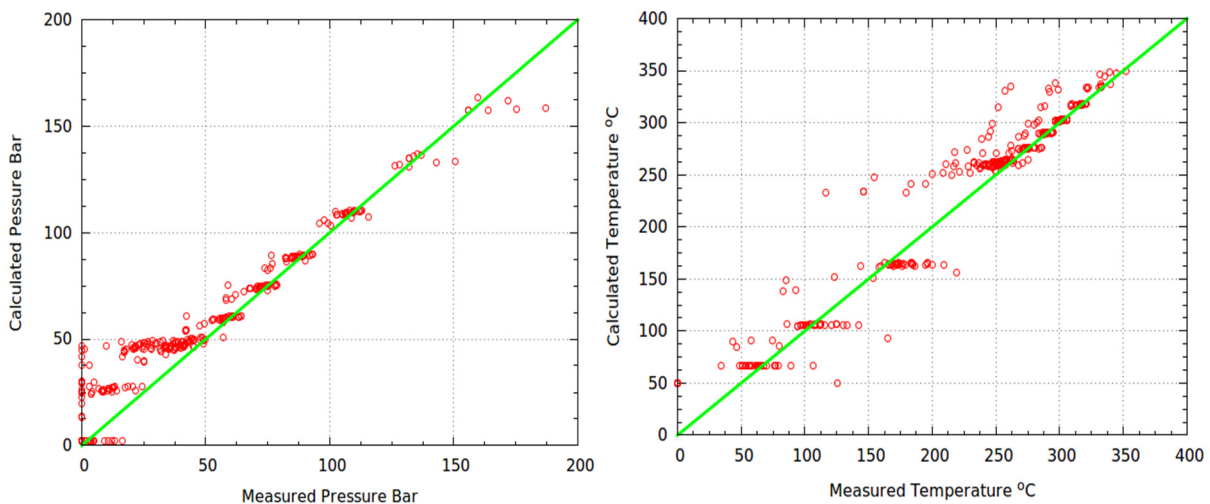

FIGURE 20: Comparison between observed and model simulated
downhole pressure (left) and temperature (right)

Figures 21 and 22 show the comparison of the observed and simulated contours at 200 m a.s.l and -600 m a.s.l., respectively. More contours for different elevations are presented in Appendix D. Contours shows how the model captures the plume propagation from bottom to the top. Mass flow vectors extracted from the model at natural state are shown in Figure 23. The vectors shows the prevailing flow field in the reservoir domain in the pre-exploitation state. The dominant heat transfer process is convection and the resulting heat flow vectors demonstrate such a flow field.

The numerical code used (TOUGH2) outputs information on the calculated heat and mass transfer between adjoining grid blocks surfaces for each time step. Usually, in a complex model like in the current model, there are many interfaces, and a visualization of all vectors of each interface can be
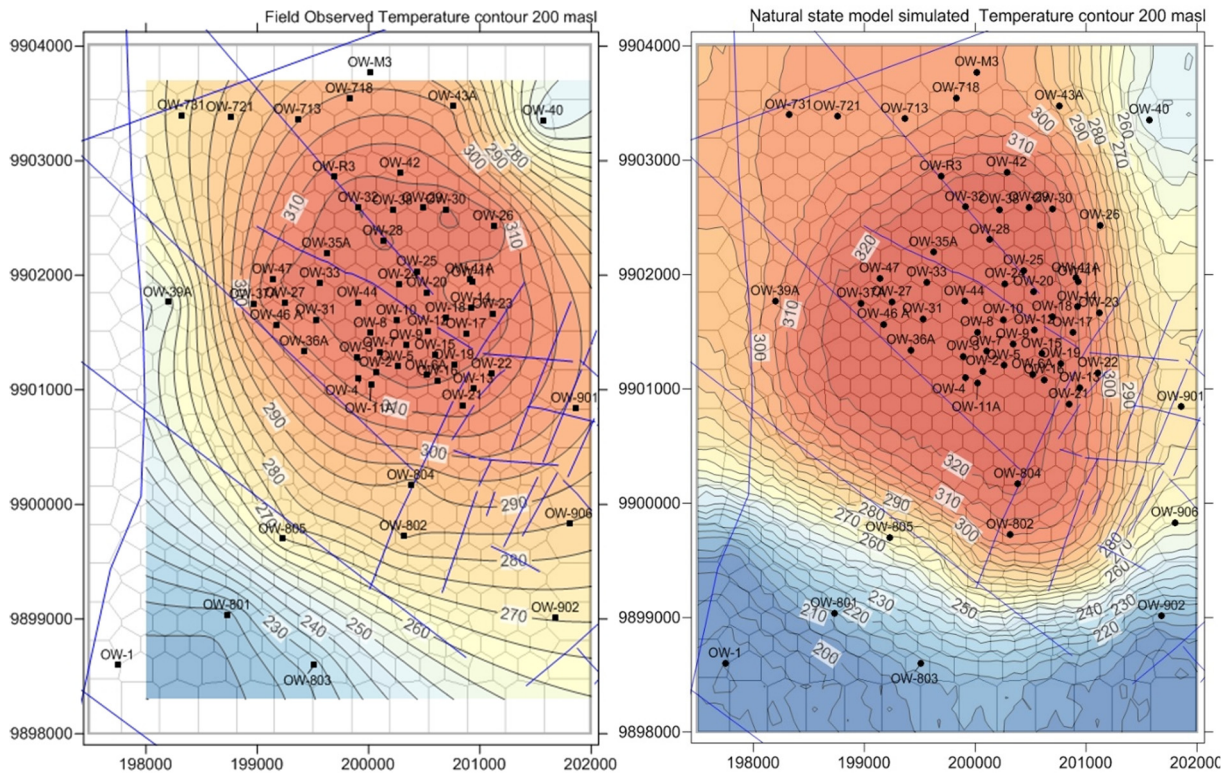
33

FIGURE 21: Comparison between observed (left) and model calculated (right) temperature contours at 200 m a.s.l. (Layer I)
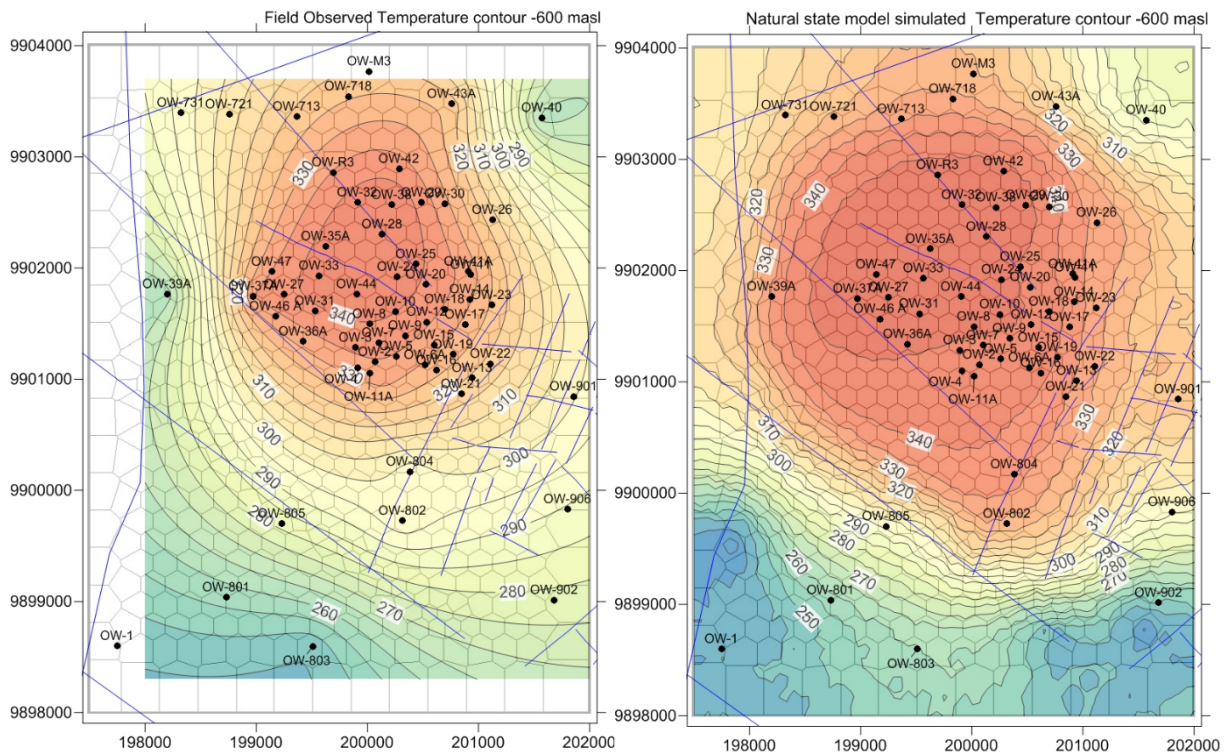

FIGURE 22: Comparison between observed (left) and model calculated (right) temperature contours at -600 m a.s.l. (Layer K)

unclear, so it was decided to associate to each grid node (computational element) the vector resulting from the sum of all flows across the interfaces of the block. The flow vector visualization gives vector flows with all vectors having unitary length and the flow rate or heat flow values are represented through a colour scale (Berry et al., 2012). Three dimensional flow vectors for the mass flow (flow field) are

shown in Figure 23. The vector flow field follows exactly the same upwelling and downflow of the total mass flow representative of a convective cell. The main heat transport mechanism is by convection. Planar view of the flow vectors in horizontal direction at 800 m a.s.l. is shown in Appendix E.1
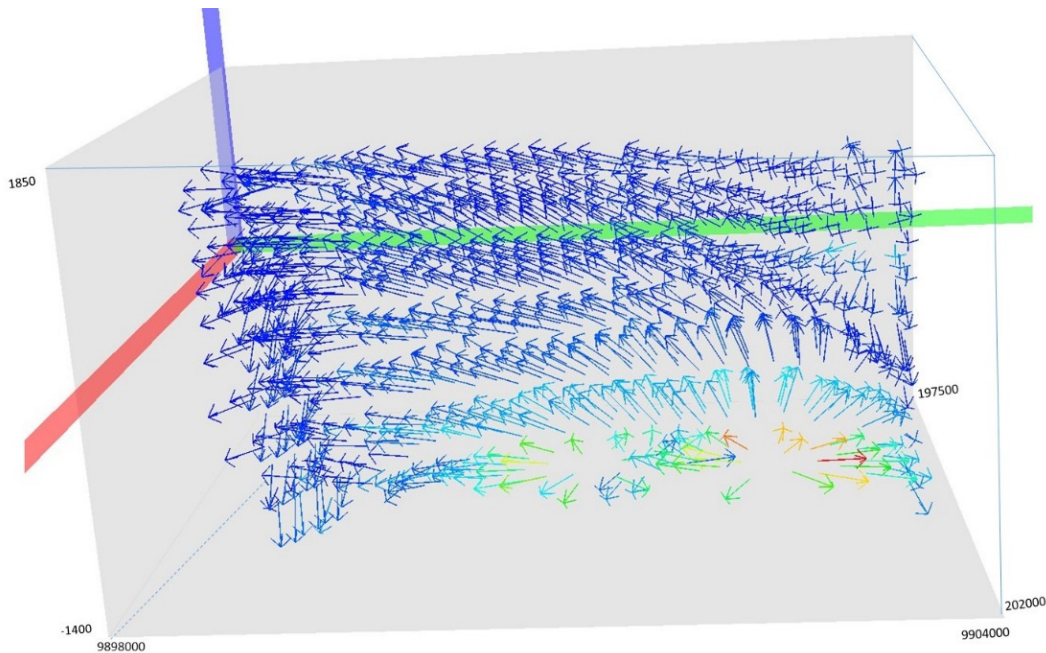

FIGURE 23: Vector flow field for the mass in the numerical natural state model of the East and Southeast sectors of the Olkaria Geothermal System

6.2 Production model calibration

The natural state model earlier developed serves as an input, or as initial conditions, for the production history model which describes the response of a reservoir to exploitation. It refines the numerical model earlier calibrated by the natural state in readiness for future production predictions. Simulation of the total production period begins by assigning the past production for given wells to relevant blocks in the model based on information about the locations of the feed-zones. The entire data set is then calibrated in a single run, that is, the system is driven to steady-state after which it proceeds automatically to the production phase. All the results are finally compared to the measured data.

The actual field response to production observed in the geothermal system comprising of mass extracted and its enthalpy together with pressure measurements are used to calibrate the production model. Producing wells are defined as mass sinks (MASS option in the TOUGH2 code) in the model where mass extracted is specified as a function of time. For wells with multiple feed zones, the relative mass extraction is assigned to the elements along the well trajectory. Details of the layers and element assignment for each producing well are as tabulated in Appendix H.

The pressure drawdown data is available for five wells, some of which have been producing and as a result have limited time series data. Pressure drawdown from the wells that once served as producing wells are unreliable as the draw-down noted could be localized as result of production and may not be representative of the reservoir. Down-hole pressure logs are used to estimate the pressure variation with time. Capacity expansion has been gradual and the total mas produced was increased in 1996 just when the pressure draw-down in the field was beginning to stabilize (Figure 24). This production increase consequently lead to an increase in pressure decline.

Pressure drawdown plots in Figure 24 show a comparison of the modelled and observed pressure available for wells OW-03, OW-08, OW-21 and OW-33 at 600 m a.s.l. The model underestimates the observed pressure drawdown but captures the general decline trend associated with increasing production.
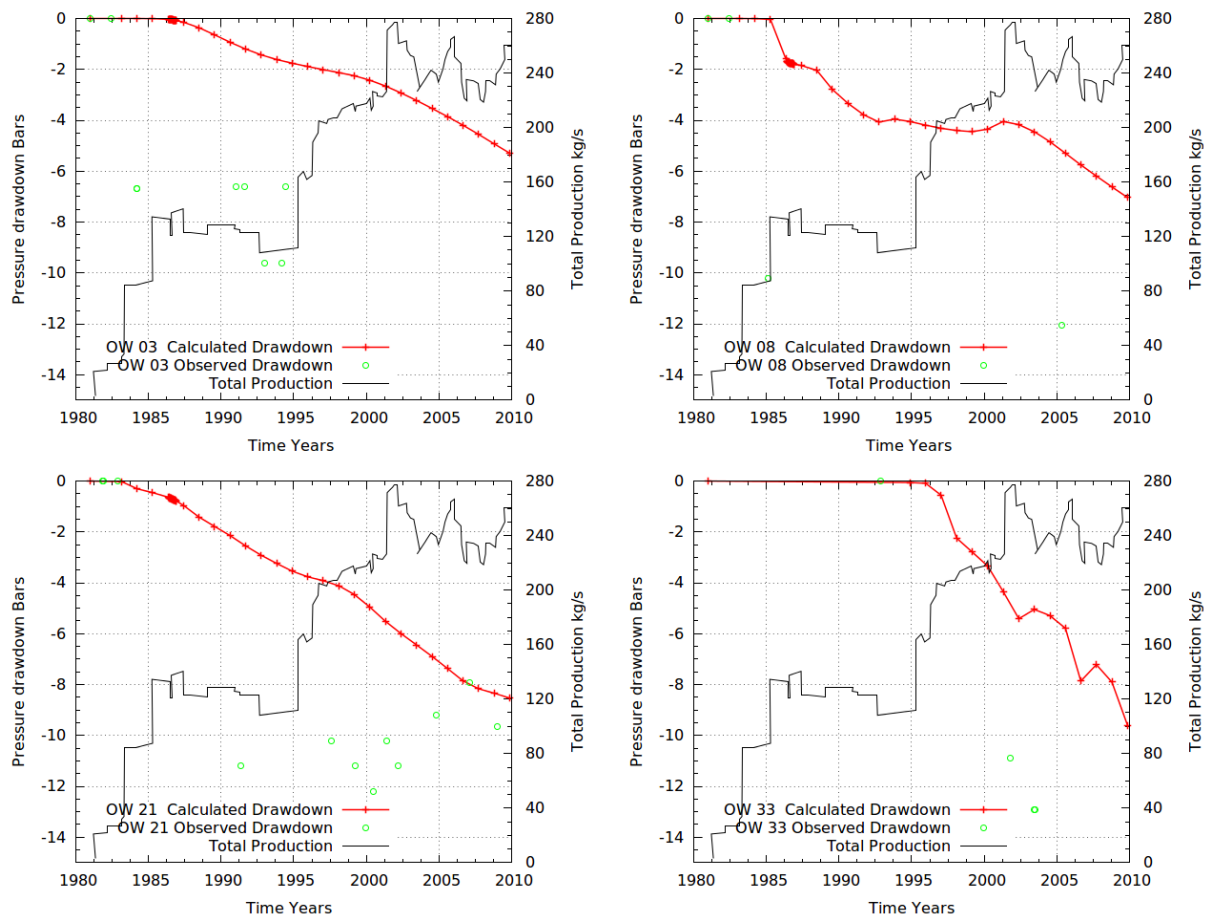
FIGURE 24: Pressure drawdown in the monitoring wells observed (green circles) and model calculated (red) in response to increased production (black)

The enthalpy of flowing wells, observed at the well head, was also used to calibrate the production model. There is a fairly good match seen for some wells and under-estimation for others but the general trend is captured. It should be noted that the enthalpy is measured from the well head and is the aggregate for all the feed zones. Simulated enthalpy is the weighted enthalpy for the feed zones assigned for each well in the model. As such getting a perfect match is a challenge considering that the precise mass flow for each feed zone has to be quantified and assigned accordingly. Field monitoring data is collected twice a year for the accessible wells and for non-monitored wells observations from previous years are extrapolated, which can explain the discrepancies in some points.

Some wells have time varying cyclic production especially when there are multiple feed zones and enthalpy difference is significant. Monitoring data is a spot reading averaged for a short period. The reservoir system under study is two-phase and a small change in steam fraction brings about big changes in enthalpy. There was also drilling of makeup wells in the field during the course of production. The drilling fluid injection rates and location of drilled wells are not accounted for. The enthalpy drop during reinjection in 1996 in OW 12 is noted in OW-15 and slightly in OW-18. Comparison between observed and model calculated enthalpy for wells OW-11, 15, 18 and 21 are shown in Figure 25, plots for other wells are presented in Appendix I.

6.3 Tracer test data application in model calibration

In this chapter an attempt is made to incorporate the tracer test data discussed above into the production model after it has been calibrated against available field production history observations. The tracer is introduced as a pulse into an element corresponding to well OW-12 in the calibrated production model. Figure 26 shows the breakthrough curves simulated by the model. Simulated tracer recovery shows that the tracer peaks arrive after about 3-6 years, much slower than in reality.
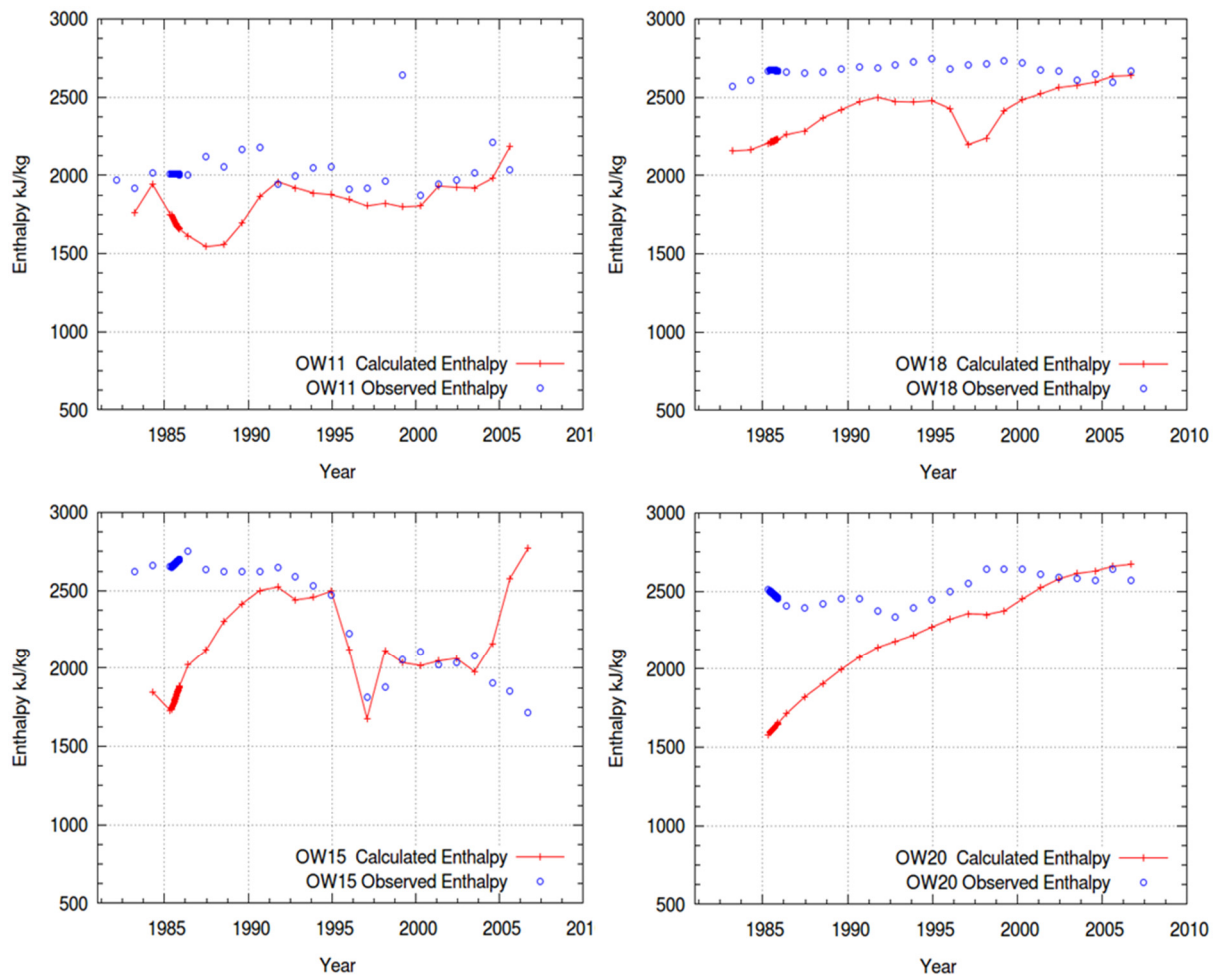
FIGURE 25: Comparison between observed enthalpy at the well head (blue)
and the simulated enthalpy (red).

To try and improve the tracer break through speed an explicit fracture was defined as shown in Figure
27. Hydraulic conductivity of the structure was increased so that the tracer could travel quickly through
the channel by advection so as to improve the match to the field observation breakthrough times. The
tracer breakthrough curves observed in the field data suggest the presence of flow channels connecting
the wells. From the interpreted geological structures the intersection of NE and NW trending fractures
could imply the presence of a fractured region (rock type defined as EPFNS with higher permeability,
see Appendix J).

It was not possible to increase the permeability to the extent of matching the field data, with the current
computational grid. Simulation deteriorated due to numerical dispersion, a phenomenon associated with
advection dominated transport. Significance of advection is determined by Peclet number. Peaceman
(1977) showed that numerical dispersion in solving of advection equation is a function of grid block
size and time step size. Liou (2007) discusses the numerical dispersion as handled in the TOUGH2 code.
It uses upstream weighting method in space and fully implicit discretization in time. Numerical
dispersion is a function of advection velocity, grid size and Courant number. The Courant number is
defined as the ratio of disturbance/tracer travel distance in a time step to the grid size. This determines
the stability of simulation. Since grid size was fixed the time step was reduced, but tracer breakthrough
curves could not be matched successfully. Multiple interacting continua (Wu and Pruess 2000) concept
was then introduced to try to enhance the resolution of spatial discretization in the flow channel.
Successful modelling of advection dominated tracer transport in fractured media requires good spatial
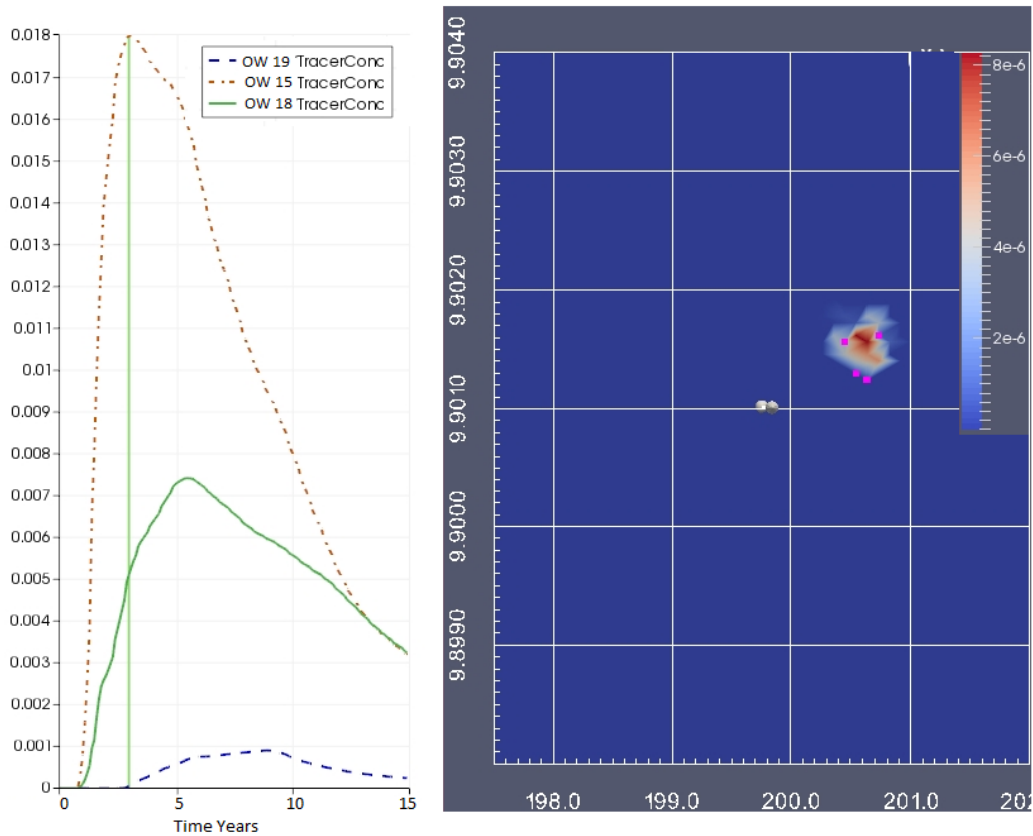and temporal discretization.

FIGURE 26: Production model calculated tracer recovery curves for wells OW-15, OW-18 and OW-19 with tracer injection in OW-12 (left) and tracer cloud in year 3 after tracer injection (right)

The Multiple Interacting Continua (MINC) model grid shown in Figure 27 was used to improve spatial discretization. The mesh has square block size with dimensions 50 m. There was an improved fit in the tracer break through curves, the time scales matches well except for offset in peak concentration arrival times in well OW-15 while overall peak concentration is underestimated. The MINC model covers an area of 1 km^2 around tracer injection well OW-12 and the boundary conditions and the prevailing flow field is not captured. This explains the misfit between the observed and calculated breakthrough curves. Figure 28 shows the fit between model simulated and field observed tracer breakthrough curves.
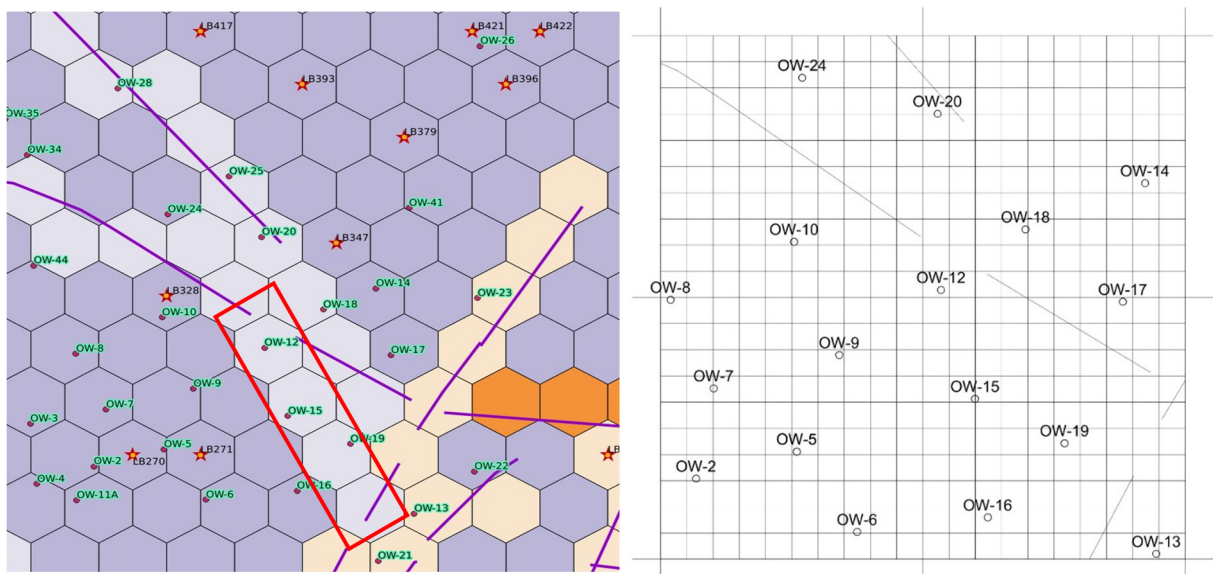

FIGURE 27: High hydraulic conductivity feature definition (left) and finer grid for multiple interacting continua (MINC) (right)
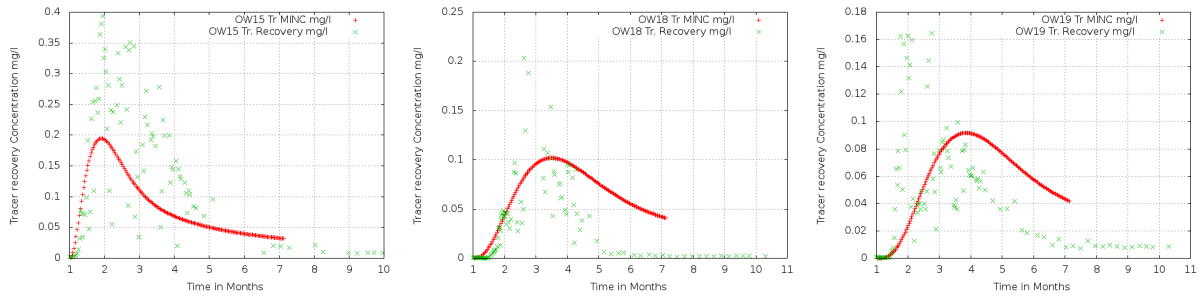
FIGURE 28: Comparison between observed (green) and MINC model calculated (red) tracer break
through curves for well OW-15 (left), OW-18 (centre) and OW-19 (right)

6.4 Cooling predictions

The reservoir response (i.e. cooling) to short-term reinjection in OW-12 was evaluated with the
numerical model. Well OW-12 is drilled to a depth of 918 m (~1000 m a.s.l.). Three injection rates 20,
30 and 50 kg/s were tested at three reinjection temperatures 25°C, 45°C and 80°C. The production rates
were maintained in the producing wells over the simulation period. Figures 6-10 to 6-12 show the
temperature, enthalpy and pressure response curves of all the three wells over a 15 year injection period.
The model covers a relatively smaller area and long term response was not attempted since the boundary
effects and interference from neighbouring fields will have to be accounted, their effect will be
significant as pressure drawdown increases with production. Well OW-15 is the most affected in all the
three scenarios, at 20 kg/s injection there is less cooling than seen at 50 kg/s. At 50 kg/s injection rate
the difference in temperature drop for reinjection temperatures 25°C and 80°C is about 30°C in
production temperature (Figure 29). After a year of reinjection enthalpy drops drastically for wells OW-
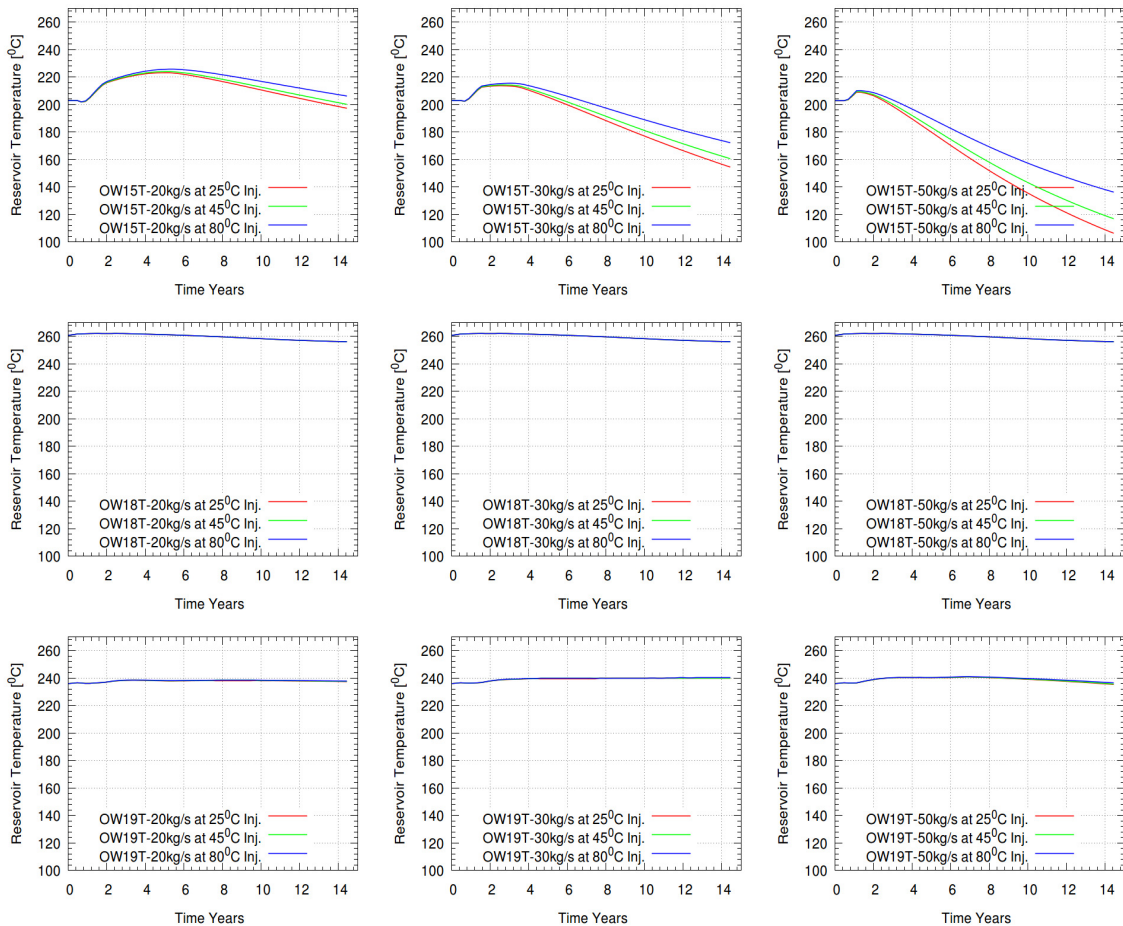

FIGURE 29: Modelled temperature response to cold reinjection in OW-12 for wells
OW-15, OW-18 and OW-19 at three injection rates and three injection temperatures
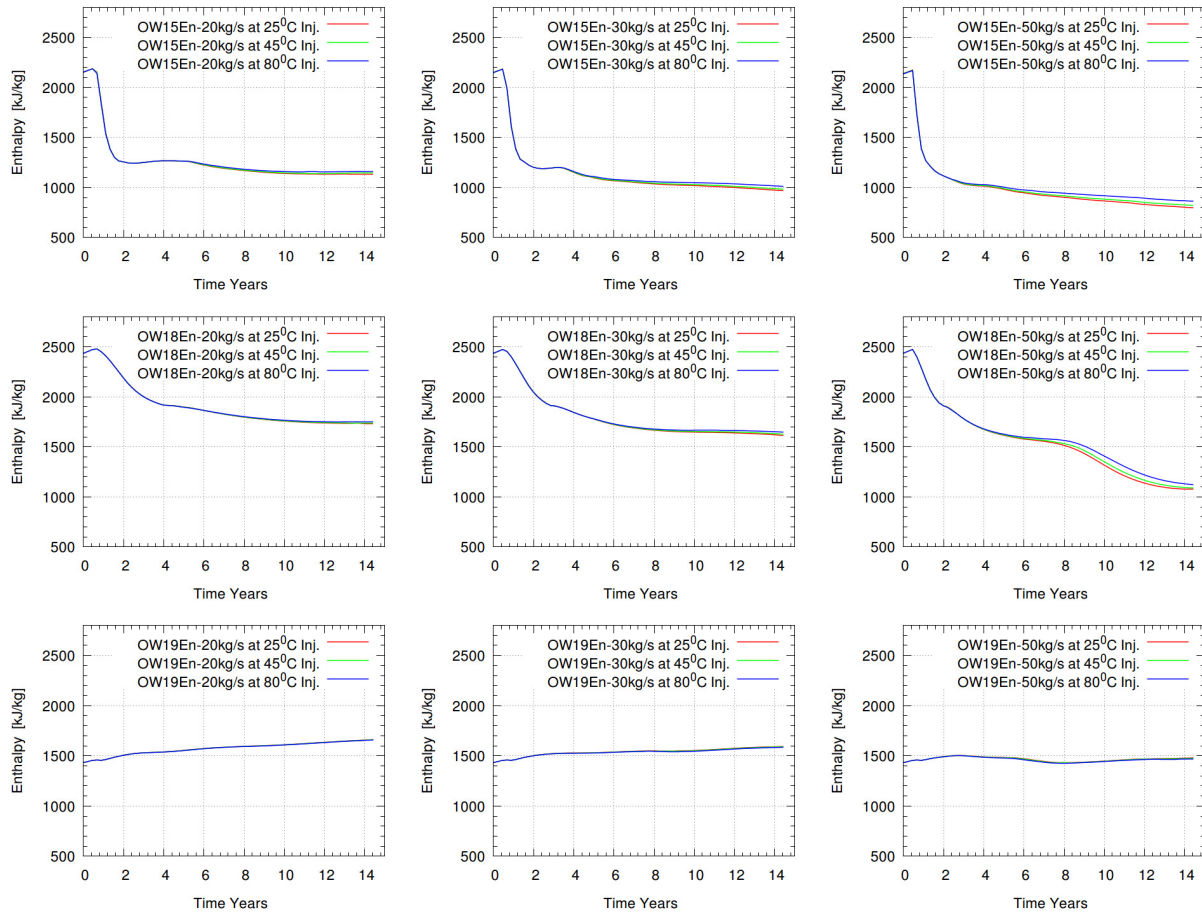
39

FIGURE 30: Modelled enthalpy response to cold reinjection in OW-12 for wells OW-15, OW-18 and OW-19 at three injection rates and three injection temperatures

15 and OW-18 the rate of decline for OW-18 is more gradual. Enthalpy of OW-19 is least affected, at 20 kg/s it is increasing and at 50 kg/s injection it stabilizes (Figure 30). Pressure increase is seen after a year in OW-15 which shows great pressure rise followed by OW-19. Greatest increase in pressure is seen in OW-15 at 50 kg/s (Figure 31). Pressure in OW-18 declines gradually with reinjection. Wells OW-15, OW-18 and OW-19 are completed at depths of 1300 m, 1400 m and 2500 m below surface, respectively. Wells OW-15 and OW-18 tap from the steam dominated zone in the shallow part of the reservoir while, OW-19 taps from the liquid dominated deeper part of the reservoir. This explains the similar characteristic enthalpy and temperature response by OW-15 and OW-18.

6.5 Comparison of deep and shallow reinjection

Deep re-injection (at -2600 m a.s.l.) was also tested to compare shallow and deep reinjection. Figure 32 shows the comparison of deep and shallow reinjection for the three production wells while injecting water at 45°C into OW-12 at 50 kg/s. OW-15 located closer to the reinjection well, for the whole reinjection period it experiences less cooling while injecting deeper as compared to shallow injection. Well OW 19 experiences more cooling. In deeper re-injection the flow path to OW-19 (deep well) is shorter and it experiences more cooling than for shallow injection. While for OW-15 the flow path is longer and less cooling is experienced. With deep reinjection the steam cap is maintained and enthalpy increases slightly. This can be countered by increasing injected mass. It should be noted that for detailed evaluation on the benefits of different reinjection schemes, it is advisable to couple well flows into the simulation. The actual production well head mass flows and parameters can be simulated and the gains with reinjection quantified in total heat extracted from the reservoir rocks for the different scenarios. In this study wells are simulated with fixed mass production assigned to the elements along the well trajectory. The net gain in heat mined by reinjecting deeper is represented by the area between deep and shallow reinjection enthalpy curves for production wells.
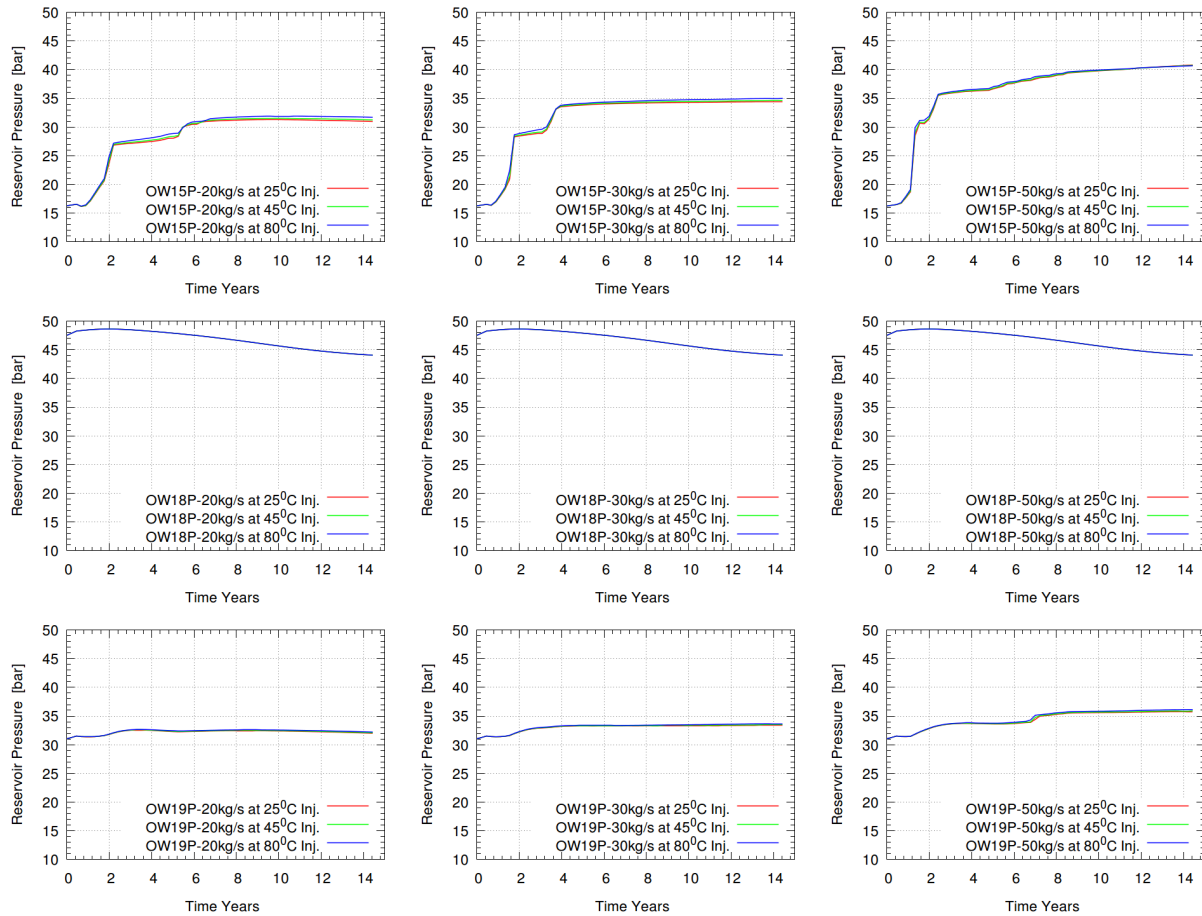
FIGURE 31: Modelled pressure response to cold reinjection in OW-12 for wells OW-15, OW-18 and
OW-19 at three injection rates and three injection temperatures

The above results are in agreement with numerical experiments by Bodvarsson et al. (1985). Injection
into two-phase fractured zones increases flow rates and decreases the enthalpies of fluids produced by
nearby wells. Injection reduces vapour saturation in the fracture system by fracture flooding and
condensation. This increases the liquid phase mobility, depending on the relative permeably used in the
simulation, and decreases the enthalpy of the fluid produced.

Colder water should be injected into the lower regions of the reservoir and production made from upper
parts. This takes advantage of variation in water density and viscosity with temperature. The denser
colder water which is more viscous will remain in lower part of the reservoir (Lippmann et al., 1977).

6.6 Comparison of cooling prediction by single fracture model and complex numerical reservoir model

Cooling is predicted in this study for a period of 15 years, using both the single fracture model (Appendix
B) and the complex numerical production reservoir model for the three re-injection wells while injecting
into well OW-12. The single fracture model showed well OW-15 to be the most affected and OW-19 is
the least affected. The pessimistic model predicts well OW-15 to cool by more than 20°C and wells
OW-18 and OW-19 to cool by about 6°C for the forecast period. Optimistic model predicts OW-15 to
cool by 16°C, OW-18 to cool by 2°C and OW-19 to cool by 4°C for the same period.

The complex three dimensional numerical reservoir model was also used to predict the reservoir
response to short-term reinjection (15 years) for a shallow injection case. Thermal front propagation was
captured in the complex reservoir model. Comparison of thermal front breakthrough for well OW-15
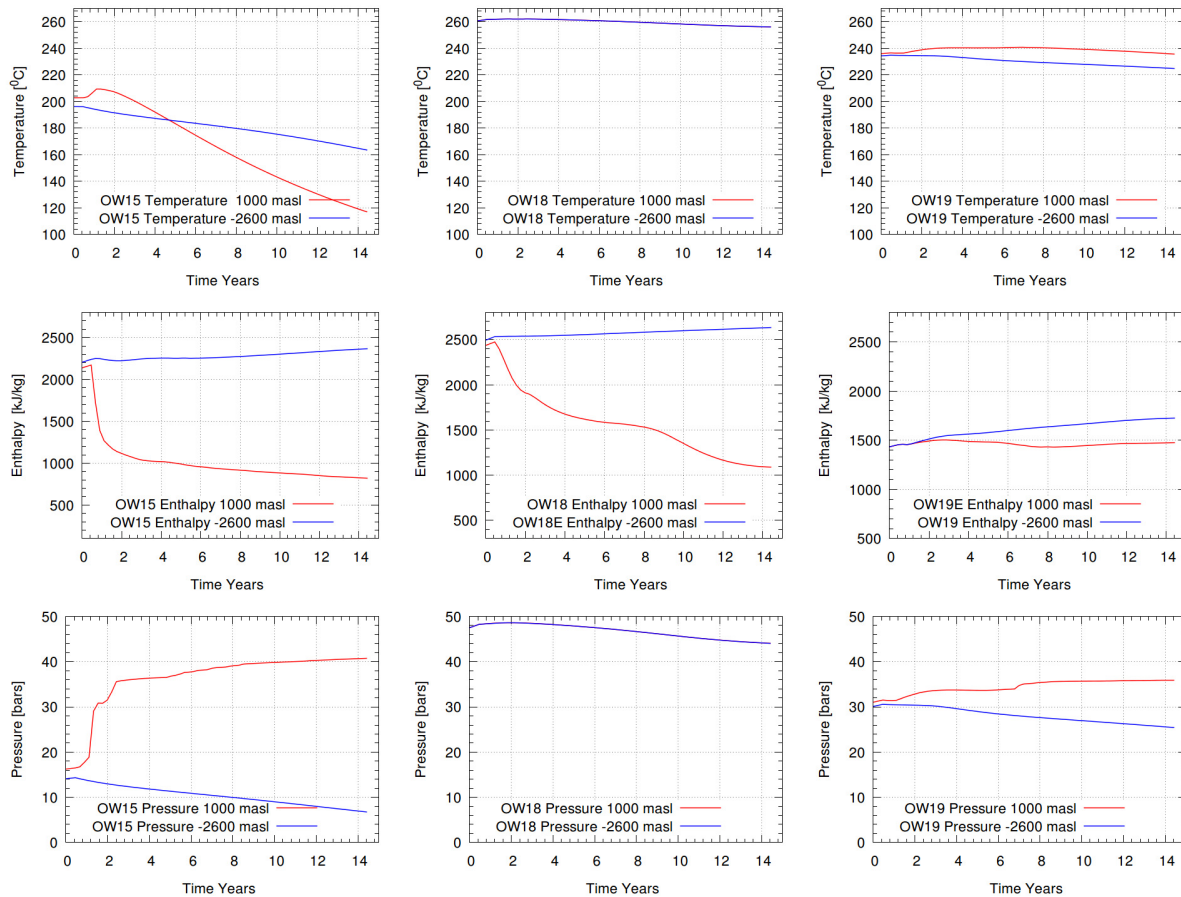
FIGURE 32: Comparison of field response to deep (-2600 m a.s.l.) and shallow (1000 m a.s.l.). Reinjection in well OW-12 for wells OW-15, OW-18 and OW-19 at 50 kg/s injection rate. Deep reinjection plotted (purple) and shallow (red)

which is the most affected well, in the complex model it takes about 4 years at 50kg/s injection rates for temperature to decline from the initial value.

Thermal front advance compares well for both models, it takes about a year to be felt in production well. Onset of cooling is immediate for single fracture model but in numerical model there is temperature rise followed by decline. This temperature increase before decline in the complex model is attributed to the steam cap collapse. The thermal velocity as observed in well OW-15 (218 m from injection well OW-12) is 0.15 m/day. According to the tracer test inversion with single fracture model, fluid flow velocity was approximated to be in the range of 4.5 m/day to 8 m/day. The ratio of fluid velocity and thermal breakthrough (thermal velocity) is determined to be 30-53. Table 5 shows the cooling prediction comparison.

TABLE 5: Cooling prediction comparison for single fracture model and complex numerical reservoir model

Model	Single fracture		Complex numerical
Well No	Pessimistic version (H~5b)	Optimistic version (H~30b)	
OW-15	20°C	16°C	40°C
OW-18	6°C	2°C	4°C
OW-19	6°C	4°C	(Increase 4°C)

7. SUMMARY

The results of a single fracture model tracer inversion using TRINV were used as input for cooling predictions for in-field reinjection in the Olkaria East Field using software TRCOOL (part of ICEBOX programs) during long term injection (15 years). Pessimistic version of the model predicts well OW-15 to cool by more than 20°C, wells OW-18 and OW-19 to cool by about 6°C. The optimistic model version predicts well OW-15 to cool by 16°C, OW-18 to cool by 2°C and well OW-19 to cool by 4°C for the same period.

The results of the natural state simulation for Olkaria East and Southeast sectors shows that the model developed simulates formation pressure and temperature quite well except for a systematic misfit in the cap rock and slightly in the steam cap, this can be explained by well drilling times, as some wells were drilled after exploitation had begun. Observed and simulated contours show that the model captures the convection plume propagation from bottom to the top. Mass flow vectors extracted from the model in the natural state shows the prevailing north to south flow field in the reservoir domain in the pre-exploitation state. The dominant heat transfer process is convection and the resulting heat flow vectors indicate a comparable flow field.

The pressure drawdown data from wells that once served as producing wells can be unreliable as the draw down noted could be localized due to near-by production and may not be representative of the reservoir. Field response to the increase in total mass produced in 1996 is captured by the model, simulated drawdown curves shows decline in 1996 just when the pressure drawdown in the field was beginning to stabilize. Overall, the model underestimates the observed pressure drawdown but captures the general decline trend associated with increasing production.

Enthalpy at the well head for flowing wells was used to calibrate the production model. There is a fairly good match seen for some wells, but underestimation for others, while the general trend is captured. It should be noted that the enthalpy is measured at the well head and is the aggregate for all the feed zones in a given well. Simulated enthalpy is the weighted enthalpy for the feed zones assigned for each well in the model. As such getting a perfect match is a challenge considering that the precise mass flow for each feed zone has to be quantified and assigned accordingly. Field monitoring data is collected twice a year for the accessible wells and for non-monitored wells observations from previous years are extrapolated, which can explain the discrepancies in some points. Some wells have time varying cyclic production especially when there are multiple feed zones and enthalpy difference is significant. Monitoring data involves spot readings averaged for a short period. The reservoir system under study is two-phase and a small change in steam fraction brings about big changes in enthalpy. The enthalpy drop noted in well OW-15 during reinjection in OW-12 is captured in the production model.

The tracer breakthrough curves observed in the field data suggest presence of flow channels connecting wells OW-15, OW-18 and OW-19 to OW-12. From interpreted geological structures the intersection of NE and NW trending fractures could imply presence of fractured region connecting these wells.

It was not possible to reduce the permeability to the extent of matching the field data with the current numerical model computational grid. The simulation deteriorated due to numerical dispersion, a phenomenon associated with advection dominated transport. Peaceman (1977) showed that numerical dispersion, during solving of the advection equation, is a function of grid block size and time step size. Since grid size was fixed, time step was reduced, but tracer breakthrough curves could not be matched successfully even after increasing the hydraulic conductivity for the defined flow channel connecting the four wells. Use of Multiple Interacting Continua (MINC) to enhance the resolution of spatial discretization in the flow channel was fairly successful, although it was only applied to a small volume around injection well OW-12. With MINC there was an improved fit in the tracer breakthrough curves. Time scales were captured but the maximum concentration at peaks was not matched. This was because the flow field existing in the reservoir was not fully captured by the MINC model. Small fracture porosity, i.e. the product of fracture zone porosity and fracture zone volume fraction, was assigned to the MINC domain.

In deeper re-injection the flow path to OW-19 (deep well) is shorter and it experiences more cooling than was in the case of shallow injection. While for OW-15 the flow path is longer and less cooling is experienced. With deep reinjection the steam cap is maintained and enthalpy increases slightly. This can be countered by increasing injected mass. It is recommended that for detailed evaluation of the benefits of different reinjection schemes, it is advisable to couple well flows into the simulation. The actual production well head mass flows and parameters can be simulated and the gains with reinjection quantified in total heat extracted from the reservoir rocks for the different scenarios. In this study wells are simulated with fixed mass production assigned to the elements along the well trajectory. The area between deep and shallow reinjection enthalpy curves, for production wells, represent the net gain in heat mined by injecting deeper.

8. CONCLUSIONS AND RECOMMENDATIONS

A numerical reservoir model was developed for the Olkaria East and Southeast fields. It covers an area of 27 km^2. The natural state model matched well available temperature and pressure data. The model was also validated on production history and monitoring data.

Thermal front propagation was captured in the numerical reservoir model. Comparison of thermal front breakthrough for OW-15, which is the most affected well, shows that in the numerical model it takes about 4 years at higher injection flow rates (50 kg/s) for temperature to decline from the initial value. Thermal front advance compares well for both single fracture and complex three dimensional model, it takes about a year to be felt in production wells. Onset of cooling is immediate for single fracture model but in the numerical model there is a temperature rise followed by decline.

The modelling results show that well OW-12 can be used as a cold reinjection well, but it has to be used intermittently, injection for one year and a period of recovery for shallow reinjection, i.e. at the current depth. If finished deeper (-2600 m a.s.l.) longer injection periods are possible without collapsing of the steam cap.

Recovery of tracers in wells to the south of the injection well confirms the conceptualized north-south flows existing in the Olkaria system.

It is recommended that the well feed zones be located and the corresponding mass flows estimated, together with their thermophysical properties, during discharge testing. Continued use of a numerical model to simulate reinjection and predict pressure and temperature interference in the production zone, is also proposed. The use of wellbore flow simulators to estimate well head flow parameters in investigating gains made by deep reinjection is, furthermore, recommended. The actual heat mined can be better estimated while simulating wells on deliverability.

Tracer testing is an important tool in reservoir characterization. In fractured reservoirs with low permeability matrix and high permeable flow channels/fractures the tracers may reveal the heterogeneities in the reservoir. Integrating tracer tests and other well testing methods to complement each other is beneficial. Rivera (1995) suggests that interference tests be performed to establish reservoir connectivity between wells in the field for effective selection of injection wells. He further points out that interpretation of interference data alone may not be conclusive as both a layered and a naturally fractured system both produce similar pressure response to a change in flow rate. By complementing the two methods, reservoir flow channels can be better characterized.

Numerical reservoir models can be used in the design of tracer tests. To estimate the minimum quantity of tracer required for breakthrough at the producing wells, knowledge of flow patterns is used to determine the first arrival times and the peak arrival times of the tracer and also to infer the tracer distribution in the reservoir. Appropriate sampling points (wells) and sampling frequency can be determined.

Tracer tests are to be carried out to determine the connectivity of planned re-injection wells. Production response of the production wells near injection wells are to be monitored. The enthalpy, well head and where possible the downhole temperature and pressure logs, and the fluid chemistry must also be monitored. The results of the tests are to be modelled to predict cooling in the production wells as affected by re-injection.

Advanced tracer test techniques like multilevel or multiple tracers could be applied. With multilevel sampling technique, feed zones location and inflow rates can be determined. In multilevel sampling, packers are used to separate the well into different depths sections so that individual breakthrough curves are obtained for the respective feed zone (Ptak and Schmid, 1996).

Numerical reservoir production model can be complemented with single fracture models to predict thermal break through where spatial and temporal discretization is limited by computing resources. This

way the flow field is captured by the numerical reservoir model and the advective nature of fracture channel flows will be captured by single fracture simple model.

It is recommended that a finer mesh is used to explicitly define the fractures when computing resources (High Performance Computing clusters) are available; Multiple Interacting Continua (MINC) can also be implemented for irregular shapes. In this study a regular grid created with inbuilt TOUGH2 Meshmaker was used as an input to MINC partitioning program also inbuilt in TOUGH2.

Fluorescein (a fluorescent dye) tracer has been used in Olkaria, which has the draw-back of decaying at temperatures above 200°C. The use of naftalene-sulfonates, or other tracers that can tolerate higher temperatures is recommended. Due to the two phase nature of the Olkaria reservoir it is recommended to use two phase tracers or a combination of liquid and steam phase tracers to gain comprehensive insight into the flow channel flows and mobility between phases

REFERENCES

Adams, M.C. and Davis, J. 1991: Kinetics of fluorescein decay and its application as a geothermal tracer. *Geothermics, 20,* 53-66.

Ambusso, W.J. and Ouma, P.A. 1991: Thermodynamic and permeability structure of Olkaria North-east geothermal field: Olkaria fault. *Geothermal Resources Council, Trans.,, 15,* 237-242.

Arason, Th., and Björnsson, G. 1994: *ICEBOX.* (2nd edition). Orkustofnun, Reykjavík, 38 pp.

Axelsson, G. 2013a: Tracer tests in geothermal resource management. *EPJ Web of Conferences, 02001 EDP Sciences, 50,* 8 pp.

Axelsson, G., 2013b: *Tracer tests in geothermal resource management: analysing and cooling predictions.* Manuscript in preparation.

Axelsson, G., Arnaldsson, A., Ármannsson, H., Árnason, K., Einarsson, G., Franzson, H., Fridriksson, T., Gudmundsson, G., Gylfadottir, S.S., Halldórsdóttir, S., Hersir, G.P., Mortensen, A.K., Thordarson, S., Jóhannesson, S., Bore, C., Karingithi, C., Koech, V., Mbithi, U., Muchemi, G., Mwarania, F., Kizito, O., and Ouma, P., 2013a: Updated conceptual model and capacity estimates for the Greater Olkaria geothermal system, Kenya. *Proceedings of the 38th Workshop on Geothermal Reservoir Engineering, Stanford University, CA,* 16 pp.

Axelsson, G., Arnaldsson, A., Gylfadottir, S.S., Halldórsdóttir, S., Mortensen, A.K., Bore, C., Karingithi, C., Koech, V., Mbithi, U., Muchemi, G., Mwarania, F., Kizito, O., and Ouma, P., 2013b: Conceptual model and resource assessment for the Olkaria Geothermal System, Kenya. *Proceedings of Short Course V on Conceptual Modelling of Geothermal Systems, organised by UNU-GTP and LaGeo, Santa Tecla, El Salvador,* 21 pp.

Axelsson, G., Björnsson, G. and Montalvo, F. 2005: Quantitative interpretation of tracer test data. *Proceedings of the World Geothermal Congress 2005, Antalya, Turkey,* 12 pp.

Axelsson, G., Flóvenz, O. G., Hauksdottir, S., Hjartarson, A. and Liu, J. 2001: Analysis of tracer test data, and injection-induced cooling, in the Laugaland geothermal field, N-Iceland. *Geothermics, 30,* 697–725.

Beall, J.J., Adams M.C. and Hirtz P.N. 1994: R-13 Tracing of injection in the Geysers. *Geothermal Resources Council, Trans. 18,* 151-159.

Benoit, W.R., and Stock, D., 1993: A case history of injection at the Beowawe, Nevada geothermal reservoir. *Geothermal Resources Council, Trans., 17,* 473-480.

Berry. P., Honduá S., Bortolotti V and Cormio C. 2012: TOUGH2Viewer: a post-processing tool for interactive 3D visualization of locally refined unstructured grids for TOUGH2, *Computers and Geosciences, Elsevier, 46,* 107–118.

Bodvarsson, G. 1972: Thermal problems in siting of reinjection wells. *Geothermics, 1-2,* 63-66.

Bödvarson, G.S., Pruess K. and O`Sullivan, M.J. 1985: Injection and energy recovery in fractured geothermal reservoirs. *Soc. Pet. Eng. J., 25,* 303-312.

Bödvarsson, G.S. and Pruess, K. 1987: *Numerical simulation studies of the Olkaria geothermal field.* Kenya Power Company Ltd., internal report.

Bödvarsson, G.S., and Witherspoon, P., 1989: Geothermal reservoir engineering, part I. *Geothermal Science and Technology, 2-1,* 1-68.

Capetti, G., Parisi, L., Ridolfi, A. and Stefani, G. 1995: Fifteen years of reinjection in the Larderello-Valle Secolo area: Analysis of the production data. *Proceedings World Geothermal Congress 1995, Florence, Italy*, 1997–2000.

Clarke, M.C.G., Woodhall, D.G., Allen, D. and Darling G. 1990: *Geological, volcanological and hydrogeological controls on the occurrence of geothermal activity in the area surrounding Lake Naivasha, Kenya, with coloured 1:100 000 geological maps.* Ministry of Energy, Nairobi, 138 pp.

Chorowicz, J. 2005: The East African rift system. *J. African Earth Science*, *43 / 1-3*, 379-410.

Divine C.E., and McDonnell, J.J., 2005: The future of applied tracers in hydrogeology. *Hydrology, Journal, 13*, 117-138.

Driscoll, F.G., 1986: *Groundwater and wells* (2nd ed). Johnson Division, 1089 pp.

Ghergut I., Sauter M., Behrens H., Licha T., Tischner T. and Jung. R. 2009: Single-well dualtracer spikings during EGS creation in Northern-German sedimentary layers. *Proceedings of the 34th Stanford Workshop on Geothermal Reserrvoir Engineering, Stanford, CA*, SGP-TR-187.

González-Vargas, C., Moya-Rojas, P., Sánchez-Rivera, E., Vallejos-Ruiz, O. and Yock-Fung, A. 2005: Evolution of the Miravalles geothermal field in Costa Rica after ten years of exploitation. *Proceedings of the World Geothermal Congress 2005 Antalya, Turkey.*

Goyal, K.P., and Conant, T.T., 2010: Performance history of The Geysers steam field, California, USA. *Geothermics*, *39*, 321–328.

Grant, M.A. and Bixley, P.F., 2011: *Geothermal reservoir engineering* (2nd ed.). Academic Press, NY, 323 pp.

Haukwa, C.B., 1984: *Recent measurements within Olkaria East and West fields.* Kenya Power Co., internal report, 13 pp.

Haukwa, C.B., 1998: *A mesh creating program for the integral finite difference method: User's manual.* Lawrence Berkeley National Laboratory, Berkeley, CA, report LBNL-45284, 53 pp.

International Formulation Committee, 1967: A formulation of the thermodynamic properties of ordinary water substances. IFC Secretariat, Düsseldorf, Germany.

Kamau, M., and Odeny, J., 1997: *Effects of cold injection in OW-12 on the Olkaria East production wells*. KenGen, internal report.

Kocabas, I.., Axelsson G., and Björnsson, G., 1996: Interpretation of the Return profile of a tracer test in the Thelamörk geothermal field, Iceland. *Proceedings of the. 21st Workshop on Geothermal Reservoir Engineering, Stanford University, Stanford, CA,* 399-405.

Kocabas, I., and Horne, R. 1987: *Analysis of injection-back-ow tracer tests in fractured geothermal reservoirs.* Stanford University, Stanford, CA, technical report.

Kreft, A., and Zuber, A. 1978: On the physical meaning of the dispersion equation and its solutions for different initial and boundary conditions. *Chemical Engineering Science*, *33*, 1471–1480.

Leibundgut, C., Maloszewski, P., and Kúlls, C. 2009: *Tracers in hydrology*. John Wiley & Sons, New Delhi, 441 pp.

Lenda, A., and Zuber, A., 1970: Tracer dispersion in groundwater experiments. International Atomic Energy Agency. *Isotope Hydrology, Vienna,* 619-641.

Liou, T. S. 2007: Numerical analysis of a short-term tracer experiment in fractured sandstone. *Terr.Atmos. Ocean. Sci.*, *18*, 1029-1050.

Lippmann, M.J., Truesdell, A.H., Rodríguez, M.H., and Pérez, A., 2004: Response of Cerro Prieto II and III (Mexico) to exploitation. *Geothermics*, *33*, 229–256.

Lippmann, M.J., Tsang, C.F., and Witherspoon, P.A., 1977: *Analysis of the response of geothermal reservoirs under injection and production procedures.* SPE Paper 6537.

Maloszewski, P. 1994: *Mathematical modelling of tracer experiments in fissured aquifers.* Freiburger Schriften zur Hydrologie, 2, Freiburg, 107 pp.

Maloszewski, P., Herrmann, A., and Zuber, A., 1999: Interpretation of tracer tests performed in fractured rock of the Lange Bramke basin, Germany. *Hydrogeology Journal*, *7*, 209–218.

Maloszewski, P., and Zuber, A. 1985: On the theory of tracer experiments in fissured rocks with a porous matrix. *Journal of Hydrology*, *79*, 333–358.

Maloszewski, P., and Zuber, A., 1990: Mathematical modeling of tracer behavior in shortterm experiments in fissured rocks. *Water Resour. Res.*, *26*, 1517-1528.

Maloszewski, P., and Zuber A. 1993: Tracer experiments in fractured rocks: Matrix diffusion and the validity of models. *Water Resour. Res.*, *29*, 2723-2735.

Mathworks, 2011: *Curve fitting toolbox, user's guide* (r2011b): Mathworks webpage: *www.mathworks.com/help/pdf_doc/gads/gads_tb.pdf.*

Mwawongo, G.M., 2004: Infield re-injection strategies in Olkaria, Kenya, based on tracer studies and numerical modelling. Report 12 in: *Geothermal training in Iceland 2004.* UNU-GTP, Iceland, 239-266.

Odongo, M.E.O. 1993: A geological review of Olkaria geothermal reservoir based on structure. *Proceedings of the 15th New Zealand Geothermal Workshop, Auckland, NZ,* 169-173.

Ofwona, C.O. 2002: *A reservoir study of Olkaria East geothermal system, Kenya.* University of Iceland, M.Sc. thesis, UNU-GTP, Iceland, report 1, 86 pp.

Omenda, P.A., 1994: The geological structure of the Olkaria west geothermal field, Kenya. *Proceedings of the 19th Stanford Geothermal Reservoir Engineering Workshop, Stanford, CA,* 125-130.

Omenda, P.A. 1998: The geology and structural controls of the Olkaria geothermal system, Kenya. *Geothermics, 27-1*, 55-74.

O'Sullivan M.J., Pruess K. and Lippmann M.J. 2001: State of the art of geothermal reservoir simulation. *Geothermics, 30-4,* 395-429.

Peaceman, D. W. 1977: *Fundamentals of numerical reservoir simulation.* Amsterdam Elsevier, 176 pp.

Pruess, K., 2002a: *Mathematical modelling of fluid and heat transfer in geothermal systems.* UNU-GTP, Iceland, report 3, 92 pp.

Pruess, K. 2002b: Numerical simulation of multiphase tracer transport in fractured geothermal reservoirs. *Geothermics*, 31, 475-499.

Pruess, K., Oldenburg, C. and Moridis, G. 1999: *TOUGH2, user's guide version 2.0.* Lawrence Berkeley National Laboratory, 197 pp.

Ptak T., and Schmid, G., 1996: Dual-tracer transport experiments in a physically and chemically heterogeneous porous aquifer Effective transport parameters and spatial variability. *Journal of Hydrology*, *183(1-2),* 117-138.

Rivera, J., 1995. *Reservoir engineering aspects related to injection*. International Geothermal Association, Auckland, NZ.

Rose, P.E., Apperson K.D., Johnson S.D., and Adams M.C., 1997: Numerical simulation of a tracer test at Dixie Valley, Nevada. *Proceedings of the 22nd Workshop on Geothermal Reservoir Engineering, Stanford, CA,* 169-176.

Shook, G.M., 1999: Prediction of thermal breakthrough from tracer tests. *Proceedings of the 24th Workshop on Geothermal Reservoir Engineering, Stanford, CA,*, SGP-TR-162.

Steingrímsson, B., Aunzo Z., Bödvarsson, G.S., Truesdell, A.H., Cuellar, G., Eseobar, C. and Quintanilla, A., 1991: Changes in thermodynamic conditions of the Ahuachapan reservoir due to production and injection. *Geothermics, 20, 23-38.*

Sudicky, E.A., and Frind E.O. 1982: Contaminant transport in fractured porous media: Analytical solutions for a system of parallel fractures. *Water Resour. Res, 18*, 1634- 1642.

Sugiaman, F., Sunio, E., Mollin, P., and Stimac, J., 2004: Geochemical response to production of the Tiwi geothermal field, Philippines. *Geothermics*, *33*, 57–86.

Sweco - Virkir. 1980: *Feasibility report for the Olkaria geothermal project*. UN - Government of Kenya, unpublished report.

Thompson, A.O., and Dodson, R.G., 1963: Geology of the Naivasha area, Kenya. *Kenya Geological Survey*. Report 55.

West-JEC, 2009: *The Olkaria optimization study (phase II)*. West Japan Engineering Consultants, Inc., unpublished optimization development report, 163 pp.

Woods, A.W., and Fitzgerald S.D., 1993: The vaporization of a liquid front moving through a hot porous rock. *J. Fluid Mech.*, *251,* 563-579.

Wu, Y.S., and Pruess, K., 2000: Numerical simulation of non-isothermal multiphase tracer transport in heterogeneous fractured porous media. *Adv. Water Resour., 23*, 699-723.

Zuber, A. 1974: Theoretical possibilities of the two-well pulse method. In: *Isotope techniques in ground water hydrology*. International Atomic Energy Agency (IAEA), Hydrology Vol. II, 277-294.

APPENDIX A: Olkaria East wells

TABLE A-1: Well construction characteristics drilled depth, Production casing depth

Well no	Elevation (m a.s.l.)	Drilled depths (m)	9 5/8" casing (m)	Stable bottom hole temp(°C)	Total mass (t/hr)	Enthalpy kJ/kg
OW-1	2068.38	1003	418	126	_	_
OW-2	1941.61	1350	594.5	282	_	2400
OW-3	1957.8	1357	682	256	50	_
OW-4	1949.9	1661	698	289	20	_
OW-5	1928.76	910	660.6	256	_	_
OW-5	1928.76	910	661	_	_	_
OW-5	1928.76	2200	660.6	333	_	2627
OW-6	1930.14	1685	630	224	71	1800
OW-7	1938.94	1308	627	254	27.7	2200
OW-8	1941.3	1600	541.6	271	14.3	2310
OW-9	1927.54	1181.3	548.1	254	15	_
OW-10	1933.29	1183	547.8	274	13	2000
OW-11	1932.28	1221	514.7	270	36	2000
OW-12	1928.83	901	497	215	34.4	2100
OW-13	1921.08	1049	537.4	230	40.6	1950
OW-14	1948.4	1049	488.7	260	23.4	2800
OW-15	1925.92	1301.6	519.8	254	23	2400
OW-16	1929.31	1304	536.3	287	33.8	2400
OW-17	1936.09	1234	544.5	275	69.7	2200
OW-18	1941.61	1406	539.6	260	20.5	2200
OW-19	1931.88	2484.6	948.9	339	53.3	2000
OW-20	1934.99	1406	545.4	243	34	2400
OW-21	1921.52	1348	537.2	255	26	2650
OW-22	1923.93	1406	547	269	24	2400
OW-23	1942.28	1329	528	200	23	1900
OW-24	1935.27	1620	558.4	276	18	2500
OW-25	1941.58	1600	546.5	310	19	1850
OW-26	2006.47	1607.2	545	212	25	1900
OW-27	1991.53	2004	692	311	50	1670
OW-28	1942.24	1605	493	306	41.5	2000
OW-29	1958.6	1599	493	292	22	2360
OW-30	1959	1602	601	294	45	1744
OW-31	1978.47	2006	707.3	_	139	2435
OW-32	1968.01	2005	593	292	20	2413
OW-33	1975.59	2006	592	268	112	2440
OW-34	1948.88	2136	595.9	265	34	2597
OW-35	1971. 68					

APPENDIX B: Single fracture cooling prediction model flow channel parameters (estimated by tracer inversion)

TABLE B-1: Single fracture model parameters used in cooling prediction for production wells OW 15, OW 18 and OW 19 and injection well OW 12 (injection rate 27.8 kg/s) where x is the distance between wells, b the flow channel width or thickness, H its' height and φ its' porosity

OW 15	x =	217.8 m						
φ=0.1	B [m]	H[m]	φ=0.15	B [m]	H[m]	φ=0.20	B [m]	H[m]
H~5b	4.34	21.725	H~5b	3.549	17.73	H~5b	3.0728	15.329
H~10b	3.07	30.723	H~10b	2.5082	25.08	H~10b	2.1726	21.726
H~30b	1.77	53.2165	H~30b	1.448	43.451	H~30b	1.2526	37.678
OW 18	x =	281.5 m						
φ=0.1	B [m]	H[m]	φ=0.15	B [m]	H[m]	φ=0.20	B [m]	H[m]
H~5b	2.395	11.979	H~5b	1.956	9.78	H~5b	1.69	8.47
H~10b	1.694	16.9410	H~10b	1.383	13.83	H~10b	1.197	11.97
H~30b	0.978	29.3428	H~30b	0.739	22.18	H~30b	0.691	20.74
OW 19	x =	451.1 m						
φ=0.1	B [m]	H[m]	φ=0.15	B [m]	H[m]	φ=0.20	B [m]	H[m]
H~5b	2.21	11.0905	H~5b	1.81	9.0553	H~5b	1.69	8.4707
H~10b	1.568	15.684	H~10b	1.280	12.80	H~10b	1.197	11.97
H~30b	0.905	27.166	H~30b	0.73	22.18	H~30b	0.69116	20.7449

APPENDIX C: Reservoir formation (steady state temperature and pressure) and natural state model simulation plots
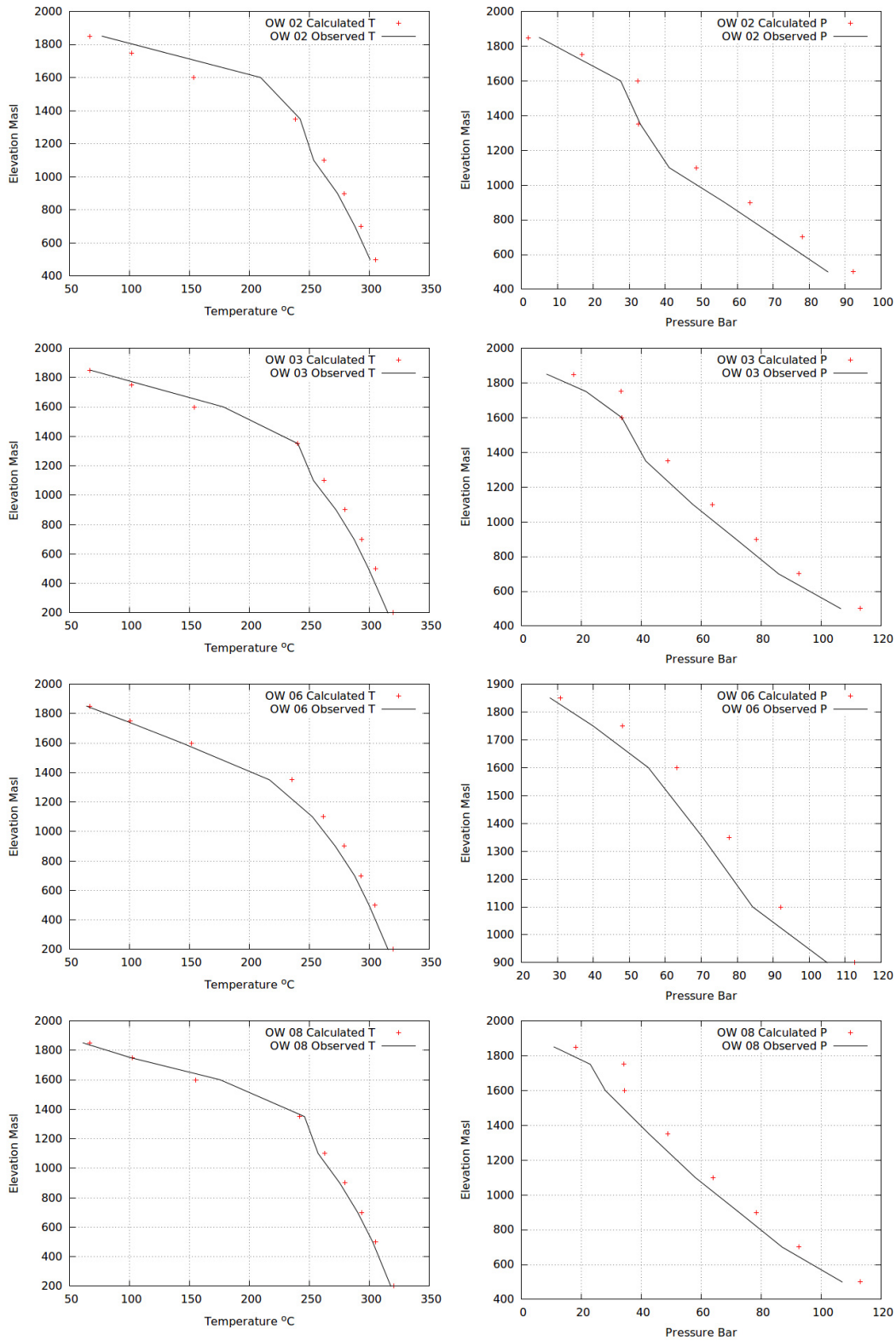
FIGURE C.1: Reservoir formation (Steady state temperature and pressure) and numerical natural state model simulations Plots for wells OW-02, OW-03, and OW-08
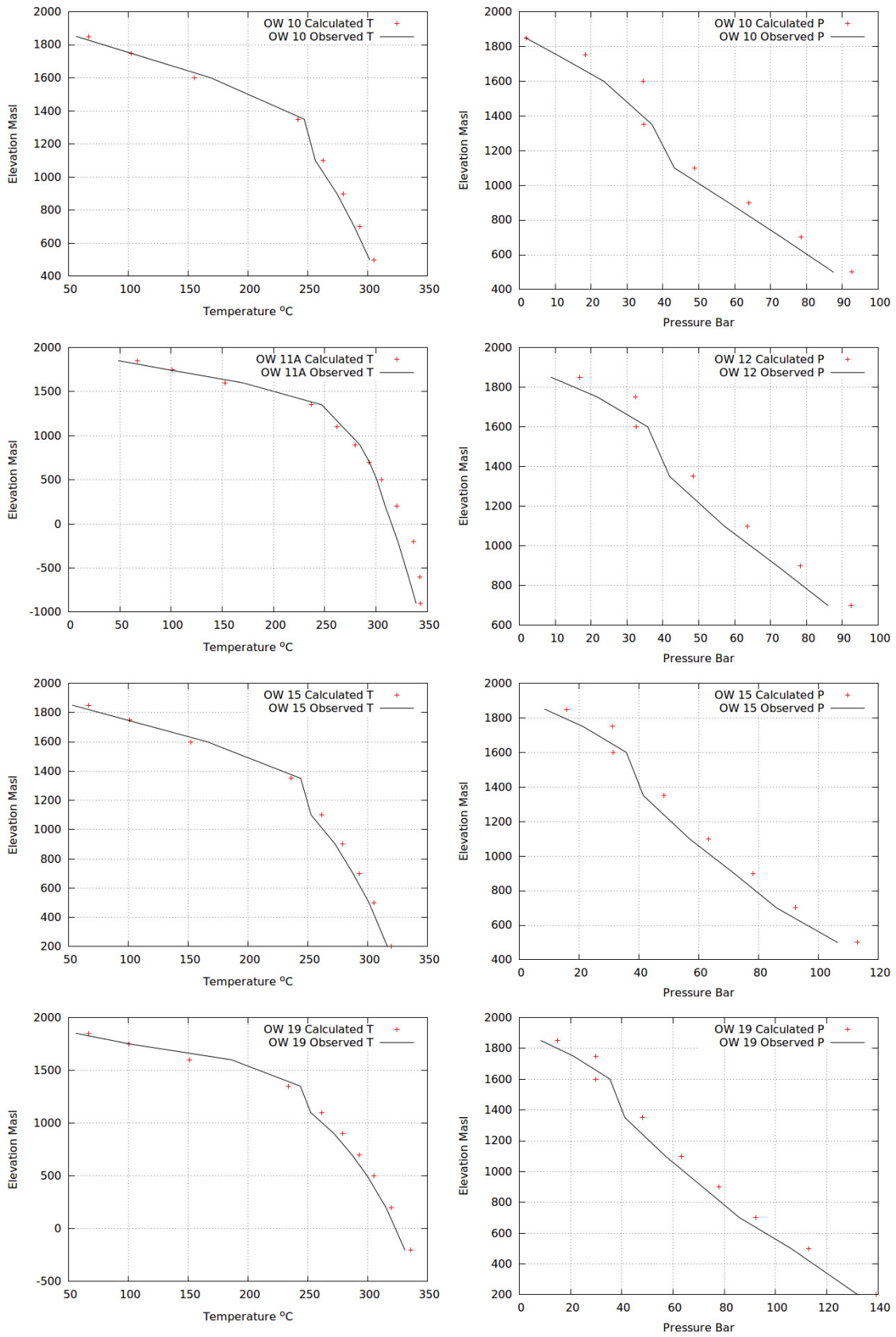
FIGURE C.2: Reservoir formation (Steady state temperature and pressure) and numerical natural state model simulations Plots for wells OW-10, OW-11, OW-15 and OW-19
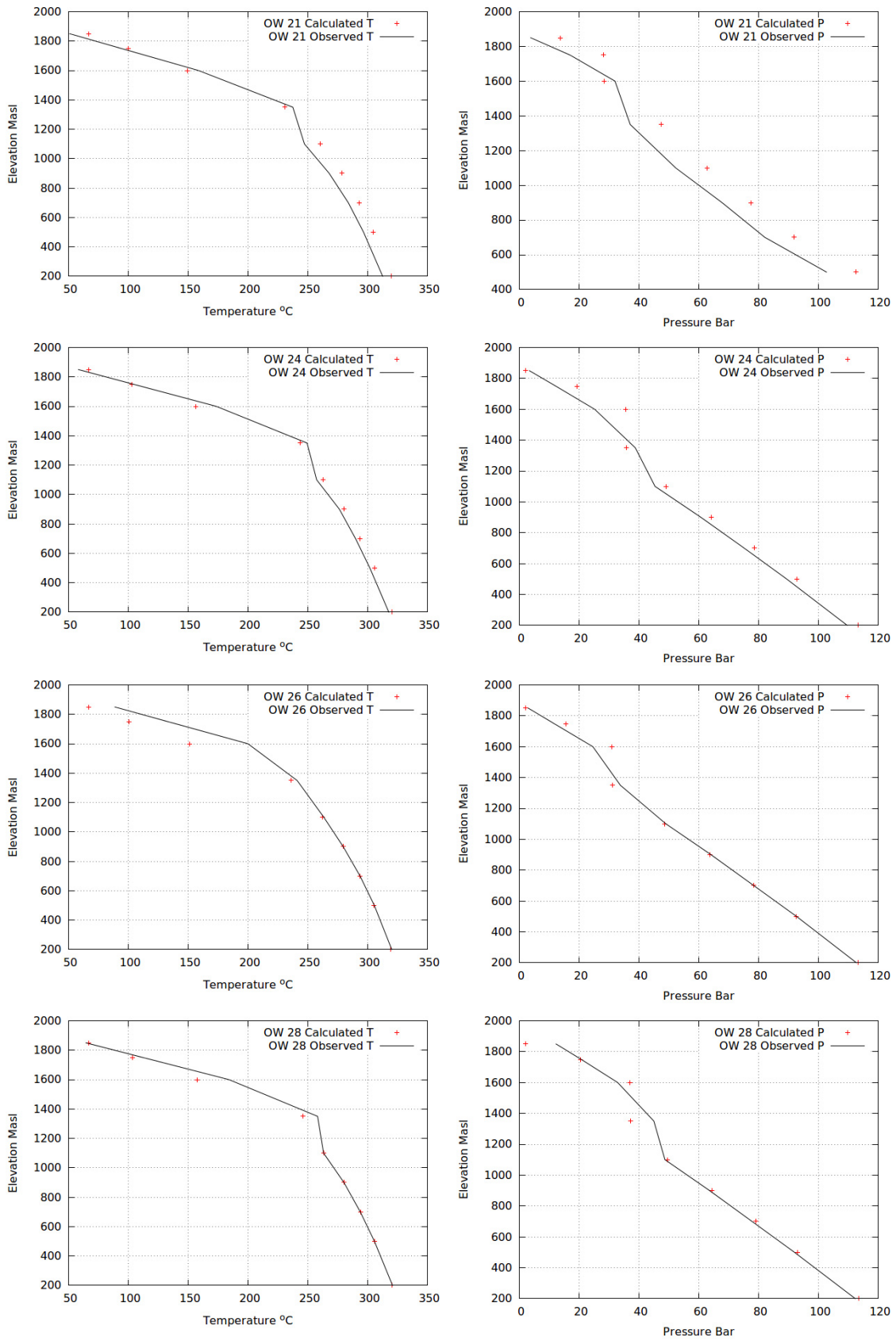
FIGURE C.3: Reservoir formation (Steady state temperature and pressure) and numerical natural state model simulations Plots for wells OW-21, OW-24, OW-26 and OW-28
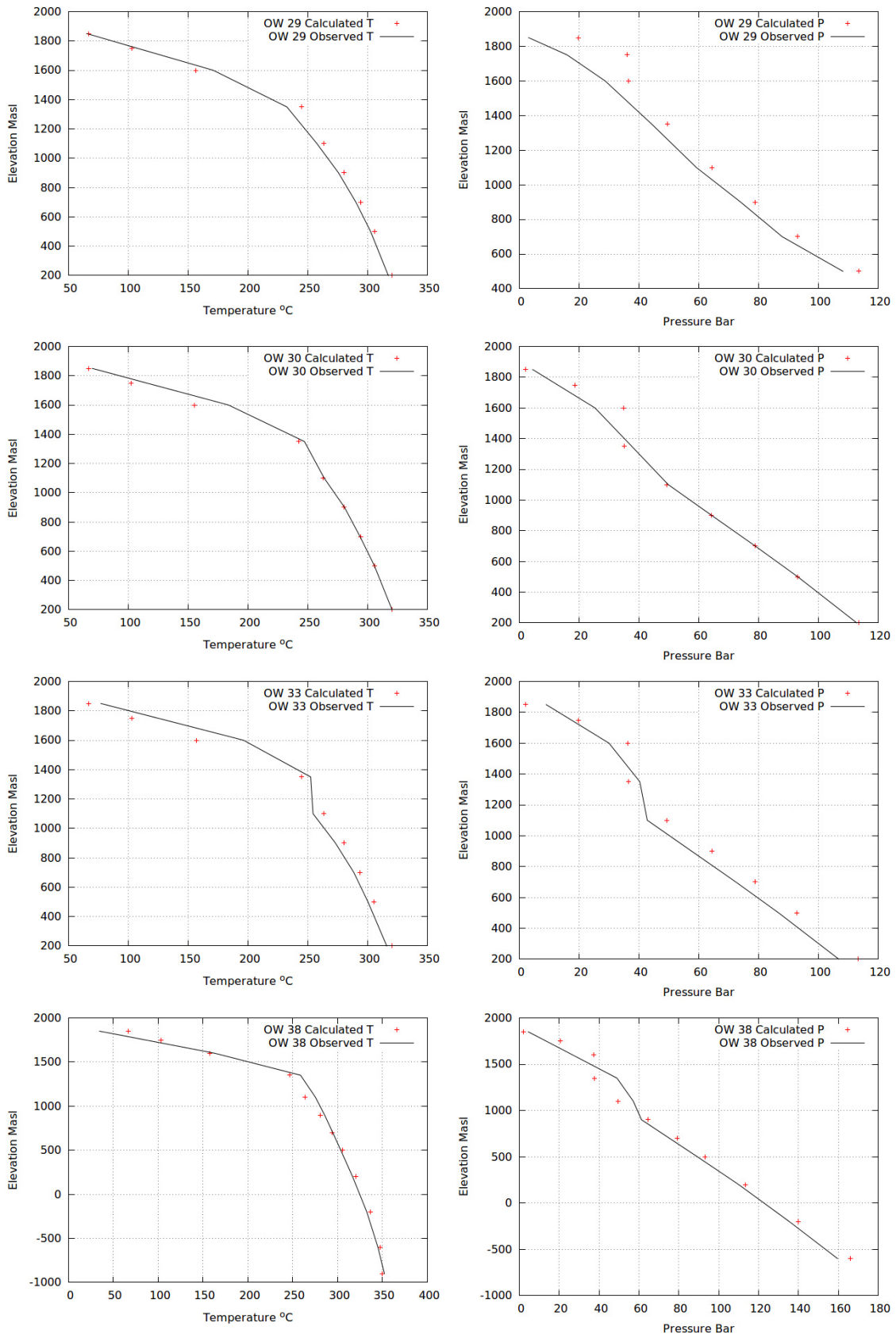
FIGURE C.4: Reservoir formation (Steady state temperature and pressure) and numerical natural state model simulations Plots for wells OW-29, OW-30, OW-33 and OW-38
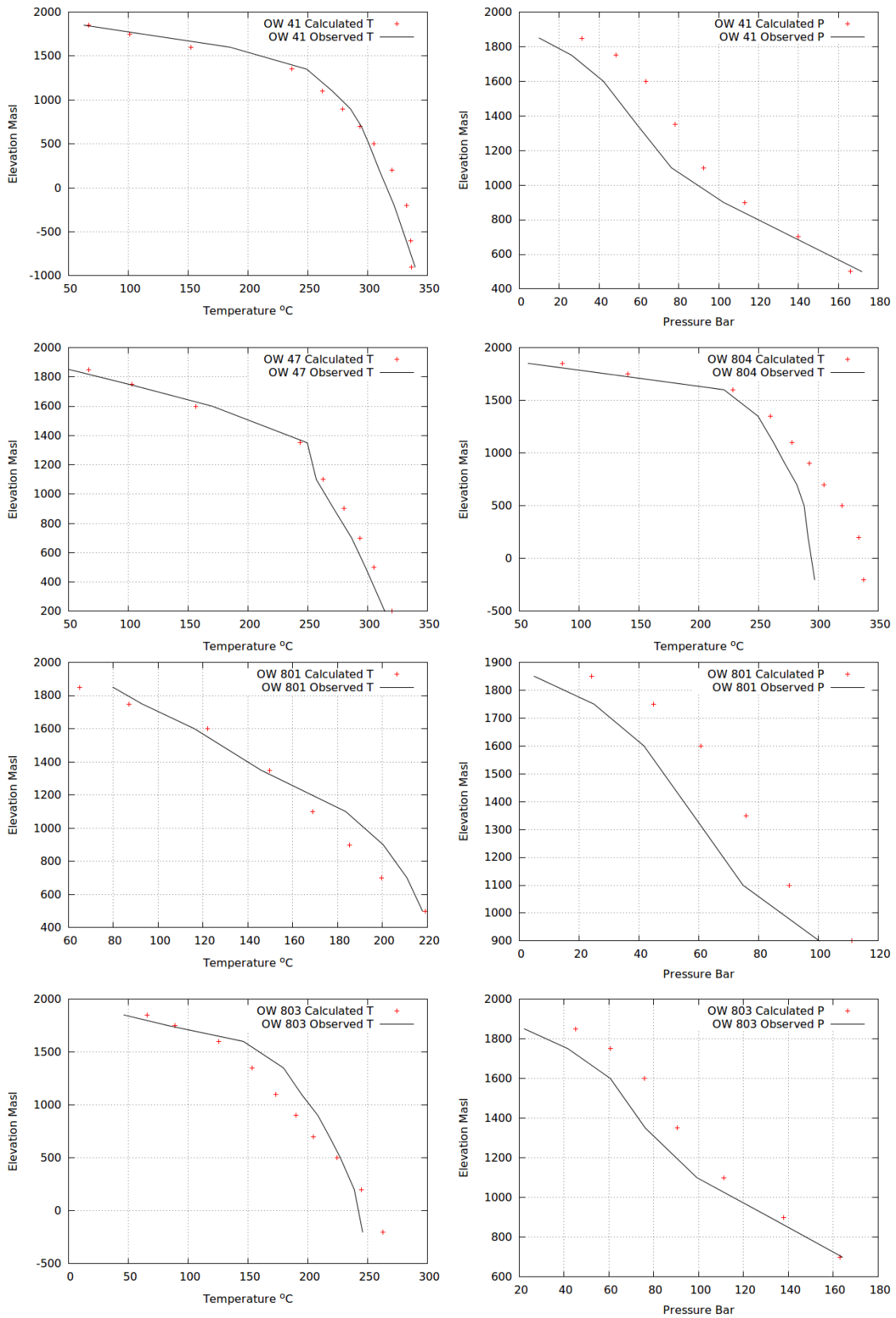
FIGURE C.5: Reservoir formation (Steady state temperature and pressure) and numerical natural state model simulations Plots for wells OW-41, OW-47, OW-801, and OW-803

57
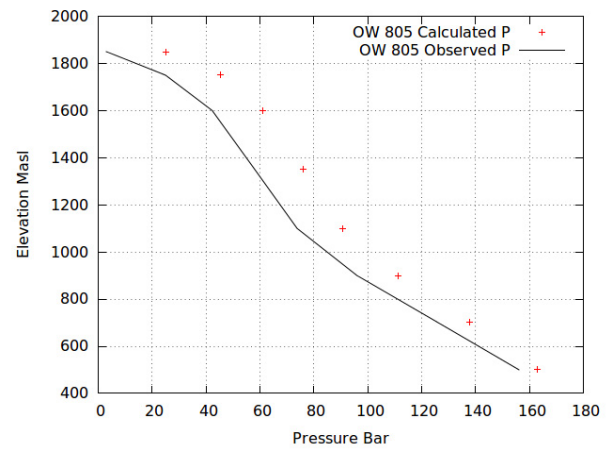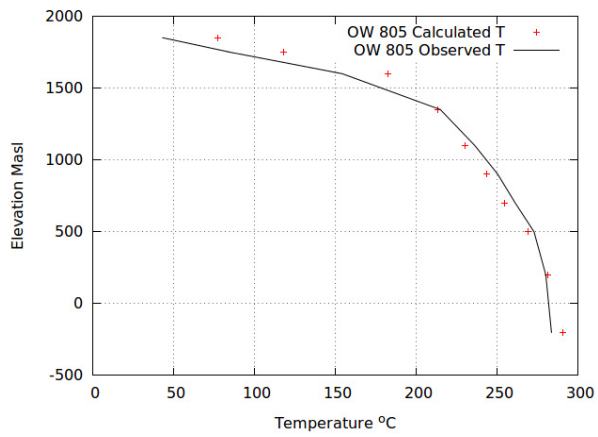
FIGURE C.6: Reservoir formation (Steady state temperature and pressure) and numerical natural state model simulations Plots for wells OW-805

APPENDIX D: Natural state model and estimated temperature comparison contours
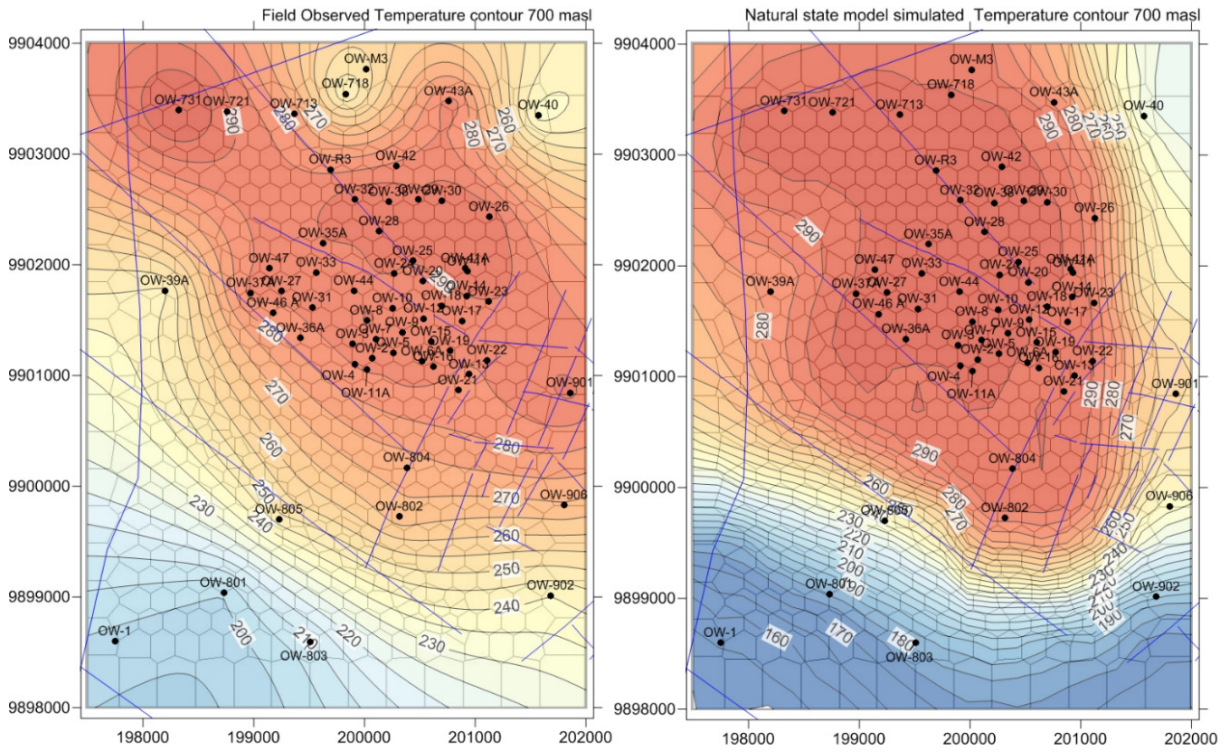
FIGURE D.1: Comparison between estimated (left) and simulated (right)
temperature contours at 700 m a.s.l. (LayerG)
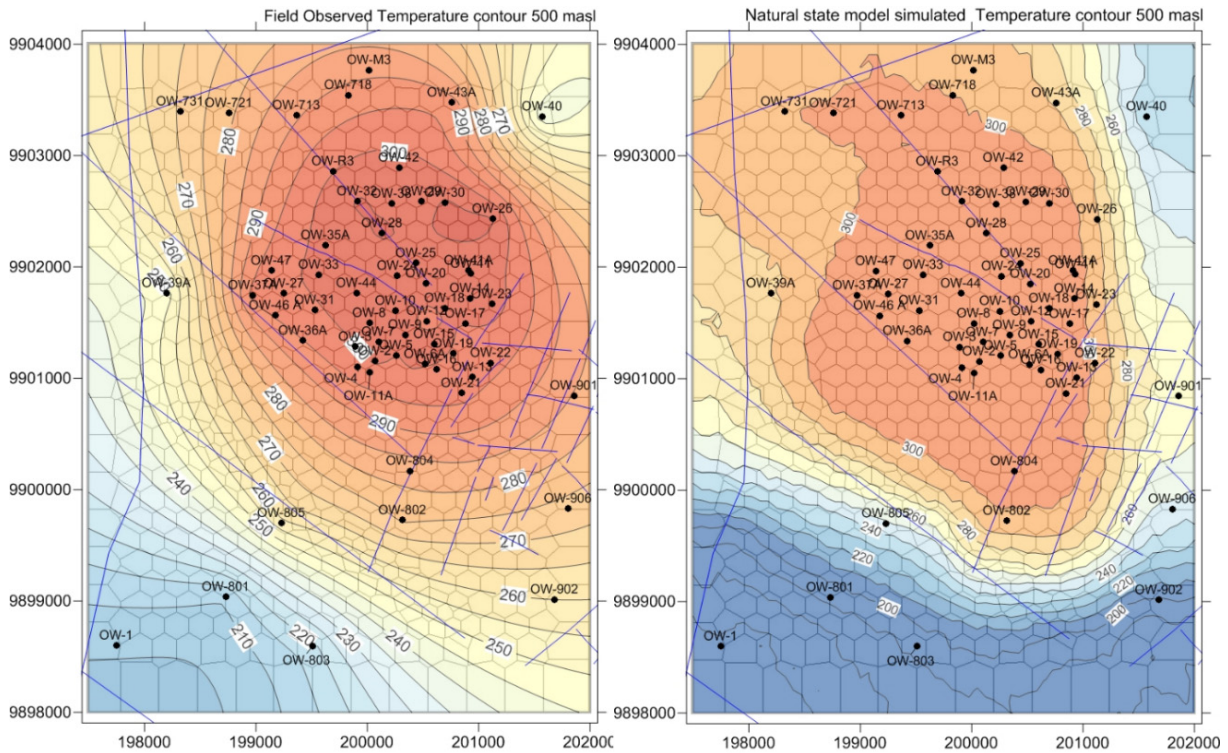
FIGURE D.2: Comparison between estimated (left) and simulated (right)
temperature contours at 200 m a.s.l. (LayerI)
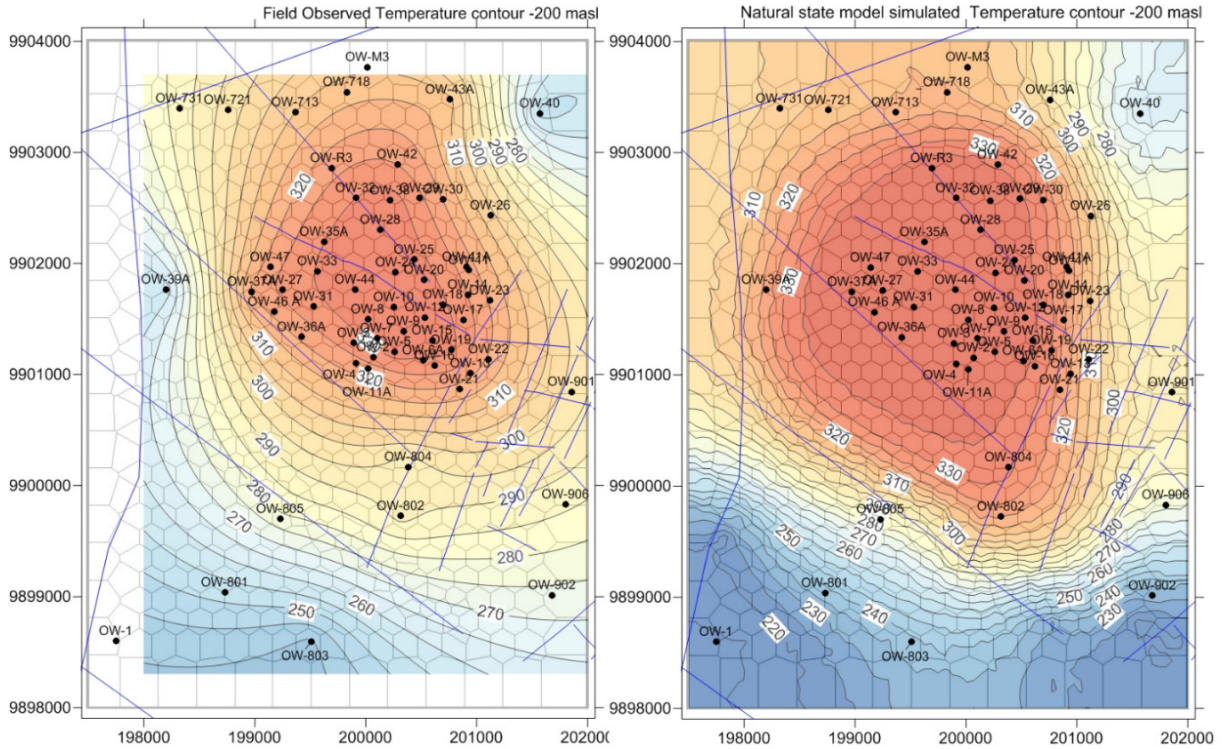
FIGURE D.3: Comparison between estimated (left) and simulated (right)
temperature contours at -200 m a.s.l. (LayerJ)
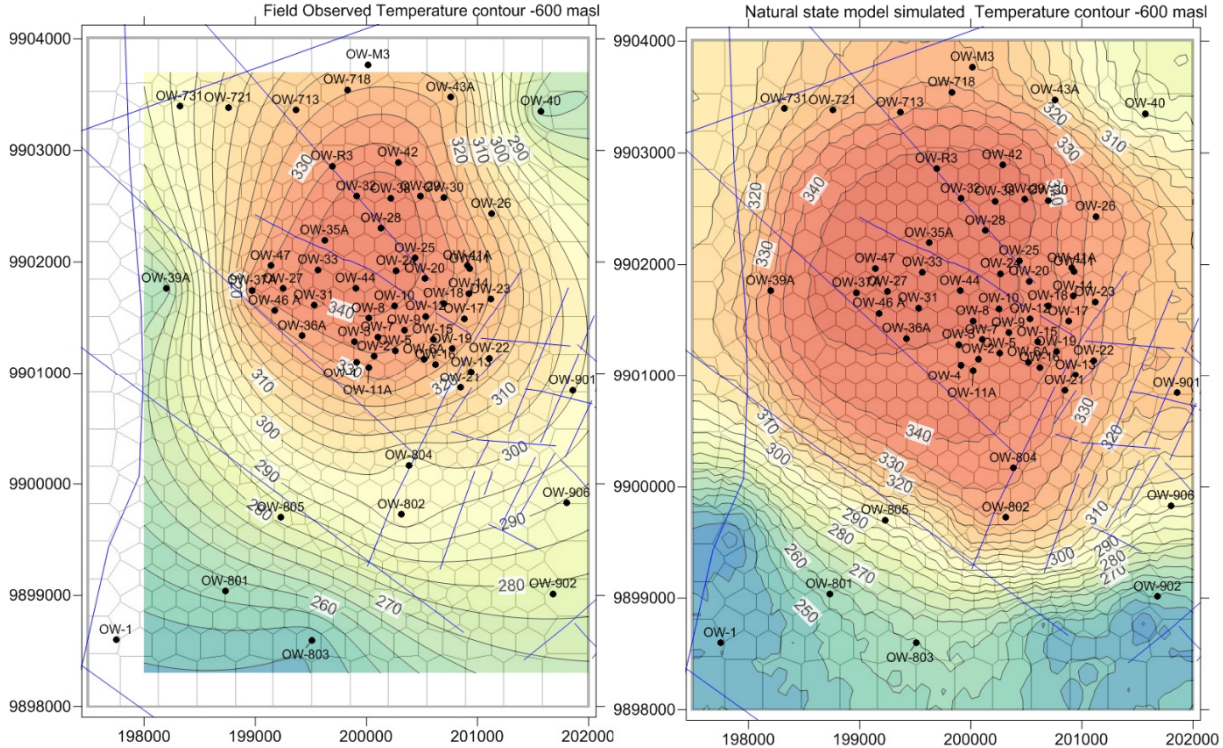
FIGURE D.4: Comparison between estimated (left) and simulated (right)
temperature contours at -600 m a.s.l. (LayerK)
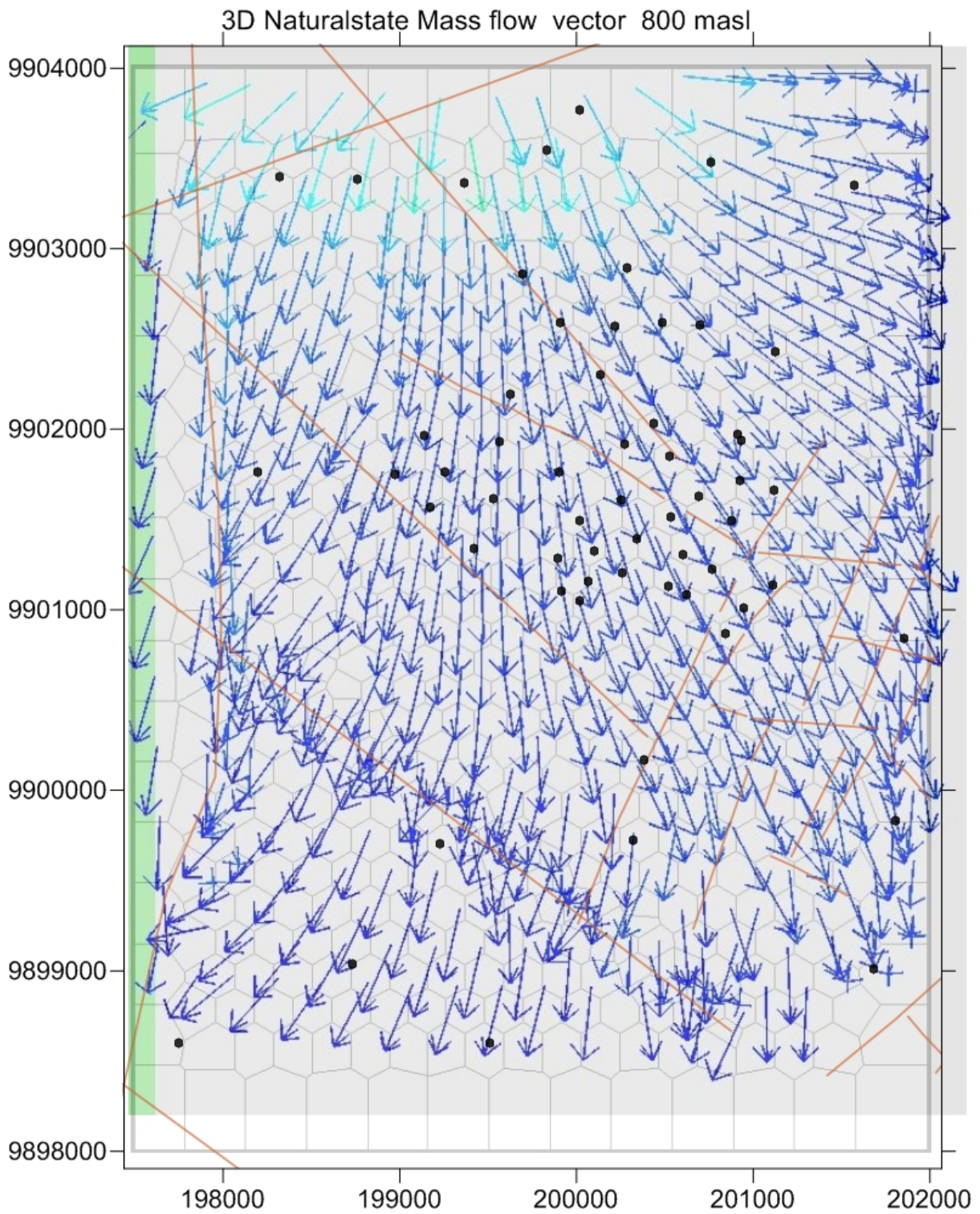
FIGURE E.1: Mass flow vector in the natural state model (arrows) at 800 m a.s.l.,
main fractures and wells
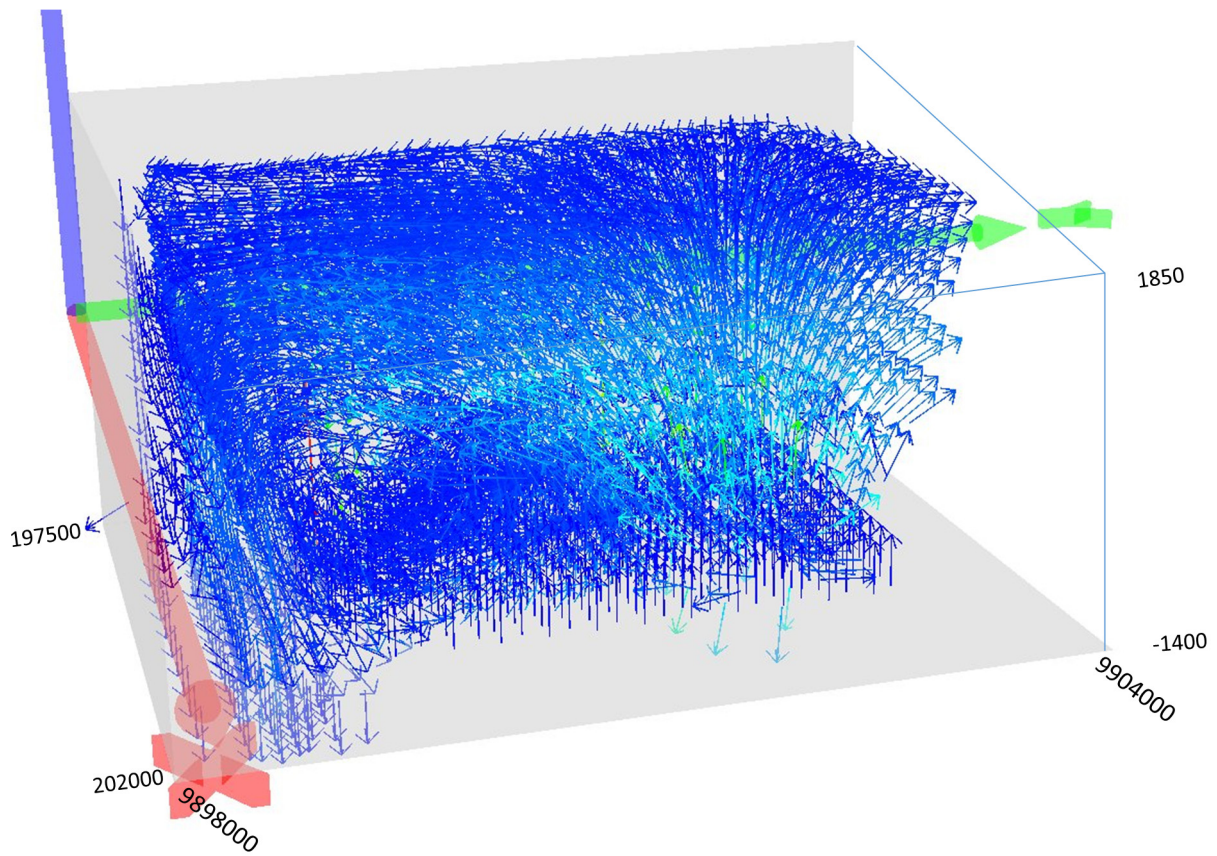
FIGURE E.2: 3D Vector flow field for the total mass flow in the geothermal field as simulated with natural state numerical model
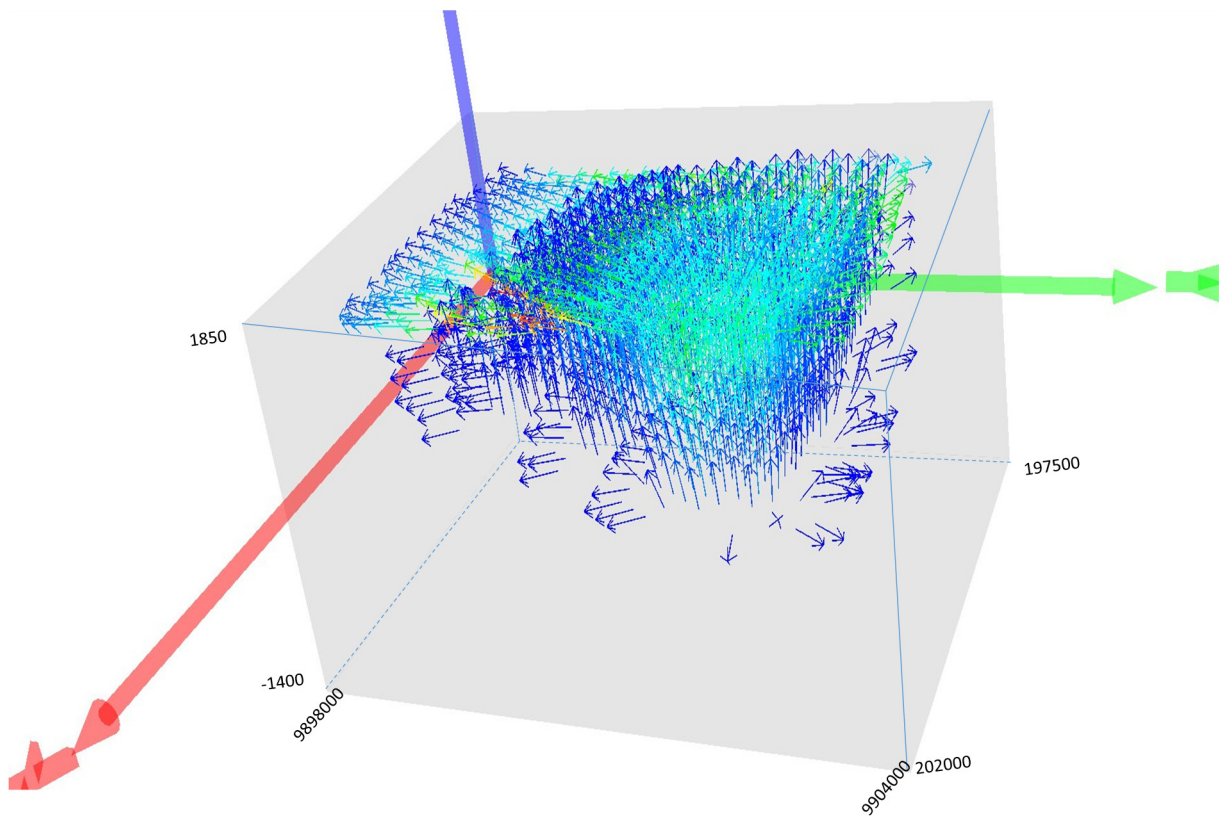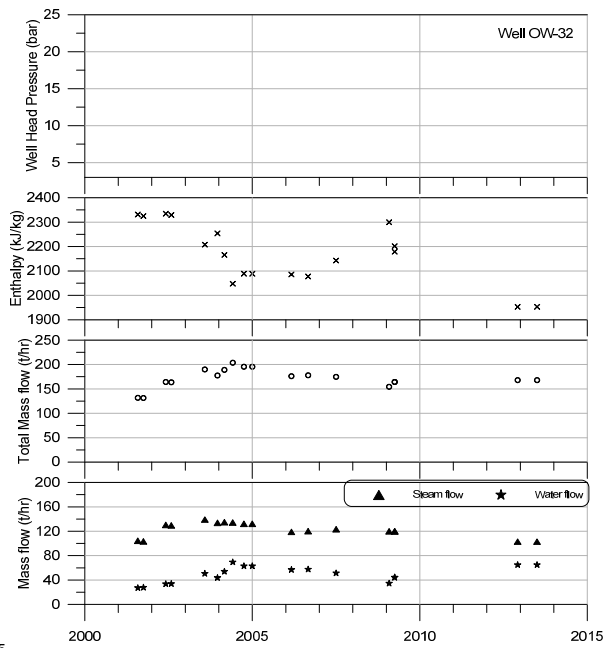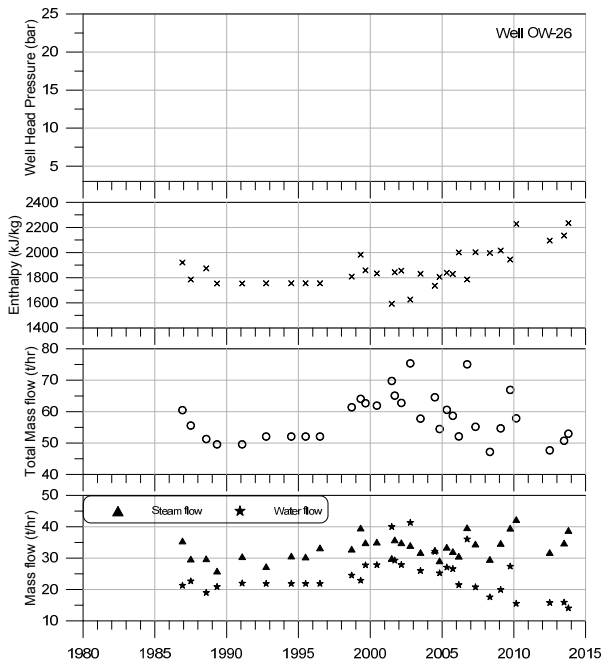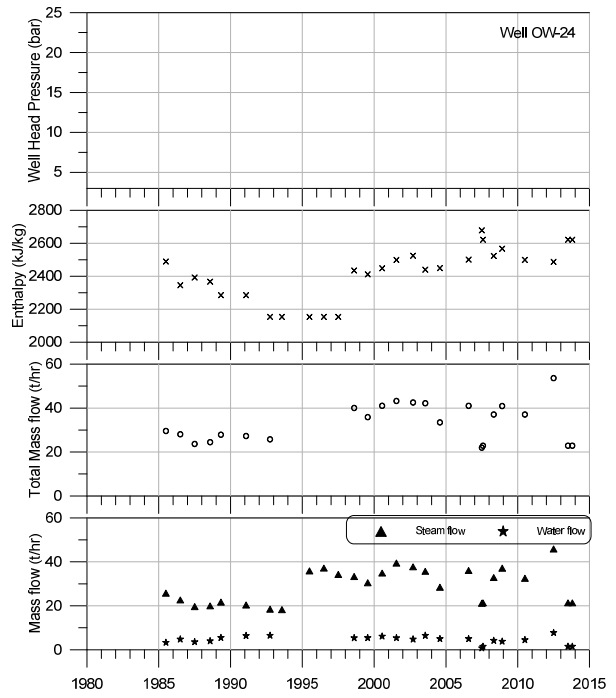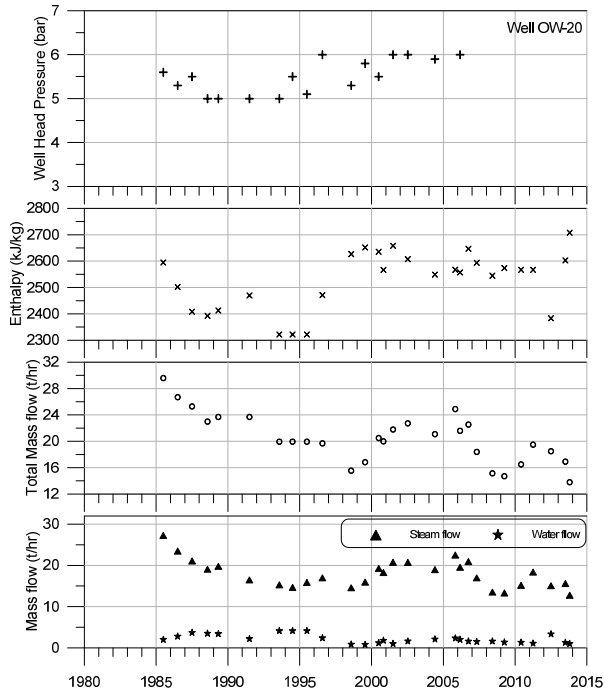

FIGURE E.3: 3D Vector flow field for the steam (vapour phase) flow in the geothermal field
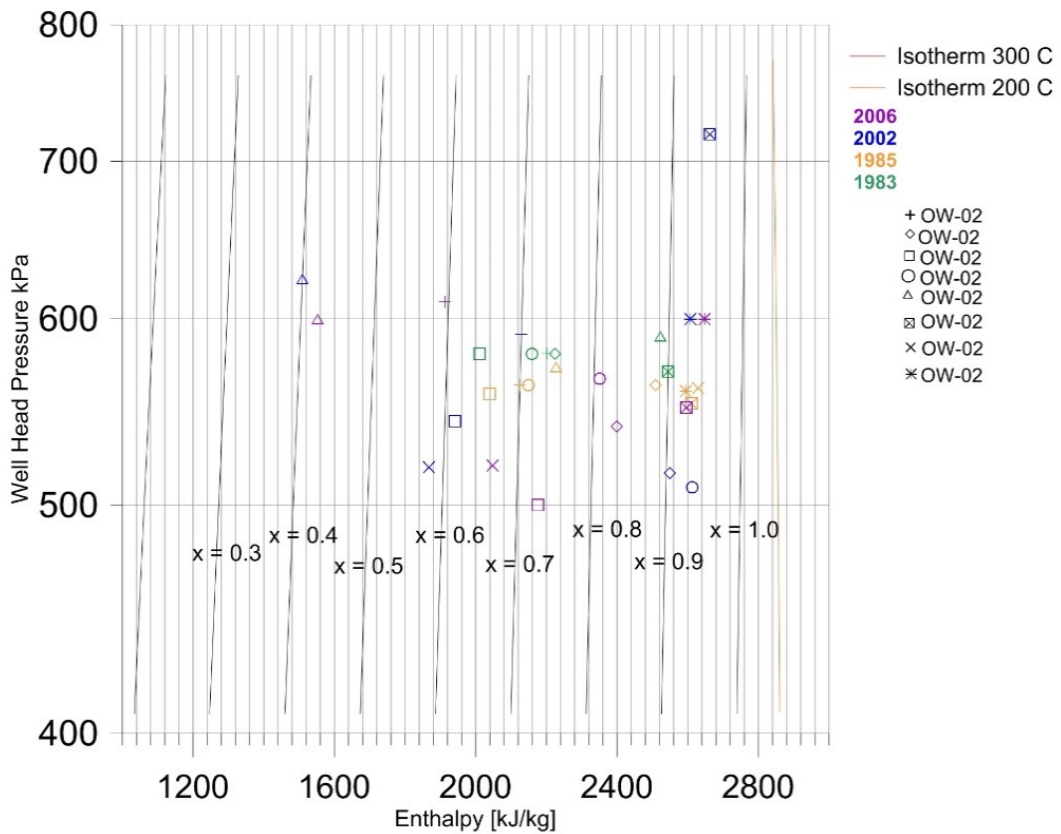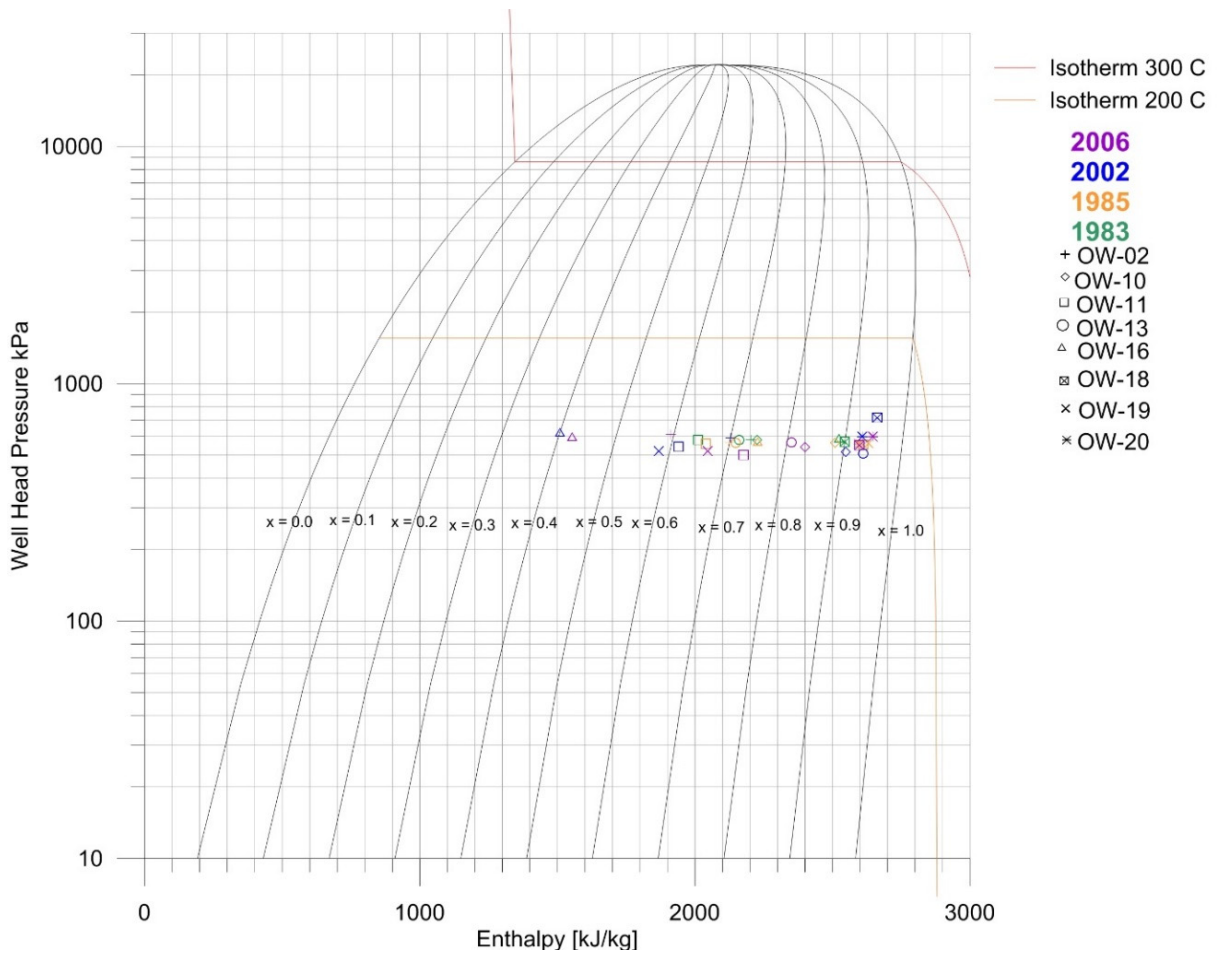
APPENDIX F: Production history plots
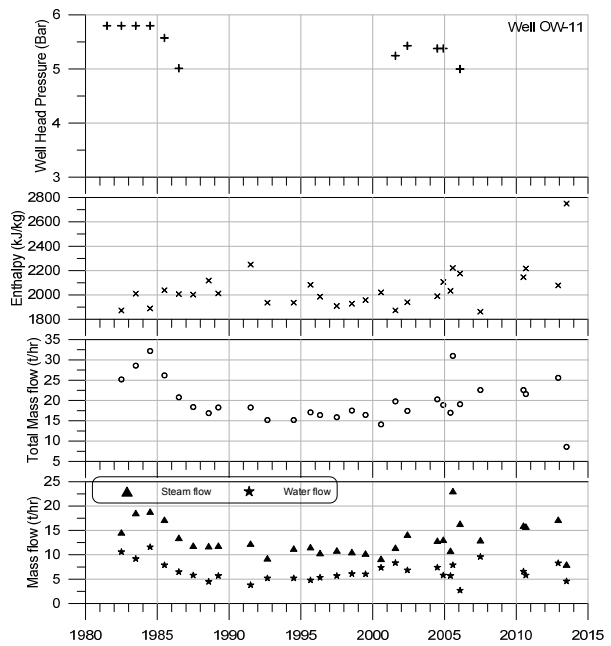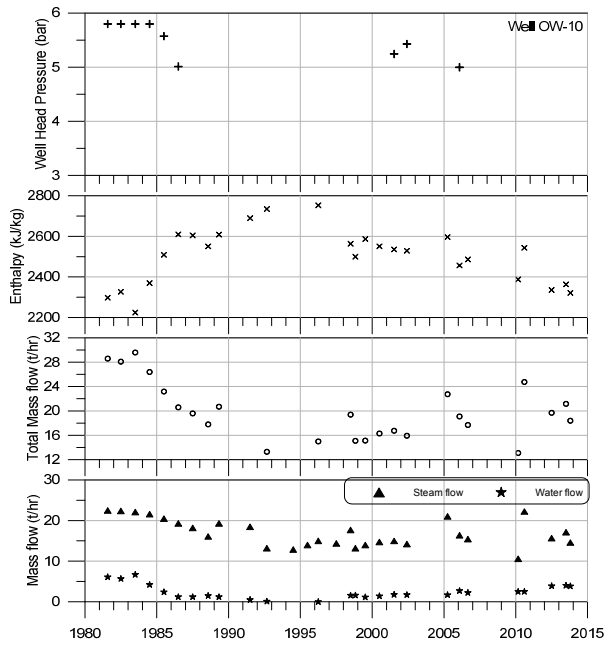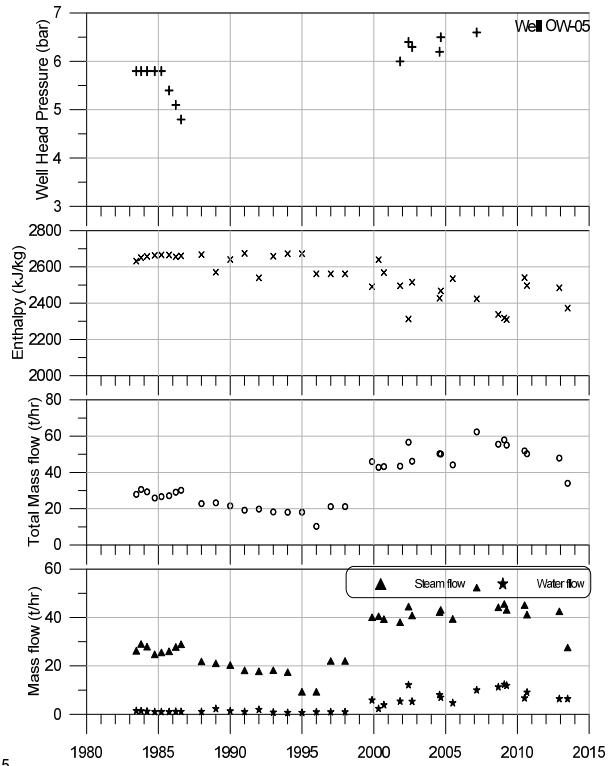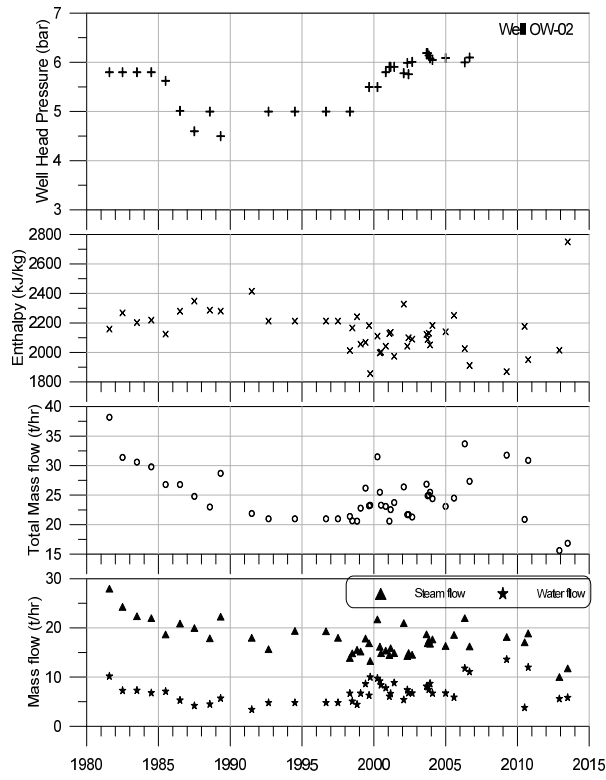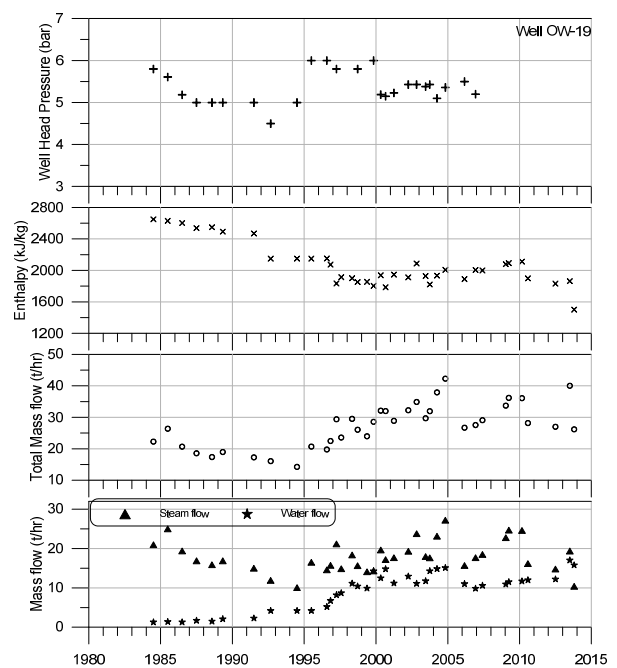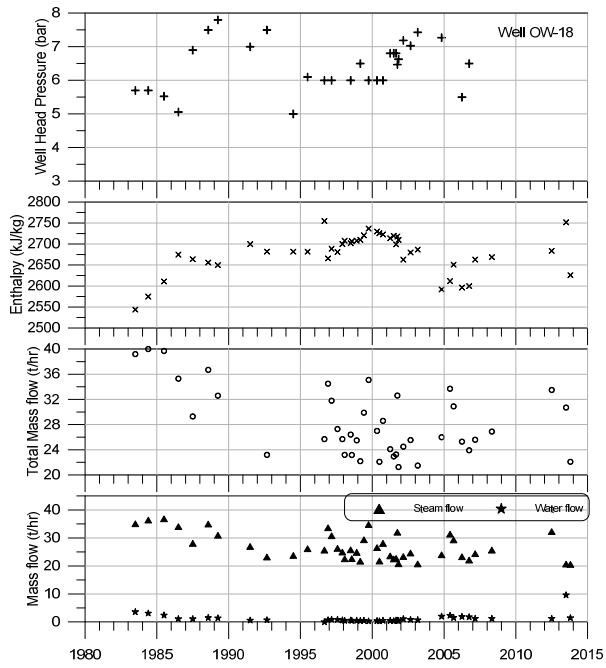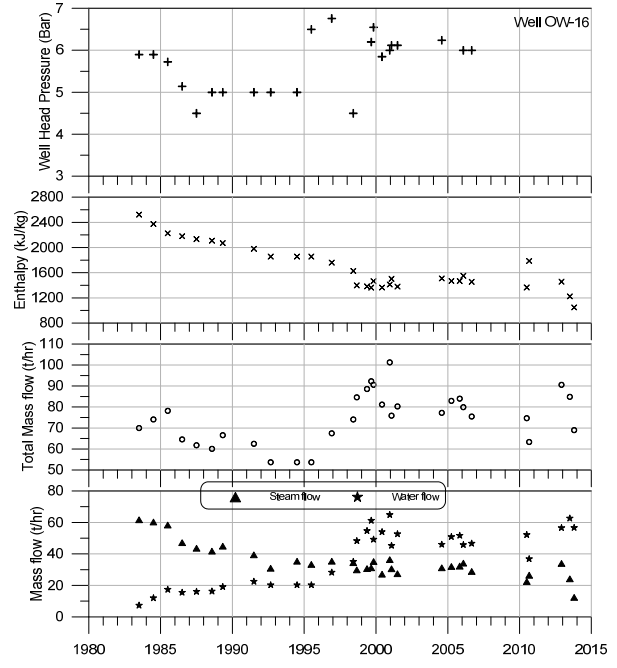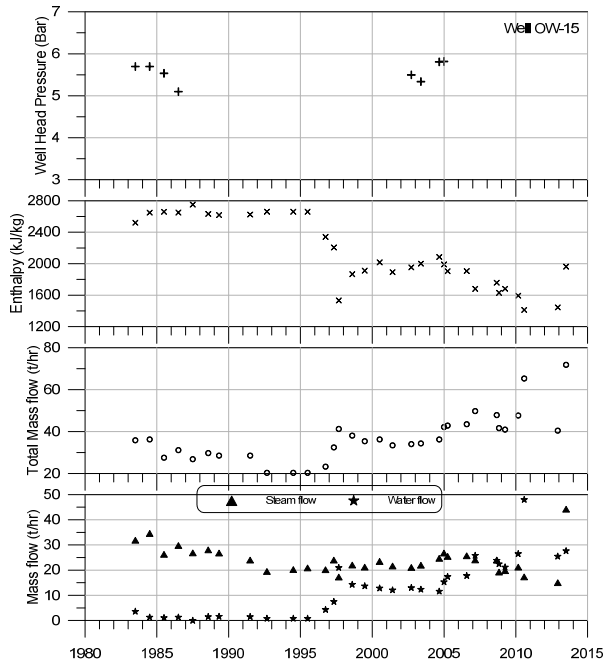
# APPENDIX G: Field production history on a p-h diagram

APPENDIX H: Production wells and feed zone assignment

TABLE H-1: Production model wells - elements assignment

Well No.	Feed zones (m)	Model layer name, elevation and depth										Enth. data	Draw-down data
	L : Liquid dominated S: Steam dominated	D	E	F	G	H	I	J	K	L			~600 masl
	Elevation[m]	1350	1100	900	700	500	200	-200	-600	-900	-1100		
	Depth [m]	550	800	1200	1400	1700	2100	2500	2800	3050	3300		
OW-02	700-750 (S); 900 (L), 1100 (L)											Yes	
OW-03	700-800(S); 900 (L), 1100 (L)												Yes
OW-04	750-850 (S); 1300-1400 (L), 1450- 1600 (L)												
OW-05	700 (S), 800 (L)											Yes	Yes
OW-06	850 (L)											Yes	
OW-07	750-800 (L)												
OW-08	550-700 (S); 900-1080 (L), 1200-1400 (L)											Yes	
OW-09	600 (S), 720 (S); 1060 (L),												
OW-10	650-670 (S); 900 (L), 1100 (L)											Yes	
OW-11	725-750(S); 1150-1200(L)											Yes	
OW-12	575 (S), 750 (S); 850-900 (L)												
OW-13	600-650 (S); 850-900 (L)											Yes	
OW-14	600-700 (S); 900-1000 (L)												
OW-15	700-800 (S); 1100-1175 (L)											Yes	
OW-16	700-750 (S),1125- 1150 (L)											Yes	
OW-17	545-600 (S); 800-900 (L), 1150 (L)												
OW-18	540-600 (S); 800-900 (L), 1150 (L)											Yes	
OW-19	1000-1050 (L), 1550-1600 (L)											Yes	
OW-20	750-850 (L), 1050-1200 (L), 1300 (L)											Yes	
OW-21	700-750 (S); 1000-1125 (L), 1275-1300 (L)											Yes	Yes
OW-22	700-750 (S); 1000 (L)											Yes	
OW-23	530-700 (S); 900-1000 (L), 1250 (L)											Yes	
OW-24	550-700 (S); 1050-1100 (L)												
OW-25	550-650 (S); 1200-1400 (L)											Yes	
OW-26	570-625 (S); 750-800 (L), 1300 (L)											Yes	
OW-26	570-625 (S); 750-800 (L), 1300 (L)											Yes	
OW-27	700-900 (S); 1030-1150 (L), 1300- (L)												
OW-33	700-900 (S); 1030-1150 (L), 1300- (L)												Yes
OW 29	1000-1500												
OW 31	1350 (2phase x= 0.8)												
OW 32	900-2400											Yes	
OW 34	900-2400											Yes	

APPENDIX I: Production model enthalpy calibration plots
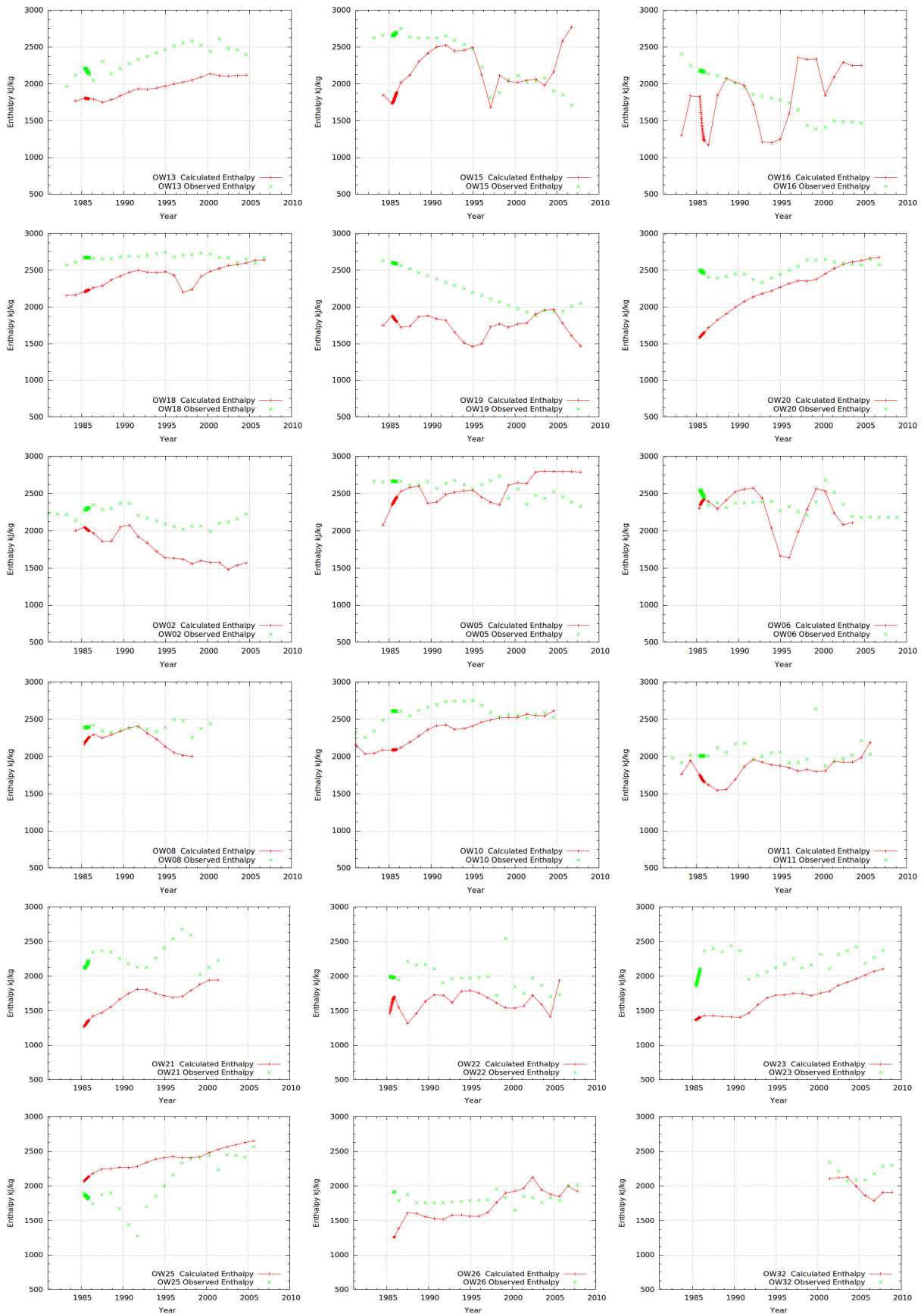
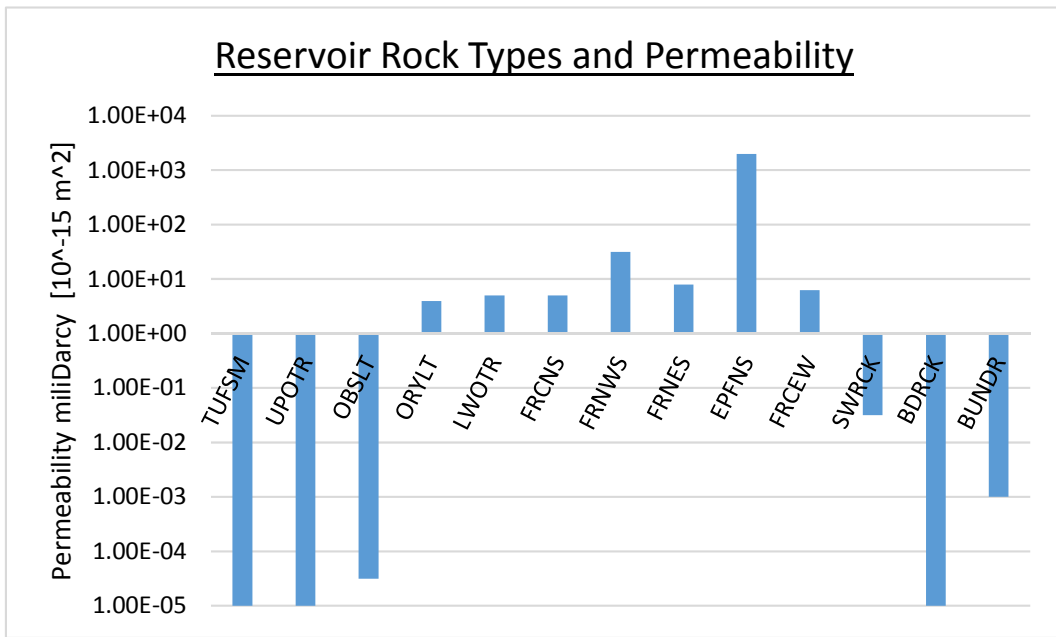**APPENDIX J: Rock types and their permeability**

FIGURE J.1: Permeabilities of the rock types assigned to the reservoir domain